

**QUANTITATIVE ULTRASOUND
CHARACTERIZATION OF RESPONSES TO
RADIOTHERAPY
*IN VITRO AND IN VIVO***

by

Roxana M. Vlad

A thesis submitted in conformity with the requirements for the degree
of Doctor of Philosophy
Graduate Department of Medical Biophysics
University of Toronto

© Copyright by Roxana M. Vlad 2009



Library and Archives
Canada

Published Heritage
Branch

395 Wellington Street
Ottawa ON K1A 0N4
Canada

Bibliothèque et
Archives Canada

Direction du
Patrimoine de l'édition

395, rue Wellington
Ottawa ON K1A 0N4
Canada

Your file Votre référence
ISBN: 978-0-494-60877-7
Our file Notre référence
ISBN: 978-0-494-60877-7

NOTICE:

The author has granted a non-exclusive license allowing Library and Archives Canada to reproduce, publish, archive, preserve, conserve, communicate to the public by telecommunication or on the Internet, loan, distribute and sell theses worldwide, for commercial or non-commercial purposes, in microform, paper, electronic and/or any other formats.

The author retains copyright ownership and moral rights in this thesis. Neither the thesis nor substantial extracts from it may be printed or otherwise reproduced without the author's permission.

AVIS:

L'auteur a accordé une licence non exclusive permettant à la Bibliothèque et Archives Canada de reproduire, publier, archiver, sauvegarder, conserver, transmettre au public par télécommunication ou par l'Internet, prêter, distribuer et vendre des thèses partout dans le monde, à des fins commerciales ou autres, sur support microforme, papier, électronique et/ou autres formats.

L'auteur conserve la propriété du droit d'auteur et des droits moraux qui protègent cette thèse. Ni la thèse ni des extraits substantiels de celle-ci ne doivent être imprimés ou autrement reproduits sans son autorisation.

In compliance with the Canadian Privacy Act some supporting forms may have been removed from this thesis.

While these forms may be included in the document page count, their removal does not represent any loss of content from the thesis.

Conformément à la loi canadienne sur la protection de la vie privée, quelques formulaires secondaires ont été enlevés de cette thèse.

Bien que ces formulaires aient inclus dans la pagination, il n'y aura aucun contenu manquant.


Canada

Abstract

Quantitative ultrasound characterization of responses to radiotherapy *in vitro* and *in vivo*

Roxana M. Vlad

A thesis submitted in conformity with the requirements for the degree of Doctor of
Philosophy
Graduate Department of Medical Biophysics
University of Toronto
Copyright by Roxana M. Vlad 2009

In clinical oncology and experimental therapeutics, changes in tumour growth rate or volume have been traditionally the first indication of treatment response. These changes typically occur late in the course of therapy. Currently, no routinely available imaging modality is capable of assessing tumour response to cancer treatment within hours or days after delivery of radiation treatment. Therefore, the goal of this thesis is to develop the use of ultrasound imaging and ultrasound characterization methods with frequencies of 10 to 30 MHz to assess non-invasively tumour response to radiotherapy, early, within hours to days after delivery of radiotherapy.

Responses to radiotherapy were characterized initially *in vitro* in a well-controlled environment using cell samples. It was demonstrated experimentally that the changes in ultrasound integrated backscatter and spectral slopes were the direct consequences of cell and nuclear morphological changes associated with cell death. The research *in vitro* provided a basis for the *in vivo* research that characterized responses to radiotherapy in cancer mouse

models. The results from mouse tumour models indicated that quantitative ultrasound could detect the regions in a tumour that corresponded in histology to areas of cell death.

In order to understand the cellular morphological changes responsible for ultrasound scattering at these frequencies and assist in the interpretation of experimental data, numerical simulations of ultrasound scattering from four different cell lines exposed to radiotherapy were conducted and compared to experimental results. It was concluded that the increases measured in ultrasound backscatter could in part be explained by the increase in the randomization of cell nuclei resulting from the increase in the variance of cell sizes following cell death.

In this thesis, it is demonstrated that ultrasound imaging and quantitative ultrasound methods were able to detect non-invasively early responses to radiotherapy *in vitro* and *in vivo*. The mechanism behind this detection was linked to changes in the acoustic properties of nuclei and changes in the spatial organization of cells and nuclei following cell death. This provides the groundwork for future investigations regarding the use of ultrasound in cancer patients to individualize treatments non-invasively based on their responses to specific interventions.

Table of Contents

Abstract.....	ii
Table of contents	iv
Abstract.....	ii
Acknowledgements.....	ix
List of Symbols and Abbreviations	x
1 INTRODUCTION	1
1.1 Historical setting, cancer disease	1
1.2 Cancer treatment, radiotherapy	2
1.3 Interaction of radiation with matter.....	3
1.3.1 Responses to ionizing radiation, cell death	3
1.4 Clinical imaging of tumour responses to ionizing radiation	6
1.5 Ultrasound imaging in oncology	8
1.6 Imaging cell death	10
1.7 Role of quantitative ultrasound in cancer management	11
1.8 Rationale, detection and prediction of early tumour responses to radiotherapy	12
1.9 Thesis outline	15
2 ACOUSTIC SCATTERING THEORY APPLIED TO SOFT BIOLOGICAL TISSUES.....	17
2.1 Abstract.....	17
2.2 Ultrasound interaction with tissue	18
2.3 Scattering from single particles	20
2.4 Weak scattering from random distribution of inhomogeneities.....	23
2.4.1 Rationale for quantitative ultrasound	29
2.4.2 Relating power spectra to tissue microstructure	30
2.4.3 General principles of spectrum analysis	33
2.5 Scattering by populations with non-random distribution of scatterers	37

2.5.1 Background.....	37
2.5.2 Scattering by regular and more random distributions of point-like scatterers.....	40
2.6 Structures potentially responsible for ultrasound scattering in tissue	43
3 QUANTITATIVE ULTRASOUND CHARACTERIZATION OF CANCER RADIOTHERAPY EFFECTS IN VITRO	45
3.1 Abstract.....	45
3.2 Introduction	47
3.3 Methods	49
3.3.1 Cell preparation	49
3.3.2 Ultrasound data acquisition and analysis	50
3.3.3 Statistics.	51
3.3.4 Cytological analysis, cell size and morphology measurements	52
3.4 Results	52
3.5 Discussion.....	59
3.6 APPENDIX - Assessment of cell morphological changes indicative of responses to ionizing radiation	63
4 QUANTITATIVE ULTRASOUND CHARACTERIZATION OF RESPONSES TO RADIOTHERAPY IN CANCER MOUSE MODELS	66
4.1 Abstract.....	66
4.2 Introduction	68
4.3 Methods	70
4.3.1 Animal use	70
4.3.2 Mouse Tumours.....	70
4.3.3 Ultrasound data acquisition and analysis	72
4.3.4 Histology.....	74
4.4 Results	75
4.5 Discussion.....	81

5 AN INCREASE IN CELL SIZE VARIANCE APPEARS TO EXPLAIN PART OF THE ULTRASOUND BACKSCATTER INCREASE MEASURED DURING CELL DEATH	85
5.1 Abstract.....	85
5.2 Introduction	87
5.3 Background.....	89
5.4 Methods	92
5.4.1 Cell preparation	92
5.4.2 Ultrasound data acquisition and analysis	94
5.4.3 Cytology analysis, measurements of cellular and nuclear size.....	96
5.4.4 Simulation.....	98
5.5 Results.....	101
5.6 Discussion.....	110
5.7 Conclusion	114
6 CONCLUSION AND FUTURE WORK	116
6.1 Conclusion	116
6.2 Implications	120
6.3 Future work	122
6.3.1 Future work, registration of whole mount tumour histology with 3D ultrasound and parametric images.....	123
6.3.2 Future work, predicting the contribution of nuclear acoustic properties and nuclei spatial organization to ultrasound backscatter	124
6.3.3 Future directions in characterization of cell death using QUS methods.....	125
7 REFERENCES	128

Figure 1.1. Hematoxylin & eosin staining of hep-2 cell samples.....	6
Figure 2.1. Ultrasound interactions with boundaries and particles.	19
Figure 2.2. Backscattering cross-section for a compressible sphere.....	22
Figure 2.3. The scattering geometry for an inhomogeneity	24
Figure 2.4. Relationship between the effective scatterer diameter and spectral slope.	33
Figure 2.5. Spectrum analysis	36
Figure 2.6. Hematoxylin and eosin staining	38
Figure 2.7. System block diagram of the transmit/receive response for a scattering volume.....	41
Figure 3.1. Representative ultrasound images of Hep-2 cell samples.....	54
Figure 3.2. Normalized power spectra and microscopy images	55
Figure 3.3. Flow-cytometric measurement of cellular DNA content.	57
Figure 3.4. Histograms of cell size distributions	58
Figure 3.5. Linear correlation between the UIB and the variance of cell sizes.....	59
Figure 4.1. The experimental setup for ultrasound data collection	72
Figure 4.2. Representative ultrasound images of the XRT(-) and XRT(+) tumours	76
Figure 4.3. Ultrasound spectral parameter characterization of tumour responses to radiotherapy.	77
Figure 4.4. Representative ultrasound images and corresponding tunel staining of FaDu tumours.....	78
Figure 4.5. Ultrasound image with corresponding histology and parametric images.	79
Figure 4.6. Hematoxylin and eosin images of the XRT(+) tumour	80
Figure 5.1. The schematic illustrating the possible position of scattering structures.....	92
Figure 5.2. Images of the sample holder and a cell sample.	94
Figure 5.3. The simulation model.....	100
Figure 5.4. UIB, representative H&E staining and the corresponding measurement of DNA content	103
Figure 5.5. Representative H&E staining and corresponding measurement of DNA content ..	105
Figure 5.6. Representative staining of FaDu cell samples	107
Figure 5.7. Histograms of cell size distributions.	108
Figure 5.8. Increase in integrated backscatter versus randomization:.....	109
Figure 6.1. Histograms of cell size distribution and corresponding H&E staining	120

Table 3-1. Ultrasound parameters measured from cell samples	53
Table 5-1. Attenuation coefficients.....	96
Table 5-2. The UIB, cellular and nuclear diameter and relevant DNA fractions.....	102
Table 6-1. The effective scatterer size and average nuclear size measured from cell samples and tumour xenografts.....	118

Acknowledgements

This time, working on my PhD has been a period of valuable transformations that would have not been possible without the encouragement, support and guidance of people around me.

I feel fortunate to have Drs. Michael Kolios and Gregory Czarnota as mentors. Michael Kolios is the rare kind of teacher who does not open the book to point you to the right answer; instead, he opens your mind by asking the right question, letting you the joy of discovering the answer. I have been learning enormously from our endless discussions and from his personal example. Gregory Czarnota is the best example I ever had that “the brick walls are there just for those who do not want badly enough to go beyond”. He has the most interesting approaches to different situations and ability to foresee “the tiny light at the end of the tunnel”. These and the time spent in his laboratory have determined my development as an independent thinker. I would like to thank to my advisory committee, Drs. Fei-Fei Liu and Peter Burns who provided direction, critical comments and support. I have learned so much from their commitment to research and knowledge.

I would also like to thank to Anoja Giles who taught me much more than laboratory biology. Her kindnesses, patience, commitment, organization in all little details and willingness to listen to everyone have been a continuous inspiration to me.

Mircea, I am grateful for your place in my life, thank you for all the encouragement and for believing so much in me. If it were not for your strong belief in what “makes me happy”, this PhD would not have begun. My little Stefan, you are now the age of my PhD, both of us have learned so much during these four years. My dear mother and father, the good example I took from home helped me in all my decisions. My dear father, this thesis is dedicated to you. Your example, the strength to follow your beliefs without compromise, the deep conviction that the spirit empowers the human being, above wealth and social position have been always helping me to find the right path. I want to ensure you once more time that, *iarba verde de acasa sa ma ratacesc prin lume nu ma lasa* (the green grass from home doesn't let me get lost into the world).

List of Symbols and Abbreviations

a	scatterer radius
a_{eff}	effective scatterer radius
ATS	attenuation coefficient slope
α	attenuation coefficient in the sample
b_{γ}	correlation coefficient,
CT	computed tomography
D	correlation distance
Day ₀	time of first ultrasound data collection;
Day ₁	time of second ultrasound data collection at 24 hours after Day ₀
ρ_0	density of the surrounding medium
ρ	density of the scatterer
DCE-DUS	dynamic contrast-enhanced Doppler ultrasound
DCE-MRI	dynamic contrast-enhanced magnetic resonance imaging
f	frequency
FDG	fluoro-2-deoxy-d-glucose
λ	wavelength
Gy	Gray
H	hour
H&E	hematoxylin and eosin
k	the wave number
κ_0	compressibility of the surrounding medium
κ_1	compressibility of the scatterer
L	length of the Hamming window
MBF	mid-band fit
MRI	magnetic resonance imaging

n	the average concentration of scatterers
NPS	normalized power spectra
PET	positron emission tomography
P_0	amplitude of pressure in the incident wave
p_i	incident pressure wave
p_s	scattered pressure wave
QUS	quantitative ultrasound;
r	radius
RECIST	response evaluation criteria in solid tumours
RF	radio-frequency
ROI	region of interest
c	speed of sound
SI	spectral intercept
SOS	speed of sound
SS	spectral slope
θ	the angle between the incident wave and scattered wave
θ_i	incident angle
θ_t	reflection angle
TUNEL	terminal uridine deoxynucleotidyl transferase 2'-Deoxyuridine 5'-Triphosphate nick end labeling;
UIB	ultrasound integrated backscatter
V	volume
XRT(-)	tumours prior exposure to radiotherapy;
XRT(+)	tumours exposed to radiotherapy.
Z	acoustic impedance

1 INTRODUCTION

1.1 Historical setting, cancer disease

Cancer is not a modern disease. Human malignant tumours have been described in pictures and in writing dating back to ancient civilizations, for example, bone cancers (osteosarcomas) have been identified in Egyptian mummies (1). Early cultures attributed the cause of cancer to various Gods, and this belief was held until the Middle Ages. Hippocrates however, described cancer as an imbalance between the black fluid (from the spleen) and the three bodily fluids: blood, phlegm and bile. Although incorrect, this theory was the first (~ 400 B.C.) to attribute the origin of cancer to natural causes. The suggestion that cancer might be an inherited or environmental disease appeared later, writings from the Middle Ages referring to “cancer houses”, “cancer families” and “cancer villages”(1).

Epidemiological studies later identified major environmental causes of cancer, such as tobacco smoke and various occupational exposures. Such studies raise the possibility of prevention through changes in life-style and diet, as has already been demonstrated through smoking cessation programs in many Western countries. Recently, molecular genetics has increased our knowledge about cancer biology. The rapid evolution of molecular biology techniques has led to the characterization, cloning and sequencing of a variety of genes where mutations or changes in their expression can lead to malignant transformation. The current model for cancer development envisions cells undergoing a series of genetic alterations which result in their inability to respond normally to intracellular or extracellular signals that control proliferation, differentiation and ultimately cell death (1). Increased numbers and types of genetic abnormalities, often specific for the tumour type,

accompany tumour progression. The development of cancer is a multistep process that progresses from benign to premalignant before manifesting as malignancy.

1.2 Cancer treatment, radiotherapy

Cancer treatment is based on two major approaches: therapy localized to the tumour mass (surgery, radiotherapy), the use of drugs (chemotherapy) or the use of a combination of these two approaches to increase therapeutic efficacy. The genetic instability of cancer cells and the resulting heterogeneity of the cellular phenotype within an individual tumour pose a major challenge to the development of more effective treatments that take advantage of the new knowledge of molecular properties of cancer. In this context, radiotherapy remains the most commonly used and effective cancer treatment modality since high doses of ionizing radiation target the entire tumour mass to ensure cancer cell killing. Radiotherapy for cancer typically involves delivering 25-40 individual dose fractions of about 2 Gy daily, over a period of 5 to 8 weeks (1). Such treatment schedules have been developed empirically and demonstrate a better therapeutic ratio than single doses, because they provide tumour control at tolerable levels of normal tissue toxicity. New developments in the delivery of radiation therapy should allow conformal treatments that limit the volume of normal tissues irradiated to high doses while allowing escalation of doses delivered to the tumour. In this context, in stereotactic radiosurgery high doses of up to 25 Gy in one fraction can be delivered to a tumour (2-4).

1.3 Interaction of radiation with matter

Since their discovery by Roentgen more than a century ago, X-rays have played a major role in modern medicine. The first recorded use of X-rays for the treatment of cancer occurred within about one year of their discovery (1). X- and γ -rays constitute part of the continuous spectrum of electromagnetic radiation that includes radio waves, heat, visible and ultraviolet light. All types of electromagnetic radiation can be considered as moving packets of energy, called photons. Individual photons of X- and γ -rays are sufficiently energetic that their interaction with matter can result in the complete displacement of an electron from its orbit around the nucleus of an atom. Typical binding energies for electrons in biological material are approximately 10 eV (electron volt), thus photons with energies greater than 10 eV are considered to be ionizing radiation (1). Radiation can cause damage to any molecule in a cell, but damage to DNA is the most crucial, causing cell lethality expressed by loss of proliferative potential (1). The damage to DNA can result from a direct interaction by direct energy absorption, or by indirect effects resulting from interaction with chemically reactive free-electrons or free-radicals (molecules with unpaired electrons). The [OH \cdot] radicals resulting from the interaction of radiation with water are probably the most damaging. DNA is the major target of ionizing radiation because of its biological importance to the cell. Even relatively small amounts of DNA damage can lead to cell lethality.

1.3.1 Responses to ionizing radiation, cell death

Inhibition of the reproductive ability of the cell is an important consequence of the molecular and cellular responses to radiation. It occurs at relatively low doses (a few Gray) and it is a major objective in clinical radiotherapy. Cancer radiotherapy aims to kill the

tumour by inducing cell death including apoptosis, mitotic arrest/catastrophe (cells that undergo up to four abortive mitotic cycles) or terminal growth arrest (cells that lose the ability to divide) (1). The extent to which one mode of cell death is dominant over another is dependent on cell type, radiation dose and the cell's microenvironment (relative oxygenation and availability of growth factors).

Apoptosis, frequently referred to as 'programmed cell death' is an active mode of cell death in which the cell itself executes a genetic program leading to its own death and subsequent cell body disposal (5). One of the early events is cell dehydration. Loss of intracellular water leads to the condensation of the cytoplasm followed by a change in cell shape and size, the originally round cell becomes elongated and smaller (5). The most characteristic feature of apoptosis is the condensation of nuclear chromatin. Condensed chromatin has a uniform, smooth appearance with no evidence of any texture typically observed in a phenotypically normal nucleus. DNA in condensed chromatin stains strongly with fluorescent and light absorbing dyes (Figure 1.1).

Mitosis is the nuclear division that produces two daughter nuclei, each with the same number of chromosomes as the parental nucleus. This process is complex and highly regulated. The sequence of events is divided into phases, corresponding to the completion of one set of activities before the start of the next.

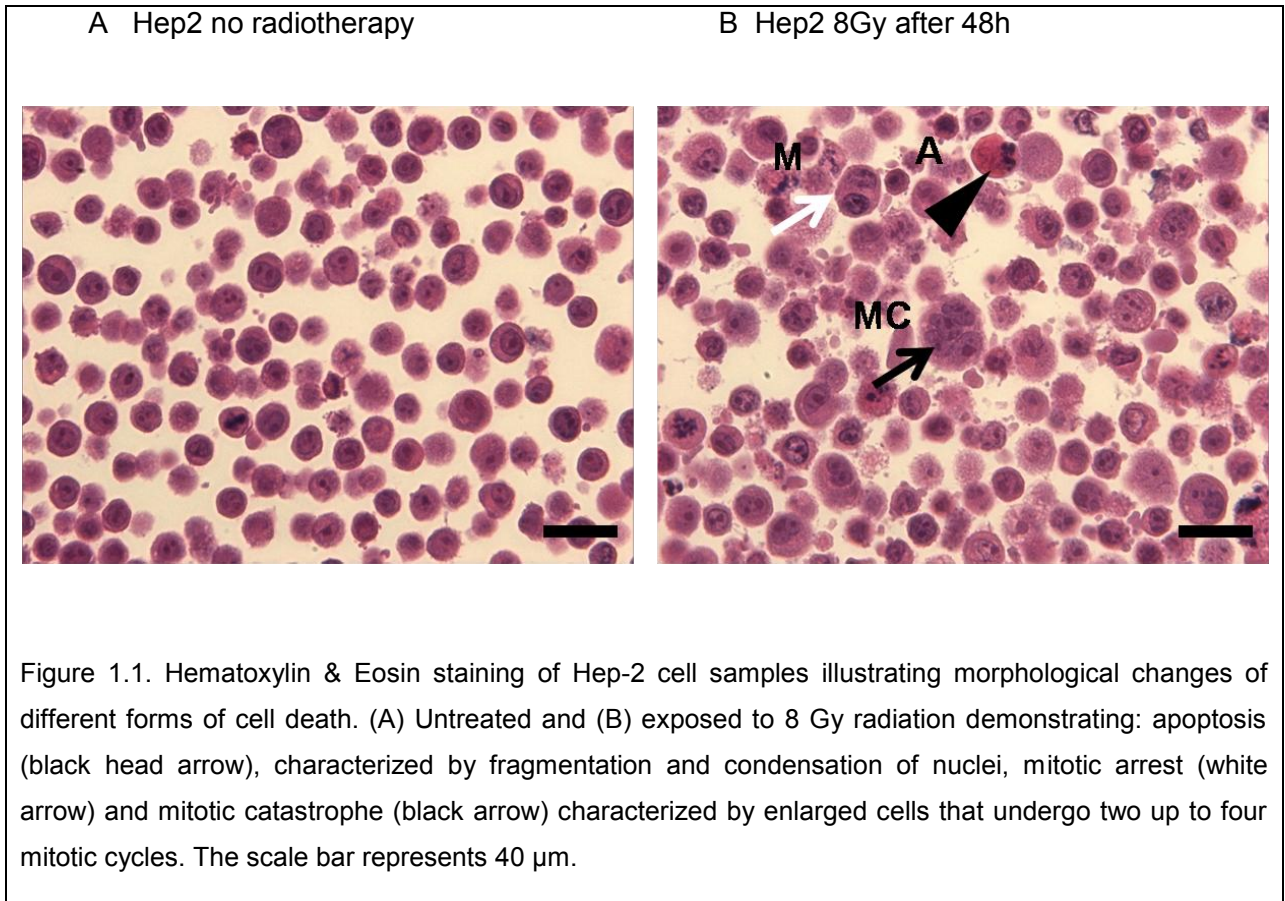
Mitotic cell death or mitotic arrest/catastrophe describes cell death occurring in the cell cycle following exposure to injury (5). For example, following radiotherapy cells can undergo mitotic arrest/catastrophe in cell cycles subsequent to the one in which the radiation exposure occurred. The cell, transiently arrested in the cell cycle as a result of the damage, is able to divide later. Its progeny cells, however, die when progressing through the subsequent cell cycle(s). The cause of their death may be damage to genes which are

essential for cell survival (5), or inability to complete the phases of cell division. For instance, cells will not progress through mitosis if the chromosomes of the two resulting daughter cells are not properly aligned during cell division. These cells are not able to complete their division resulting in cells containing two times or four times more nuclear material than their parental cells. Therefore, enlarged cells and nuclei are some of the features of cell undergoing mitotic arrest/catastrophe (Figure 1.1).

Senescent or terminally arrested cells are metabolically active but do not proliferate and do not form colonies following irradiation. They eventually die, days to weeks following irradiation, by necrosis (1). The cellular and/or nuclear size during the initial phases of cell arrest do not appear to change significantly.

Oncosis describes cell damage in which cell swelling is the predominant early response. It follows a variety of injuries (i.e., toxins and ischemia) applied *in vivo* or *in vitro* (6).

Necrosis refers to changes that occur following cell death, i.e., attributed to post-mortem changes (5, 6). Thus, necrosis is not a form of cell death but the end stage of any cell death process (e.g., equivalent to the post-mortal decay after clinical death) (7). In this phase following cell death, the morphological changes of the cell involve degradative processes that result in decomposition of organelles and other macromolecular systems (6).



1.4 Clinical imaging of tumour responses to ionizing radiation

Tumour responses to treatment have been clinically assessed by measurements of tumour size, using anatomical imaging techniques such as X-ray computed tomography (CT) and magnetic resonance imaging (MRI). CT imaging is based on the measurement of the amount of X-ray attenuation as X-rays pass through different tissues within the body (e.g., bone and soft tissues have different attenuation coefficients). MRI involves the detection of nuclear spin reorientation of water protons in an applied magnetic field. MRI of tissue water protons is used similarly to CT to provide images of anatomy but with better soft tissue contrast. These imaging modalities have been used clinically to assess tumour response to

therapies based on a reduction of the tumour size although tumour shrinkage can take weeks or even months to become apparent (8).

In recent years, these measurements have been supplemented by imaging of tissue function, often termed molecular imaging, that aims to characterize biological processes at the cellular and molecular level *in vivo*. From this category, positron emission tomography (PET) imaging using a glucose analogue, the radionuclide 2-[¹⁸F] fluoro-2-deoxy-d-glucose (FDG) is an established modality in the diagnosis and management of various malignancies (8). Since tumours typically have high rates of aerobic glycolysis, they take up relatively large amounts of glucose. FDG is taken up by glucose transporters and phosphorylated by hexokinases, the first enzymes in the glycolytic pathway, but the resulting FDG-6-phosphate is not metabolized further and is trapped within the cell. The uptake and retention of FDG is greater in many tumours than in normal tissues, so that FDG PET scanning is sensitive for localizing tumours and monitoring the response to treatment (1, 18). Since PET images have relatively poor resolution, PET is often used in conjunction with CT that provides high-resolution images of tissue anatomy. The combination of PET/CT provides the opportunity to integrate the morphological information (tumour size) with functional information (tumour metabolic rate) leading to improvements in tumour detection and response monitoring (9, 10). Studies of lung cancer (11), oesophageal cancer (12) and lymphoma (13) have demonstrated that reduced FDG uptake can identify early tumour response to treatment. Persistently increased FDG uptake after treatment is associated with a high risk for early disease recurrence and poor prognosis (8). However, FDG PET has some limitations including lower sensitivity for slowly growing, metabolically less-active tumours and has high levels of uptake in some normal tissues and accumulation in inflammatory cells (8). Most of the clinical studies regarding the benefit of FDG PET in assessing responses to cancer therapy were performed on tumours treated with chemotherapy or with new experimental

therapies. Since early radiotherapy effects include inflammatory reactions that can result in FDG uptakes comparable to tumour uptakes, it has been frequently recommended that FDG-PET to be performed several months after completion of radiotherapy (14). This might explain why less FDG-PET data are available in terms of specifically assessing tumour responses to radiotherapy.

1.5 Ultrasound imaging in oncology

Ultrasound plays an important role in oncology because of its portability, relative low cost, sensitivity, speed of imaging and sub-millimeter spatial resolution. It is often used in the first stages of patient management to visualize tumours, particularly in the soft tissues of the abdomen where both the ultrasound transmission and soft-tissue interfaces are optimal.

In standard B-mode ultrasound imaging, ultrasound probes (transducers) convert electric pulses into acoustic waves and then sense returning echoes (scattering) from biological structures to form an image. The contrast arises from the variation of acoustical properties of various tissues (density, compressibility). Due to various tissue morphological transformations during disease development, the scattering of ultrasound by a tumour and normal tissue is often different. This results in different tumour and normal tissue contrast in an ultrasound image, and therefore ultrasound imaging is capable to differentiate a tumour from apparently healthy tissue based on differences in tissue acoustic properties. Diagnostic imaging is commonly performed in the range of 1 to 10 MHz, because these frequencies ensure the visualization of body structures of interest with a reasonable resolution and penetration depth. Transducer geometry, frequency and the related bandwidth of the pulses determine the axial and lateral resolution of the ultrasound imaging system and the

penetration depth. These parameters and the general physics of ultrasound imaging have been extensively discussed in the literature (15, 16).

An important application in cancer diagnosis is Doppler ultrasound, which measures the Doppler shift in frequency when ultrasound scatters from moving objects, such as red blood cells in the vasculature. The ultrasound frequency employed in standard high-resolution scanners is in the range of 5 to 20 MHz, leading to Doppler shifts due to blood flow in the 1 kHz range. This technique can be used to measure blood flow and blood perfusion in large vessels and has been used to visualize the vasculature of tumours and normal tissue (15, 17, 18).

Frequencies higher than 20 MHz have been used to improve the resolution of images in intravascular, skin, ocular and small animal imaging (19). An important application for this range of frequencies is high resolution imaging of mouse models of disease and anatomy (pre-clinical imaging). Ultrasound preclinical imaging uses frequencies of 10 to 60 MHz and offers spatial resolution as fine as 30 μm . This method allows longitudinal studies with applications in developmental biology and cardiovascular diseases (19-21), tumour growth (22, 23), assessing angiogenesis and drug effects (24), and can be used for identifying novel tumour markers in preclinical cancer mouse models (25). Within the frequency range of 10 to 60 MHz, ultrasound imaging and tissue characterization techniques have been used to detect cell death *in vitro* on cell samples exposed to a chemotherapeutic drug (26, 27), *in vivo* on rat livers exposed to ischemic injury (28) and in cancer mouse models exposed to anti-cancer therapies (26, 29). Imaging and characterizing cell death non-invasively opens a full range of applications in preclinical and clinical settings where cell death is a desired outcome. Some of these applications include assisting in preclinical drug development, assessing tumour responses to cancer treatment and guiding biopsies.

1.6 Imaging cell death

Detecting early tumour response to therapy, and thus predicting the likely outcome of a treatment, requires suitable means to identify markers of the response. Markers of response may include: cell death, changes in metabolism or receptor expression associated with tumour cell death or inhibition of proliferation (8). Increased tumour cell death, early during a course of treatment is a good prognostic indicator of outcome (30-33). Currently, standard methods for detecting cell death are invasive and involve special histological staining. Experimental studies for non-invasive imaging of cell death include diffusion-weighted MRI techniques based on the increase in the apparent diffusion coefficient of water that is thought to increase in tumours responding to applied therapies. This method has been found to predict tumour response in brain cancer patients three weeks after the start of treatment (34). Other imaging methods rely on the fact that apoptotic cells express the negatively charged phospholipid phosphatidylserine on the outer cell membrane with a high affinity for the human protein annexin V. However, early-stage clinical trials using radiolabelled annexin V (^{99m}Tc -6-hydrazinonicotinic Annexin V) had limited success mainly due to the poor clearance and biodistribution of the labeled probe (35).

Experimentally, ultrasound imaging and spectrum analysis techniques were applied for the first time by Czarnota and Kolios (26, 27, 36) to detect cell death in cell samples and tissues exposed to cancer therapies (e.g., chemotherapy and photodynamic therapy). Apoptotic cells exhibited up to a sixteen fold increase in ultrasound backscatter intensity in comparison with viable cells, as well as other measurable changes in ultrasonic parameters (27, 37, 38). The same technique can be used to detect oncotic cell death, following ischemic injury when cells and tissues are deprived of essential nutrients. Ultrasound

backscatter intensity increased up to a eight fold in rat livers exposed to ischemic injury (28) and up to four-fold in cell samples left to die at room temperature (37). Cells can die by apoptosis and mitotic arrest/catastrophe following radiotherapy treatment. Each of these modalities of cell death presents complex and diverse cell structural changes that result in changes of the scattering properties of the cell samples and tissues treated with radiotherapy (39). The etiology behind these changes is not well known but seems to be linked to complex changes in the properties of cell nucleus (e.g. size, density and compressibility) (39-42). The influence of these properties on ultrasound scattering is addressed in this study.

1.7 Role of quantitative ultrasound in cancer management

Tissue characterization methods using ultrasound have been around for more than 20 years (43-50). These methods are based on processing radio-frequency data (before applying envelope detection used to construct conventional ultrasound images) and can improve the diagnostic capabilities of the conventional ultrasonic images by providing quantitative measurements of tissue properties. Much of the early framework for tissue characterization using ultrasound backscatter and spectral techniques was developed by Lizzi et al (49). They demonstrated theoretically and experimentally the ability to ultrasonically quantify ocular, liver and prostate tissue (44, 51-56). Since that time, tissue characterization has been utilized in a variety of applications to differentiate diseased from healthy tissue (52, 57-62). Ultrasonic tissue characterization based on spectrum analysis has proven useful for clinical applications in ophthalmology to distinguish benign from malignant tumours and differentiate among ocular malignancies that were previously indistinguishable (45, 50, 56, 63-65). These methods are currently applied to aid in the

diagnosis of intraocular neoplasms and treatment selection (16). Spectral parameters have also been used to diagnose prostate cancer (52, 57), liver abnormalities (44) and identify benign breast lesions, thus potentially sparing patients from unnecessary biopsies (55). Spectrum analysis significantly improves the detection and evaluation of prostate cancer and real-time applications of spectrum analysis have been proven to significantly decrease the number of false-negative biopsies (57). Other investigators use ultrasonic estimates to construct parametric images, thus providing imaging contrast where grey-scale B mode images did not present any distinguishable differences between healthy and diseased tissues. These parametric images were able to differentiate benign fibroadenomas from mammary carcinomas and sarcomas in mice (66, 67), detect changes in renal and liver microanatomy (47, 68) and differentiate cancerous from noncancerous prostate tissue (52). At higher frequencies of 10 to 60 MHz, spectrum analysis methods have been used to detect various forms of cell (26-28, 39, 69, 70). This capability of ultrasound spectrum analysis to identify various forms of cell death forms the basis of this thesis that aims to characterize the responses to radiotherapy *in vitro* and *in vivo*.

1.8 Rationale, detection and prediction of early tumour responses to radiotherapy

Response evaluation criteria in solid tumours (RECIST) guidelines are traditionally applied to evaluate tumour responses. These guidelines are based on the measurement of the longest diameter of the assessed tumour (71). The following criteria are used to evaluate tumour response:

1. complete response: the disappearance of all target lesions;

2. partial response: at least 30% decrease in the longest diameter of the target lesion;
3. progressive disease: at least 20% increase in the longest diameter of the target lesion;
4. stable disease: neither sufficient shrinkage to qualify for partial response nor sufficient increase to qualify for progressive disease.

Evaluation of tumour response following these criteria is typically performed at six to eight weeks after treatment starts. In this context, the goal of this thesis is to demonstrate that ultrasound tissue characterization techniques are capable of detecting early response to radiotherapy in cell samples and cancer mouse models as early as 24 hours. Radiotherapy was selected as the treatment modality because radiotherapy is currently the most commonly utilized and effective cancer treatment modality, since ionizing radiation targets the entire tumour mass to ensure tumour killing (1).

In this thesis I use ultrasound imaging and tissue characterization techniques to detect responses to radiotherapy *in vitro* and *in vivo*. The method of this detection is based on identifying the changes in ultrasound parameters that are correlated to changes in cellular and nuclear structure following cell death in cell samples and tumour tissues. The findings from this thesis can contribute to clinical cancer research in several ways, briefly outlined in the next paragraphs.

The index of cell death in a tumour, early during the course of the therapy can represent an indication of treatment efficacy (31-33) and can be potentially used to individualize patient therapy. Therefore, the ability to detect cell death in a tumour, within days after the start of radiotherapy, could aid clinicians in making decisions to modify therapy, such as choosing different radiation regimens, adding a radiosensitizer or selecting

different chemotherapy drugs that potentially could result in more effective treatment. This might lead to improved outcomes and the sparing of patients from unnecessary side effects related to ineffective prolonged treatments. Since the method presented in this thesis aims to detect cell death using ultrasound methods, it might be equally applicable to monitor the effects of chemotherapy, photodynamic therapy, *in vitro* and *in vivo*, and might provide new approaches for the development of different experimental therapies in clinical and preclinical studies. The method can be used before treatment starts and regularly during treatment to monitor therapy responses without the need to inject radionuclides or specialized contrast agents as with other techniques (e.g., PET, diffusion-weighted MRI).

Detecting early response to a treatment may provide a new approach to the development of experimental therapies. Currently, new treatments are often assessed in patients with end-stage disease, for whom conventional therapies have usually failed. These are arguably the worst patient groups in which to evaluate novel therapies. By using an imaging technique that could provide an indication of drug efficacy within a few days, as opposed to weeks or months, it might become acceptable to try new treatments in patients who are in the early stages of disease.

Monitoring therapy response is becoming an essential component of drug development in preclinical studies. Ultrasound imaging and tissue characterization of therapy response in animal cancer models allows repeated assessments of the tumour and may provide spatial and temporal information regarding target organs and heterogeneity of response. This information could be correlated with tumour biopsies and histopathological methods to provide the therapy response end-points for this imaging modality.

1.9 Thesis outline

The goal of this thesis is to demonstrate the use of ultrasound imaging and quantitative ultrasound techniques to characterize non-invasively early responses to radiotherapy. I hypothesized that radiotherapy alters the cellular and nuclear acoustical properties and sizes, resulting in observable and measurable changes in ultrasound images and spectral parameters.

After a review of the acoustic scattering theory applied to biological tissues, responses to radiotherapy are characterized *in vitro* in a well controlled environment using cell samples. This *in vitro* work provides the basis for the *in vivo* work that characterizes response to radiotherapy in cancer mouse models. In order to understand the cellular morphological changes responsible for ultrasound scattering at these frequencies, and help the interpretation of experimental data, numerical simulations of ultrasound scattering were conducted, then compared to experimental results from four different cell lines exposed to radiotherapy. Careful analysis of cytology and histology, quantification of cellular and nuclear structural changes following cell death, and the comparison between experimental and simulated data provide new insights into the mechanisms potentially responsible for the increase in ultrasound scattering following cell death. The findings from this study constitute a framework for tumour adaptive radiotherapy in a preclinical setting.

Specifically, Chapter 2 reviews models of ultrasound tissue characterization in the context of the work presented in this thesis. These models lead to the framework that provides a basis for calculating ultrasonic estimates to characterize tissue properties. In Chapter 3, quantitative ultrasonic methods are used to characterize cellular responses to cancer radiotherapy *in vitro*. As indicators of response, ultrasonic integrated backscatter and spectral slope are determined from cell samples. These parameters were corrected for

ultrasonic attenuation. Cellular and nuclear changes in size are assessed, quantitatively and qualitatively, and correlated with changes in the ultrasound parameters. This work allows the study of the mechanisms by which ultrasound is capable of detecting cellular response to radiotherapy *in vitro* in compact aggregates of cells emulating cell arrangements in tissues. In Chapter 4 the responses to radiotherapy *in vivo*, in mouse cancer models, are non-invasively characterized using ultrasound spectrum parameters and parametric images. These findings are compared to the results obtained from the corresponding histological staining. Chapter 5 explores a mechanism to explain the changes in ultrasound backscatter measured from cell samples undergoing different forms of cell death. Based on these findings and on the previous work of Hunt et al (72, 73) a simplified model of ultrasound scattering is proposed and compared to the experimental results. Concluding remarks and suggestions for further studies are presented in Chapter 6.

2 ACOUSTIC SCATTERING THEORY APPLIED TO SOFT BIOLOGICAL TISSUES

2.1 Abstract

The purpose of this chapter is to review the general principles of theoretical models of acoustic scattering and their application to ultrasonic tissue characterization. Historically, biological tissues have been treated either as a continuum with varying density and compressibility or as a discrete distribution of scatterers whose acoustic properties differ from the surrounding medium. Regardless of what theoretical approach is taken, it is recognized that the ultrasound scattering process in biological tissues is primarily affected by the size and acoustic properties of tissue structures responsible for scattering (16). The model of weak scattering in an inhomogeneous medium is discussed in this chapter and is used as a modality to predict scattering in cell samples and tumours. Assuming that tissue scatterers have a certain shape and acoustical properties, and are randomly distributed, simple models to predict ultrasound scattering in biological tissues can be formulated. These models are capable of providing quantitative ultrasound estimates that can be related to underlying tissue structure. Quantitative ultrasound is applied in this thesis to characterize cellular responses to radiotherapy.

Cell samples and tumours contain a tightly packed distribution of cells in which the assumption of a random scattering medium may not hold. To account for the effect of changes in randomization, a simplified model (72, 73) considering scattering from point-like scatterers with regular and more random distributions is presented. This model is used in Chapter 5 to simulate the ultrasound scattering from distribution of point scatterers with different degrees of randomization and the results are compared with experimental data.

2.2 Ultrasound interaction with tissue

Sound propagates through a medium in the form of a wave. The term ultrasound is used to describe vibrations of a material, e.g. biological tissue, that are similar to sound waves, but have frequencies too high to be detected by the human ear. Any sound wave with a frequency higher than 20 kHz is classified as ultrasound.

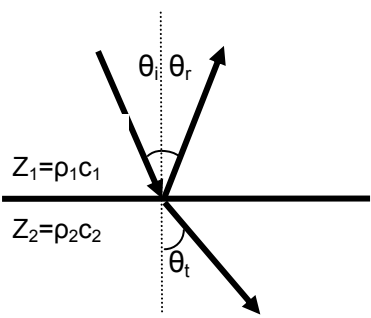
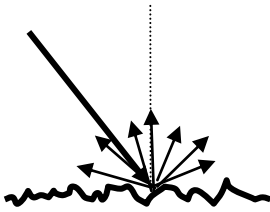
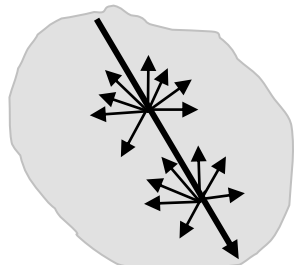
Three important tissue properties are: speed of sound, absorption and scattering. The accuracy of the distance measurements in ultrasound images is determined by our knowledge of the speed of sound in tissues. Speed of sound, however, varies by a few percent for most soft tissue (74). Typically, the speed of sound for longitudinal waves in soft tissues is considered to be approximately 1540 m/s at 37°C. The interactions between ultrasonic waves and soft tissues may be divided into absorption and scattering. The combined effect of these two processes is termed as attenuation. Attenuation causes the ultrasound beam to lose energy thus reducing the signal strength that forms the ultrasound image. Absorption is the transformation of the acoustic energy into thermal energy. Scattering refers to the re-direction of a portion from the travelling wave and occurs when an acoustic wave is incident on an obstacle whose mechanical properties differ from those of the surrounding medium. If the acoustic wave is incident on an obstacle much larger than the wavelength, part of the wave is reflected and the rest is transmitted through the object (refraction) as described by the equation 2.1.

$$R = \frac{Z_2 \cos \theta_i - Z_1 \cos \theta_t}{Z_2 \cos \theta_i + Z_1 \cos \theta_t} \quad 2.1$$

where $Z_1 = \rho_1 c_1$ and $Z_2 = \rho_2 c_2$ (density multiplied by speed of sound) are the acoustic impedances of the medium and the object. The reflection coefficient, R describes the fraction of the acoustic wave that is reflected. The angle θ_i is the incident angle ($\theta_i = 0$ for the normal incidence), θ_t can

be calculated by Snell's Law: $\sin \theta_t = \sin \theta_i \frac{c_2}{c_1}$ (Figure 2.1, A). Acoustic scattering also arises

from structures within a tissue that are approximately the size of the wavelength or smaller and represent a rough or nonspecular reflector surface (Figure 2.1, B and C). The strength of the reflected signal and its frequency content depend on the properties of these structures (e.g., size, density and compressibility), thus ultrasound is highly sensitive to the mechanical properties of tissue structures that often change during disease or cell death. Medical diagnostic ultrasound uses ultrasound energy to map the variations in the acoustic properties of the body and display these as gray-scale images.

A. Specular reflection (surface is smooth with respect to λ)	B. Non-specular reflection (surface roughness $\sim \lambda$)	C. Acoustic scattering, small object reflectors, size $\leq \lambda$
		
<p>Figure 2.1. Ultrasound interactions with boundaries and particles. (A) The incident, reflected and refracted beams at the interface between a media with characteristic velocities c_1 and c_2. The angle of incidence is θ_i, the angle of reflection is θ_r and the angle of refraction is θ_t. (B) As the wavelength becomes smaller, the boundary becomes rough, resulting in diffuse reflections from the surface irregularities; (C) Small particle reflectors within a tissue or organ cause diffuse scattering, giving rise to tissue speckle. <i>Adapted from (75).</i></p>		

2.3 Scattering from single particles

When a sound wave propagates through a homogeneous medium, it encounters a region of different density and compressibility and some of the original wave is deflected from the initial course. The difference between the actual wave and the undisturbed wave, which would be present if the inhomogeneity were not there, is defined as the scattered wave (76).

Rayleigh (77) derived the equation of the scattered pressure around 1900. Under the assumption that the particle is much smaller than the wavelength and thus, senses a uniform field, the scattered pressure radiated by a small spherical particle is given by:

$$p_s(r, \theta) = P_0 e^{-ikr} \frac{k^2 a^3}{3r} \left[\frac{\kappa_1 - \kappa_0}{\kappa_0} + \frac{3(\rho_1 - \rho_0)}{2\rho_1 + \rho_0} \cos \theta \right] \quad 2.2$$

where $P_0 \exp(-ikr)$ is the incident pressure wave (p_i), the time harmonic dependent term $\exp(i\omega t)$ is assumed and thus omitted and P_0 is the amplitude of pressure in the incident wave. The other terms in the equation are: p_s is the scattered pressure amplitude at the scattering angle θ and distance r away from the scattering particle, k is the wave number defined as $k = 2\pi/\lambda$ for a wave of frequency f , ρ_0 and κ_0 are density and compressibility for the surrounding medium, the scatterer has a radius a , density ρ_1 , compressibility κ_1 , and θ is the angle between the incident and scattered wave. This equation is valid for $ka \ll 1$, where a practical upper limit of the scatterer radius for Rayleigh scattering is $ka = \pi/10$ (78).

For larger particles, $ka > 1$, part of the scattered wave is spread out more or less uniformly in all directions (the wave is not in phase over the whole scatterer diameter), part of the scattered wave interferes with the incident field and a variety of complex interference and resonance phenomena occur. In these conditions, the exact solutions for scattered pressure from a spherical object has been derived and experimentally confirmed by Faran (79):

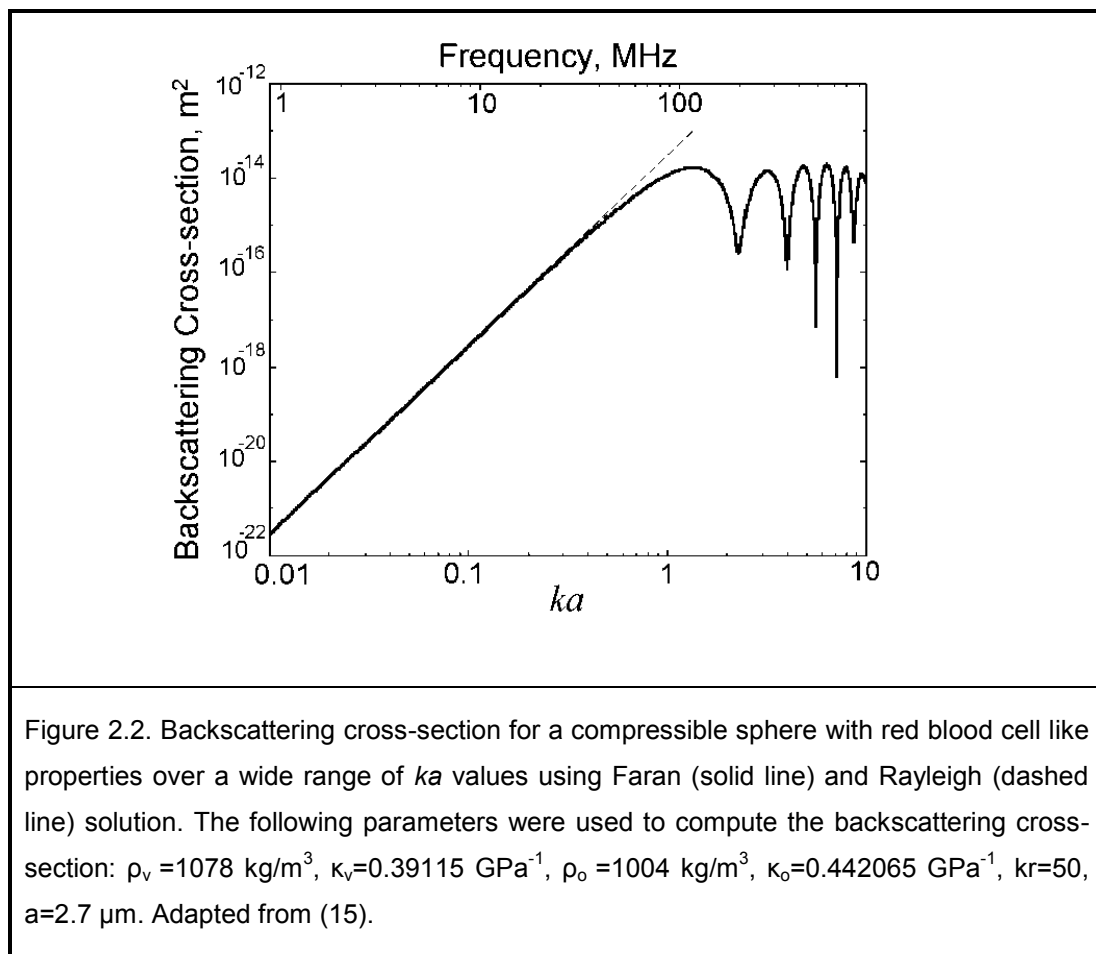
$$p_s = -P_0 \sum_{m=0}^{\infty} (2m+1) (-i)^{m+1} \sin \eta_m \exp(i\eta_m) [j_m(kr) - n_m(kr)] P_m \cos \theta \quad 2.3$$

where P_0 is the amplitude of pressure in the incident wave, c is the longitudinal speed of sound in the medium, k is the wave number, η_m is a term accounting for the properties of the scatterer, $P_m \cos \theta$ is the Legendre polynomial, j_m is the spherical Bessel function of the first kind and n_m is the spherical Bessel function of the second kind.

In most experimental situations, the transducer, considered to be placed far away from the scattering volume, has a finite aperture and therefore only a fraction of the total scattered power is sampled. This is the differential scattering cross-section, defined as the power scattered into a unit solid angle divided by the product of the incident intensity and the scattering volume. Of major importance to ultrasound imaging is the backscattering cross-section that is the differential scattering in the opposite direction to the incident beam for $\theta=180^\circ$.

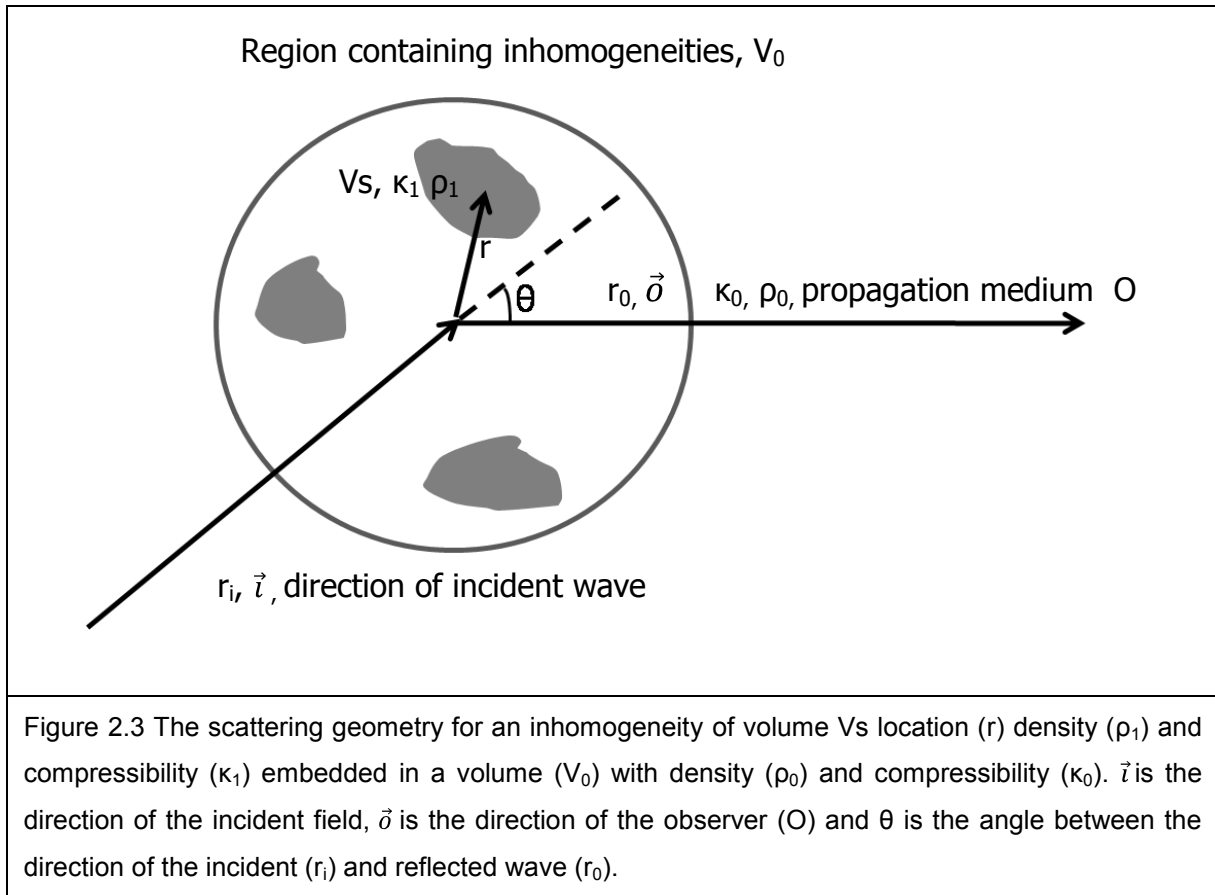
The Faran and Rayleigh solutions for the backscattering cross section of a red blood cell as a function of ka are presented in Figure 2.2. The Faran's solution accurately predicts the differential backscattering cross section at a distant observation point from a single target in a fluid like medium at all ka . It also accounts for the effect of the shear waves (transverse wave consisting of oscillations perpendicular to the direction of wave propagation). For $ka \ll 1$, both the Rayleigh and Faran's solutions predict the same values and an increase of the backscattering cross-section with the fourth power of frequency (Figure 2.2). The backscattering strength is very sensitive to changes in particle size $\sim a^6$ within the Rayleigh scattering regime. However, within this regime the frequency dependence of scattering is almost constant for a relative large range of particle sizes, $\sim f^4$, and therefore, less sensitive to changes in particle size over a large frequency range, providing little information about changes in the size of scattering structures in the analyzed medium. As the ultrasound frequency increases to $ka \leq 1$, the ultrasound wavelength approaches the scale of scattering structures and, therefore, the

frequency dependence becomes sensitive to changes in the size of these structures. Within this regime, however, the backscattering cross-section does not provide great discriminatory power. As the ultrasound frequency further increases to $ka > 1$, the interferences between the echoes from the different parts of the spherical scatterer induce a difference between the results of the Rayleigh and Faran model, as presented in Figure 2.2. In this case, the backscattering cross-section presents a complex pattern resulting from the interference of the incident and scattered wave.



2.4 Weak scattering from random distribution of inhomogeneities

The results deduced from Faran's theory are particularly useful for verifying experimental results using simple random test media as scattering structures with well defined shapes e.g., glass or polystyrene microspheres in agar (80). They also provide a "gold" standard against which approximate calculations may be compared (16). However, this method is not directly applicable to scattering from biological tissues, for which the scatterers are non-uniform in composition and irregular in shape. In this case, to accommodate the presence of arbitrary inhomogeneities, a Green's function approach is used as in the derivation given by Morse and Ingard, (76) for scattering of a propagating acoustic wave in a heterogeneous medium. Biological tissues might be regarded as a conglomeration of cells or subcellular components with different acoustical properties than the surrounding tissue matrix. In this case, the density and compressibility at any location r within the inhomogeneous volume V_s , can be represented by the values $\rho_1(r)$ and $\kappa_1(r)$ superimposed on the uniform background values of ρ_0 and κ_0 of a larger volume V_0 , (Figure 2.3).



The total density and compressibility are expressed as:

$$\rho(r) = \rho_0 + \rho_1(r) \text{ and } \kappa(r) = \kappa_0 + \kappa_1(r) \quad \text{inside } V_s \quad 2.4$$

$$\rho(r) = \rho_0 \text{ and } \kappa(r) = \kappa_0 \quad \text{outside } V_s \quad 2.5$$

Considering that scattering is the result of a wave propagating through an inhomogeneous medium and considering some approximations (A1, A2, A3 outlined below), a solution for scattered pressure p_s that accommodates the presence of arbitrary inhomogeneities can be obtained as:

$$p_s(\mathbf{r}) = \frac{Pe^{ikr_0}}{r_0} \frac{k^2}{4\pi} \int_{V_s} [\gamma_k(\mathbf{r}) - \gamma_\rho(\mathbf{r})] e^{-k(\bar{\sigma}-\bar{\tau})r} dV \quad 2.6$$

where: $\gamma_\rho(\mathbf{r}) = \frac{\rho_1(\mathbf{r})-\rho_0}{\rho_0}$ and $\gamma_k(\mathbf{r}) = \frac{\kappa(\mathbf{r})-\kappa_0}{\kappa_0}$ are the relative variations in density and compressibility and $\theta=180^\circ$ (backscatter). This is a classical result describing the scattering of sound in an inhomogeneous medium (76). The terms on the right side describe the scattering of sound by fluctuations about the average acoustic properties of the medium and are commonly referred as *scattering sources*. The term 'source' is potentially misleading since the inhomogeneities do not introduce any new energy into the pressure field: they 'generate' scattered sound by an interaction with the incident pressure wave.

The solution derived by Morse and Ingard, (76) using a Green's function approach is valid within the following approximations (A1-A3):

A1. Born approximation: it is assumed that the scattered wave amplitude is much smaller than that of the incident pressure, thus the incident wave remains unchanged as it progress through the scattering volume $p(\mathbf{r})=p_i(\mathbf{r})+p_s(\mathbf{r})\approx p_i(\mathbf{r})$. This is valid only if the scattering is weak: $\gamma_\rho(\mathbf{r})$ and $\gamma_\kappa(\mathbf{r})$ are very small (i.e., $\gamma_\rho(\mathbf{r}), \gamma_\kappa(\mathbf{r}) < 0.1$ for the first order Taylor series approximation to be accurate). For a weak scatterer, the solution derived by Morse and Ingard and Rayleigh model are in good agreement in the long wavelength limit (15) more exactly for $ka \leq 0.35$ (81). However, unlike the Rayleigh model, the model derived using the Born approximation remains in close agreement with the exact theory, equation 2.3, up to wavelengths comparable to the size of the scatterer $ka=1$ (81). The limitation in the Born approximation lies in the assumption that the scattered field is much smaller than the incident field in the region of the scatterer and thus multiple scattering is negligible. This assumption holds in structures with tissue like properties as indicated by Couture in his PhD thesis (82). He

calculated the secondary scattering ratio for one of the cell lines used in this work, AML (acute myeloid leukemia). The calculation has been based on the work of Chin (83) that defines as significant a secondary scattering ratio of 10%. It was concluded that cells are weak scatterers and have to be closer than their own diameters in order for their scattered pressure to be significantly affected by multiple scattering. The Born approximation has been used in the analysis of all scattering measurements in tissue (16).

A2. Far-field approximation: the distance from the observation point (O) to the volume of scatterer is large compared to the size of the volume occupied by scatterers ($r_0 \gg r$) (Figure 2.3).

A3. The incident pressure field is approximated by a plane wave: $p_i(r) = P e^{ikr_0}$. This plane-wave result may also be extended to include scattering from focused transducers (49) as the plane wave approximation is applicable to the focal zone of the transducer, as used in this work. For small density and compressibility fluctuations (e.g., $\gamma_\rho(r)$, $\gamma_\kappa(r) < 0.1$) the backscatter pressure field is proportional to the relative fluctuations in the plane wave acoustic impedance, hence the equation 2.7 becomes:

$$p_s(r) = \frac{P e^{ikr_0}}{r_0} \phi(\vec{K}) \quad \text{where } \phi(\vec{K}) = \frac{k^2}{4\pi} \int_{V_s} [\gamma(r)] e^{-i\vec{K}r} dv \quad 2.7$$

$$\vec{K} = k(\vec{o} - \vec{i}) \quad \text{and } \gamma(r) = \frac{\Delta\rho}{\rho_0} - \frac{\Delta\kappa}{\kappa_0} = \frac{-2\Delta z}{z} \quad \text{where } z = \sqrt{\rho/\kappa} \text{ is the acoustic impedance}$$

and $\phi(\vec{K})$ describes the spatial frequency dependence of the scattered pressure by an inhomogeneity of varying density and compressibility without any limiting assumptions about its shape or size. Under these approximations, the scattered pressure from the scattering volume V_s is proportional to the Fourier transform of the scattering sources $\gamma_\rho(r)$ and $\gamma_\kappa(r)$.

Ultrasound imaging is typically performed on collections of particles (e.g., red blood cells) or complex structures such as tissues and the resulting scattered wave is affected by the interference of scattered waves from each particle in the collection. From the previous equation, the scattered field from an ensemble of randomly positioned inhomogeneities is the sum of the individual pressure fields from each inhomogeneity:

$$p_s(\mathbf{r}) = \frac{P e^{ikR}}{R} \frac{k^2}{4\pi} \sum_{j=1}^N \int_{V_s} [\gamma_j(\mathbf{r}_j)] e^{-i\vec{k}\mathbf{r}_j} dV_j = \frac{P e^{ikR}}{R} \sum_{j=1}^N \phi_j(\vec{K}) \quad 2.8$$

where \mathbf{r}_j is the position of the j^{th} particle with respect to origin, N is the total number of inhomogeneities in the scattering volume V_0 and R is the distance from the volume occupied by scatterers to the observation point O .

The scattered wave from a collection of scatterers results from a term that arises from the reflection of the overall structure of the volume (V_0) of scatterers (the coherent scattering contributions) and a term that arises from the random fluctuations of acoustical properties within the population of scatterers that accounts for the contributions from all scatterers in the insonified volume (V_0) (the incoherent scattering contributions) (15). In practice, it is often assumed that measurements are made from a sample volume that lies within a region whose average acoustic properties are the same as the entire volume. Under this assumption, the coherent term is zero and only the incoherent intensity is considered (15).

Under this assumption, the differential backscattering cross-section per unit volume (backscattering coefficient) can be written as:

$$\sigma_b = \frac{k^4 \bar{V}_s}{16\pi^2} n\gamma_0^2 \int_{-\infty}^{\infty} b_\gamma(\Delta\mathbf{r}) e^{-i\vec{K}\Delta\mathbf{r}} d^3\Delta\mathbf{r} \quad 2.9$$

where n is the average concentration of scatterers per unit volume or number density, \bar{V}_s is the average scatterer volume, γ_0^2 is the mean square acoustic impedance fluctuation per particle and $b_\gamma(\Delta r)$ is the correlation coefficient. This equation describes the structural properties of the scattering medium in terms of the average particle size, shape, number density and scattering strength per particle and depends on the ultrasound frequency used to analyze the scattering medium.

The correlation coefficient, $b_\gamma(\Delta r)$, is a statistical measure of similarity in density and compressibility of two scattering inhomogeneities in V_0 separated by Δr and averaged over the ensemble. It may be used to model scattering in terms of the underlying structure of the medium. The correlation coefficients widely used in literature to model scattering in tissue are, the fluid sphere, Gaussian, and exponential functions (16, 58). These functions, first used to describe electromagnetic and acoustic scattering in the ocean and atmosphere, are also used in biomedical applications because they offer simple mathematical solutions that correspond to the measurements in tissue (16, 58). The correlation models of ultrasound scattering (80, 84) are simple in form but do not adequately describe tissue scattering. At long wavelengths ($ka < 1$) the choice of the model is not critical because all the models converge (80). Experimental results using glass-in-agar media have shown that it is possible to estimate an average particle size and an average particle strength (66-68, 85). These results agree well with theoretical predictions in the transition regime of $0.5 < ka < 1.2$ provided the scattering material does not support shear waves or is fairly rigid and dense (80), the assumptions A1-A3 hold for the scattering medium and the scattering structures are randomly distributed. Considering that the potential scatterers are at the level of *cellular structures*, the frequencies of 10-30 MHz chosen in this study allow working within this transition regime and hence, are more sensitive to changes in cellular structure than conventional ultrasound used in clinical routine imaging. Higher-order effects not included in the correlation models (e.g., resonance phenomena) have

considerable influence on the scattering energy for $ka > 1.5$ and for materials that support shear waves (80).

The Gaussian scatterer model (equation 2.10) has been used in many studies to model the backscatter power spectra from soft tissues and obtain estimates of scatterer properties (43, 53, 60, 66, 67, 80):

$$b_{\gamma}(\Delta r) = e^{-\Delta r^2/2d^2} \quad 2.10$$

In this equation, d is the correlation distance. Typically, the error between the log of the normalized experimental power spectrum and the log of the theoretical normalized power spectrum is minimized using a Gaussian form factor as compared to other factors (exponential and spherical shell) (86, 87). Based on this consideration, the Gaussian factor is used in the last part of this thesis (Chapter 6) to estimate the average effective scatterer size in mouse tumours and cell samples. These results were compared with the average size of the tissue structures (e.g. cells and nuclei) evaluated from histological sections.

2.4.1 Rationale for quantitative ultrasound

Conventional medical ultrasound B-mode images are constructed from envelope-detected radio-frequency (RF) backscattered signals. The B-mode images are good at displaying large-scale structures (larger than the wavelength) because simple tissue interfaces such as organ boundaries produce well-defined RF-backscattered signals whose envelopes are clearly detected. However, most structures of interest including organ parenchyma and tumours, contain a complex spatial distribution of mechanical properties that results from the complex internal microstructure of biological tissues. RF backscattered signals from these structures exhibit interference patterns arising from closely spaced scatterers which are not resolved because of their backscattered signals that overlap in time. B-mode images reflect this

complexity, exhibiting an average gray-scale level (indicative of average scattering strength) with a certain speckle pattern that depends on tissue characteristics. This speckle pattern consists of bright and dark spots resulting from the interference among waves scattered by different tissue constituents. Clinicians interpret the speckle pattern on the basis of boundary geometry, internal brightness and texture but not much information can be inferred about the properties of the underlying tissue structure.

To quantify smaller scale structures (smaller than the wavelength), a number of investigators (43-68) have developed techniques to examine the frequency-dependent RF data. The frequency dependent backscatter signals provide information about the size, number, relative impedance and spatial arrangement of the scattering regions within a tissue. Characterization of tissue microstructure by examining the frequency-dependent information of ultrasound backscatter spectra can be categorized as quantitative ultrasound (QUS). The QUS estimates describe the statistical properties of tissues or cell samples lying within a well defined region of interest (ROI).

2.4.2 Relating power spectra to tissue microstructure

Quantitative ultrasound spectral parameters can be computed by comparing the backscatter power spectrum calculated from a region of interest of the investigated tissue with a theoretical power spectrum. The theoretical power spectrum can be modeled from a three-dimensional spatial autocorrelation function describing the distribution of acoustic impedances in a sample. As shown previously, in equation 2.7, tissue structures can be characterized in terms of a stochastic spatial distribution of acoustic impedances z , that exhibit small fluctuations Δz about its mean value. Ultrasound spectrum measurements for tissue characterization are

typically performed by selecting a ROI in the analyzed tissue and applying a Hamming¹ weighting function to the backscattered RF signals within that ROI to suppress spectral lobes.

In this thesis, I apply the derivation of the theoretical power spectrum as described by Lizzi et al (49, 88). This derivation uses a Gaussian correlation function to describe the impedance fluctuations and incorporates the effect of the Hamming window and the beam pattern of a weakly focused transducer resulting in:

$$W_{\text{theor}}(f) = \frac{185 Lq^2 a_{\text{eff}}^6 n z_{\text{var}}^2 f^4}{[1+2.66(fqa_{\text{eff}})^2]} e^{-12.16f^2 a_{\text{eff}}^2} \quad 2.11$$

where q is the ratio of the transducer aperture radius to the distance from the ROI (typically chosen in the transducer focal region), L is the length of the Hamming window, a_{eff} is the effective scatterer radius, n is the average concentration of scatterers per unit volume and $z_{\text{var}} = (Z - Z_0)/Z_0$ is the fractional change in the impedance between the scattering particle of impedance (Z) and the surrounding medium of impedance (Z_0). The exponential term is the Gaussian form factor term in the frequency domain. Continuous isotropic media are characterized by the correlation distance d , equation 2.10, whereas discrete isotropic media are characterized by an average scatterer radius $a_{\text{eff}} = 1.55d$ (16).

The average power spectra measured from various tissues have exhibited a quasilinear shape when expressed in dB in most of the clinical observations (43, 44, 52, 55, 63, 89, 90). Therefore, it was considered a valid approach (53) to apply linear regression analysis to equation 2.11. The expressions of three spectral parameters can be derived (from each two are independent) by applying linear regression analysis directly to $10\log W_{\text{theor}}$ in equation

¹ Smoothly shaped curve commonly used to extract portions of the signal without discontinuities at the edges. It is defined as *Hamming Window* (n)= $0.54-0.46\cos(2\pi n/N)$ where N is the width of the window expressed in samples and n is the sample index.

²The relation between the correlation distance d and a_{eff} is deduced from: $V_s = \int_{-\infty}^{\infty} b_{\gamma}(\Delta r)dv = (2\pi d^2)^{3/2} = 4\pi a_{\text{eff}}^3/3$ using equation 2.11 for b_{γ} .

2.11 (53, 88). These parameters are: the midbandfit (MBF, the value of the regression line at the frequency (f_c) corresponding to the middle of the bandwidth), spectral slope (SS, the slope of the regression line) and spectral intercept (SI, the value of the regression line at 0 MHz). A figure with representation of these parameters is presented below (section 2.4.3)

Assuming a Gaussian scattering model, these parameters can be derived as a function of transducer specifications, effective scatterer radius and scatterer acoustic concentration (acoustic concentration= nz_{var}) (53). For example, SS can be expressed as a function of fractional bandwidth (b)= $\text{transducer bandwidth (B)}/f_c$, and average effective scatterer radius:

$$SS = 26.06 \frac{\left[b - \left(1 - \frac{b^2}{4}\right) \ln\left(\frac{2+b}{2-b}\right) \right]}{b^3 f_c} n - 105.5 f_c a_{eff}^2 \quad 2.12$$

where $n=2, 3$ or 4 representing planar, cylindrical or isotropic scatterers, the units for frequency are MHz and the units for a_{eff} are mm.

Therefore, in terms of tissue properties, the theoretical expression of SS depends only on the effective scatterer size of the predominant scattering structure in the analyzed sample. This dependence of SS with scatterer size is presented in Figure 2.4 for transducer specifications that match the transducer used in the experiments presented in this thesis.

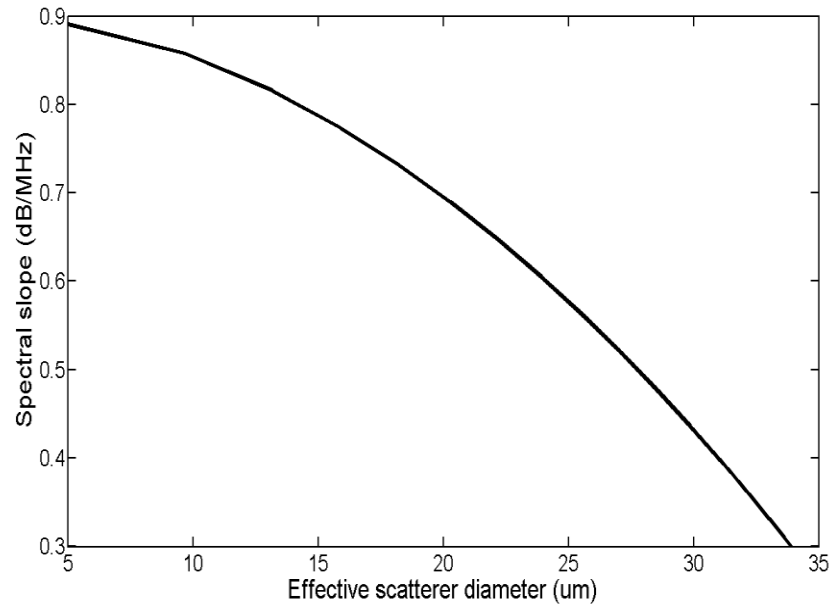


Figure 2.4. The theoretical relationship between the effective scatterer diameter and spectral slope. The transducer has a center frequency of 20 MHz and a -6dB bandwidth of 11 to 29 MHz.

2.4.3 General principles of spectrum analysis

Spectra are frequently used to analyze complex signals, and they have proven useful in voice print analysis, sonar and radar. Analogous techniques can be applied to light analysis for diverse applications such as colorimetry and spectrophotometry. In ultrasonic tissue characterization, normalized spectral analysis allows instrument factors to be suppressed, and provides a methodology to characterize complex tissue architecture.

Correction of system factors within the transducer focal zone is accomplished by using a calibration spectrum derived from the front surface of a normally insonified flat quartz placed in the transducer focus. The calibration spectrum describes the properties of the transducer, electronic pulser and amplifier, all of which influence tissue spectra. The calibration procedure consists of dividing the spectra of cell samples and tissues with the calibration spectrum to

remove the effects of instrumentation dependent factors. The result of these operations is shown in Figure 2.5 which depicts the RF signal from a tissue sample with its uncalibrated spectrum (expressed in dB). The uncalibrated spectrum is heavily influenced by system factors and its shape resembles that of the calibration spectrum. In contrast, the calibrated spectrum has a quasilinear shape and describes the tissue reflectivity referenced to a standard reflector.

The averaged backscatter power spectrum describes the frequency dependence of scattering in the analyzed medium. Frequency-dependent attenuation will affect the averaged backscatter power spectrum and if not compensated for, will give rise to inaccurate estimates of tissue properties. The compensated power spectrum is represented by:

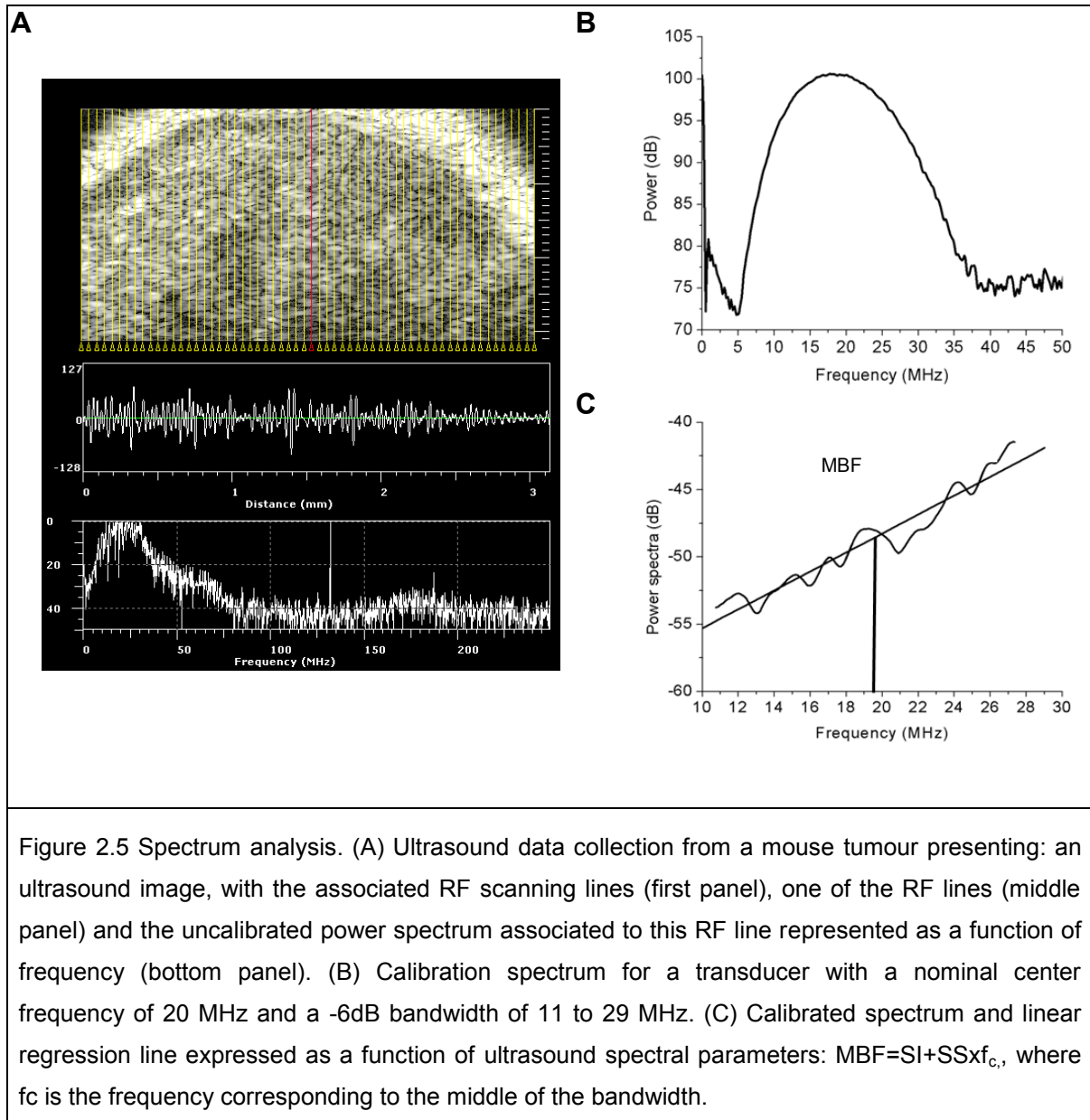
$$W_{\text{comp}}(f) = W_{\text{meas}}(f) e^{2\alpha_0(f)x_0} e^{-2\alpha(f)x} / 2 \quad 2.13$$

where W_{meas} is the averaged measured backscattered power spectrum, $\alpha_0(f)$ is the power attenuation coefficient in the intervening sample (assumed constant), x_0 is the propagation distance in the intervening sample, $\alpha(f)$ is the power attenuation coefficient in the selected ROI (assumed constant) and x is the propagation distance in the selected ROI. The factor of 2 in both exponentials accounts for a two-way beam path. The two-way beam path in the selected ROI is averaged in the second exponential, resulting in the cancellation of this factor.

Depending on the heterogeneity of the analyzed tissue, the calibrated spectra of RF signals from different individual scan lines within the same sample may vary significantly. In spite of this, the average power spectrum of RF signals derived from calibrated spectra from several ROIs within the same tissue sample yields a relatively smooth function of quasilinear shape that can be used to characterize mean tissue properties (27, 39, 49, 50, 52, 53, 55, 88). The spectral parameters, SS, MBF and SI are determined from the linear regression analysis applied to the calibrated spectrum (Figure 2.5, C). The SS measures the frequency dependence of scattering

and provides estimates of effective scatterer size when compared with theoretical predictions, as presented in equation 2.12. The SI is a measure of the effective scatterer size and acoustic concentration (53, 55). Ultrasound integrated backscatter (UIB) is representative of the area under the calibrated RF spectra over the -6dB bandwidth of the transducer. UIB has similar properties to MBF and represents a measure of the overall scattering strength in the analyzed sample. It depends on the scatterer size, relative acoustic impedance and spatial arrangement of scatterers.

Two modes of spectrum analysis are typically used for tissue evaluation: analysis of large-region-of-interests (ROIs) and parametric-images. The large-ROI mode computes the average power spectrum of RF data within ROIs, usually defined by simple shapes (e.g., rectangular). For many long-term studies, the large-ROI mode has been the method of choice in constituting clinical data bases in order to develop tissue classifiers for diagnosis, evaluation and monitoring (44, 50, 91). The parametric-image mode uses small, sliding windows to compute local spectral-parameter values and displays them as color pixel values. Parametric images can be used to depict the spatial distribution of the spectral parameters (e.g., MBF, SS and SI) that are related to tissue scattering properties (52, 55, 66, 91, 92), and hence can detect tissue type distribution, i.e. discern between healthy and cancerous tissue. Furthermore, parametric images are not restricted to simple rectangular regions allowing evaluation of areas with irregular boundaries.

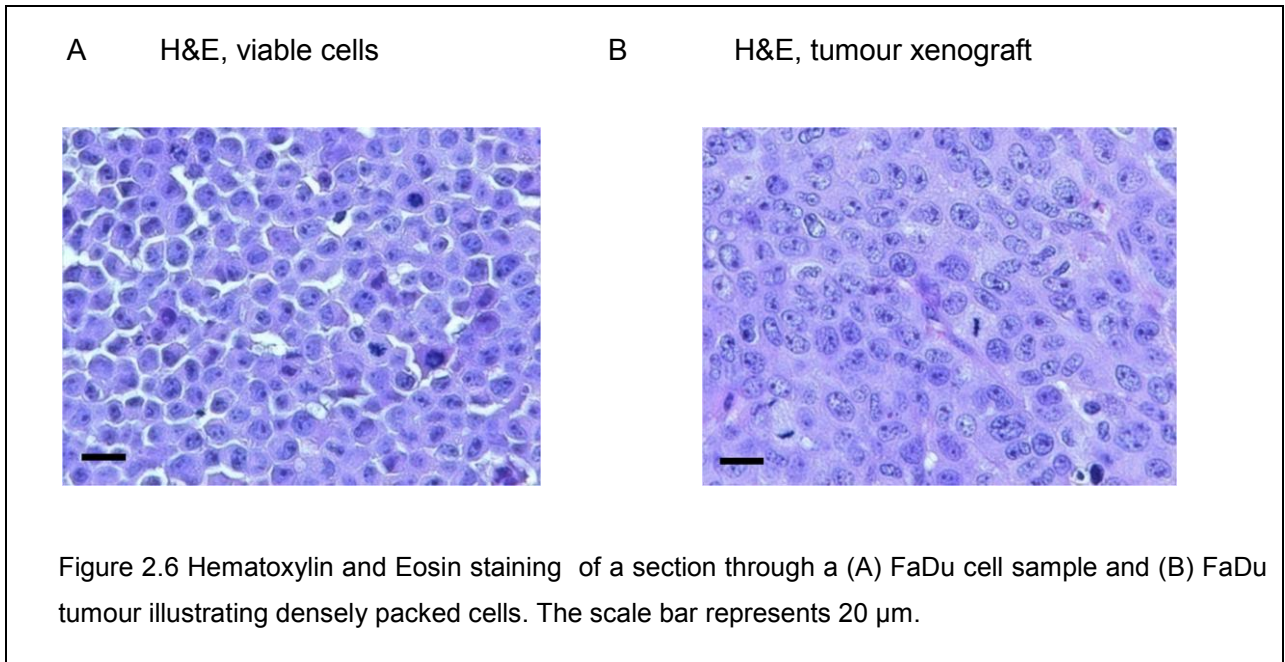


2.5 Scattering by populations with non-random distribution of scatterers

2.5.1 Background

Historically, the established scattering models in biological tissues assume that scatterers are randomly distributed. Under this assumption, regardless of what theoretical approach is taken, e.g. discrete or continuum scattering model, it is recognized that ultrasound scattering increases linearly with the concentration of scatterers and is primarily affected by the size and acoustic properties of tissue scattering structures and their relationship to the ultrasound wavelength, as discussed in the previous section 2.4. For random distribution of scatterers, it can be also demonstrated that an increase in the variance of the scatterer volumes yields an increase in the backscattering coefficient (15).

The assumption of randomly distributed scatterers may not hold in cell samples or tumours with tightly packed cells. For example, in modeling the scattering from red blood cells, red blood cells are considered densely packed and the positions of any pair of adjacent cells are correlated when the average separation between cells is less than 10% of the cell diameter (16). Cells and nuclei in cell samples and tissues are even more packed than red blood cells (Figure 2.6). Therefore, it is reasonable to consider some correlation between the positions of cells and nuclei in cell samples and tissues. Correlation between the scatterer positions (implying some organization) results in interference effects and this may influence significantly the ultrasound scattering from a distribution of particles (15). Added complexity to the analysis of the results arises if the scatterers, within the analyzed distribution, have different sizes, shapes or acoustic properties, as likely occur in tissues.



The linear relationship between the backscattering coefficient and the concentration of scatterers is lost when the position of a given scatterer is not independent of the location of any other scatterer (the scatterer positions are correlated). This situation has been discussed frequently in the literature based on the evidences of the backscattering from blood (15, 93, 94). For instance, the backscattering coefficient increases linearly with the volume concentration of red blood cells up to a maximum of approximately 16%, after which it decreases, because of the loss of randomness in the position of particles (15). Similar effects, an increase of the backscattering coefficient from nucleated cells up to cell volume fractions between 20% and 30% followed by a decrease, have been reproduced using suspensions of nucleated cells by Baddour et al (95).

To theoretically predict the backscattering coefficient from suspension of red blood cells in this regime (the positions of red blood cells are correlated), a correction factor, called packing factor, has been introduced (15, 96, 97). For a particular case in which all the red blood cells in

the insonified blood volume are identical with a mean scatterer volume of V_c , the model predicts that the backscattering coefficient by blood is given by the equation 2.14:

$$\sigma_b = \frac{\sigma_{bs}}{V_c} HW \quad 2.14$$

where σ_{bs} is the backscattering cross-section of a red blood cell (Figure 2.2), H is the hematocrit and W is the packing factor. The packing factor represents a measure of the degree of the orderliness in the spatial arrangement of the red blood cells and is used to correct for the destructive phase interferences introduced by the increase in correlation between particles. It can be viewed as a measure of orderliness in the spatial arrangement of red blood cells (15). At very low hematocrit when the positions of red blood cells are completely random the packing factor is equal to unity. As H increases, the packing factor decays gradually to zero since closer packing will lead to a greater order. The packing factor is based on the Percus-Yevick pair-correlation function for particles that are identical and radially symmetric (slabs, circles, spheres for $m=1, 2$ and 3). The Percus-Yevick packing factor for hard sphere ($m=3$) expressed as an unknown function of hematocrit (equation 2.15) was first applied to blood by Shung (15, 16):

$$W = \frac{(1-H)^4}{(1+2H)^2} \quad 2.15$$

The equation 2.14 with this expression of the packing factor (equation 2.15) provides a fairly good fit to the observed backscattering by blood under laminar flow conditions (16). This model has been also able to explain the “black” regions in the ultrasound images of high concentrated red blood cells, as being caused by a more regular separation of cells in those regions (15, 94).

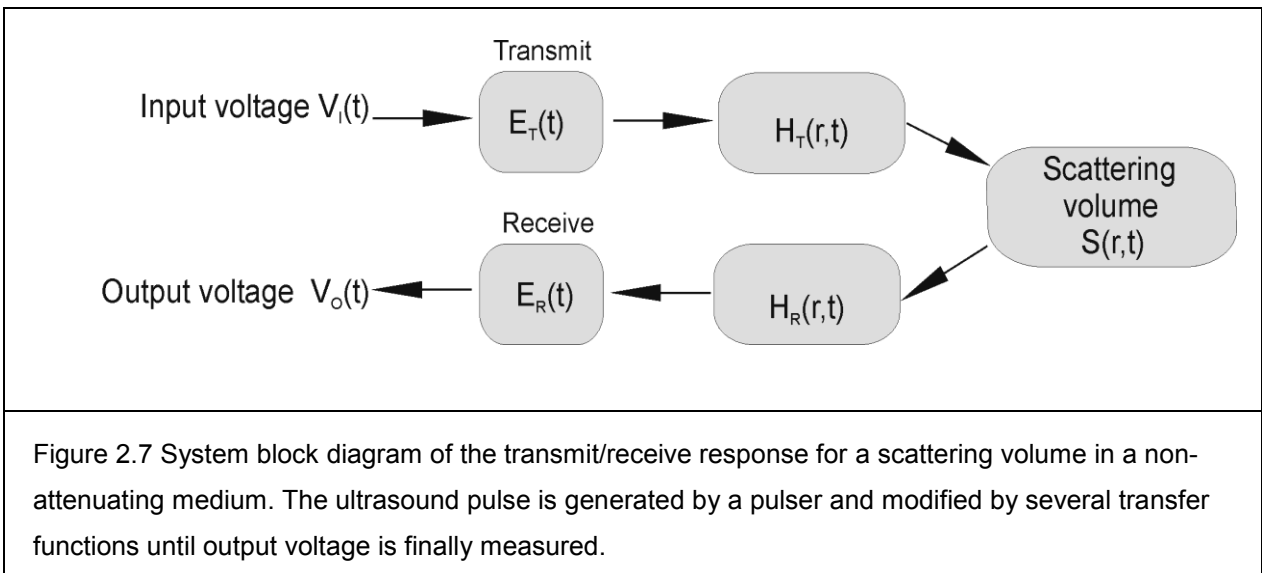
2.5.2 Scattering by regular and more random distributions of point-like scatterers

In the context of understanding how different degrees of randomness in the spatial distribution of scattering sources influence the changes in ultrasound backscatter, large changes in backscatter have been predicted by the model of Hunt et al (72, 73) for point scatterers³ with constant number density but with differing degrees of randomization. The model attempted to explain the acoustic microscope images of spheroids produced by Sherar et al (98). In these acoustic microscope images the backscatter amplitude was constant through small spheroids but increased in cells deprived of O₂ and nutrients. The apparently normal cells had a fairly regular distribution and low backscatter values while the hypoxic cells had pyknotic centers, a highly disorganized distribution and high backscatter values. The model also attempted to explain part of the large changes measured in backscatter ultrasound from apoptotic cells compared to normal cells (26, 36). The cytology of apoptotic cells revealed a more disorganized distribution after exposure to a chemotherapeutic drug. The model predicted an increase of up to four times in the maximum amplitude of backscattered ultrasound for a tissue or cell sample with the same type of cells and same acoustic properties but different spatial distribution of the cell scattering centers (e.g. fairly regular to more random distribution). In a tumour the differences in backscatter intensities could be due to changes in cellular properties (e.g., size, acoustic impedances) and could be linked to different degrees of randomness in the spatial distribution of scattering sources. Therefore, part of the increase in backscatter during the sequence of cell death may be the result of varying degrees of scatterer randomization induced by the disorganization of tissue structure following cancer treatment. Since the model of weak scattering from randomly distributed inhomogeneities does not take into account the changes in the spatial arrangement of scatterers, the Hunt model will be used

³ A point scatterer does not have a volume and its pulse echo response is a positive delta function or unit impulse function. ($\delta(x) = 1$ for $x = 0$ and $\delta(x) = 0$, for $x \neq 0$).

in this thesis (Chapter 5) to investigate the changes in ultrasound scattering resulting from the increase in randomization of scatterers spatial distribution. An overview of the mathematical derivation of the backscatter signal from regularly spaced and more randomly distributed scatterers (72, 73) is described in this paragraph.

Following the notation adapted by Jensen (99) a model for the scattering process can be summarized by the flow-chart presented in Figure 2.7:



$$V_o(t) = V_i(t) * E_T(t) * H_T(r,t) * S(r,t) * H_R(r,t) * E_R(t)$$

2.16

where :

- $V_o(t)$ is the output voltage from the transducer;

- $V_i(t)$ is the excitation voltage;

- $E_T(t)$ and $E_R(t)$ are the electromechanical responses of the transmitter and receiver transducers; - $H_T(r,t)$ is the transmit spatial impulse of the transducer and $H_R(r,t)$ is the receive spatial impulse of the transducer located at the position r ;

- $S(r,t)$ is the scattering term accounting for perturbations or inhomogeneities in the medium that give rise to the scattered signal;

The transmit–receive pulse-echo electromechanical impulse response of the transducer is defined as:

$$P(t) = V_I(t) * E_T(t) * E_R(t) * S(r,t) \quad 2.17$$

Assuming that the same transducer is used on transmit and receive, equation 2.16 can be rewritten as,:

$$V_o(t) = P(t) * H_T(r,t) * H_R(r,t) \quad 2.18$$

Where $P(t)$ can be modeled as a Gaussian–shaped pulse. Extending equation 2.18 to consider many scatterers within the resolution volume, yields:

$$V_o(t) = P(t) * \sum_{i=1}^N H_T(r_i,t) * H_R(r_i,t) \quad 2.19$$

Where r_i is the position of the i th scatterer and N is total number of scatterers. This equation describes the backscatter signal for the transducer held in one position and for one excitation burst. The problem simplifies when $H_T(r_i,t)$ and $H_R(r_i,t)$ are considered δ functions, thus if the i^{th} scatterer is in the resolution cell of the transducer, a positive delta peak occurs at the time corresponding to the twice distance between the i^{th} scatterer and the transducer. The backscattered signal from the cloud of scatterers can be computed by summing all pulse-echo impulse responses functions before convolution with the transducer pulse function $P(t)$ (equation 2.19). In Chapter 5 of this thesis more detail is presented about the implementation of this model in order to simulate changes in ultrasound backscatter following cell death.

2.6 Structures potentially responsible for ultrasound scattering in tissue

Biological tissues are complex structures consisting of cells of different sizes and different composition interspersed with blood vessels and connective tissue. The complexity of tissue composition and the frequency dependence of scattering, i.e., different scattering structures may predominantly scatter ultrasound within certain ranges of frequency, may be the reason that the fundamental ultrasonic scattering structures in tissue are still unknown. Fields and Dunn (100) proposed that echographic appearance of a tissue may be related to the content of connective tissue because acoustic properties of connective tissue such as collagen and elastin seem to significantly differ from the acoustic properties of other tissue components, e.g., fat, water, protein (16). Later, several investigators confirmed that collagen plays a significant role in determining tissue ultrasonic properties including scattering (101-103). However, Bamber et al (104) showed a poor correlation between the ultrasonic properties and the content of connective tissue in different organs, i.e., liver, spleen and kidney. The reason for this discrepancy might be attributed to the variation in the content of the connective tissue being too small to be detected by ultrasound. Then, it was hypothesized that the size of tissue structures may dominate ultrasound scattering (84, 105). Thus, results from ultrasound studies of scattering from blood, whose composition is much simpler than the majority of other tissues, indicate that small changes in the average size of red blood cells greatly affects ultrasound scattering (15).

The majority of ultrasound tissue characterization work conducted in the past was performed at clinically relevant ultrasound frequencies within the range of 2-10 MHz. At these frequencies, the ultrasound interrogating wavelengths are approximately 150-750 μm , much larger than the typical dimension of a cell or nucleus (10-20 μm). Since the frequency of ultrasound waves determines the scale of scattering structures and the strength of scattering, within this regime, larger tissue structures, larger than cells, act as main scatterers. For example, the Gaussian

model applied to estimate the average scatterer size in the kidney yielded two main scattering structures depending on the ultrasound frequencies. Frequencies of 2-7 MHz yielded estimates of average scatterer size of $220 \pm 15 \mu\text{m}$ close to the size of kidney glomeruli ($200 \mu\text{m}$) (16). By increasing the frequency to 16 MHz the same estimation technique yielded average scatterer sizes of $55 \pm 10 \mu\text{m}$ close to the size of kidney tubules ($50 \mu\text{m}$) (16). These results clearly indicate that different structures in tissue will scatter preferentially depending on interrogating ultrasound frequencies. Higher ultrasound frequencies will be sensitive to even smaller structures, e.g., the cell and cell nucleus, as suggested by experiments analyzing the backscatter changes in compact aggregates of cells, within a large range of ultrasound frequencies of 5 to 60 MHz (39, 40, 42, 106). The work of Oelze et al (67, 87) comparing ultrasonic scatterer size estimates with histological sections, suggested that cells or structures in the range of cells are dominant sources of scattering from the mouse models of mammary cancers. Increasing the ultrasound frequency to a range of 30 to 90 MHz (wavelength of $17\text{-}50 \mu\text{m}$), the same estimation techniques yielded scatter size estimates close to that of a cell nucleus (107). Furthermore, investigations in our laboratory on ultrasound backscatter from mono-nucleated HEK and multinucleated HEK cells with larger cell sizes and multiple nuclei (40) and experiments on isolated nuclei of AML cells (42) have indicated that the size of the nucleus, not the size of the cell itself dominates the backscatter in cell ensembles at frequencies of 20 to 60 MHz. Based on these considerations, my working hypothesis in this thesis is that the backscatter characteristics from cell samples or tumour tissue are closely linked to cellular and nuclear acoustic properties. The ultrasound scattering models presented in this chapter and the results presented in Chapters 3, 4 and 5 help in addressing this working hypothesis in Chapter 6.

3 QUANTITATIVE ULTRASOUND CHARACTERIZATION OF CANCER RADIOTHERAPY EFFECTS IN VITRO⁴

3.1 Abstract

In this chapter, I demonstrate the application of quantitative ultrasonic methods to characterize cellular responses to cancer radiotherapy, in a well-controlled environment *in vitro*. The work presented in this chapter allows the study of the mechanism by which ultrasound is capable to assess cellular responses to radiotherapy *in vitro* in compact aggregates of cells emulating cells arrangement in a tissue.

Three different cell lines were exposed to radiation doses ranging from 2 to 8 Gy. Data were collected with an ultrasound scanner using frequencies of 10 to 30 MHz. As indicators of response, ultrasonic integrated backscatter and spectral slope were determined from cell samples. These parameters were corrected for ultrasonic attenuation by measuring speed of sound and attenuation coefficient slope.

A significant increase in the ultrasonic integrated backscatter ranging from 4-7 dB ($p < 0.001$), was found for radiation treated cells compared to viable cells at all radiotherapy doses. The spectral slopes decreased in the cell samples that predominantly underwent mitotic arrest/catastrophe following radiotherapy, consistent with the increase in cell size, whereas the spectral slopes did not change significantly in the cell samples that underwent a mix of cell death including apoptosis and mitotic arrest, with no significant change in average cell size.

⁴ The work presented in this chapter has been published as: Vlad RM, Alajez NM, Giles A, Kolios MC, Czarnota GJ. Quantitative ultrasound characterization of cancer radiotherapy effects *in vitro*. Int J of Radiat Oncol Biol Phys 2008;72:1236-43.

The changes in ultrasound integrated backscatter and spectral slope were direct consequences of cell and nuclear morphological changes associated with cell death. The results indicate that this combination of quantitative ultrasonic parameters has the potential to assess cell responses to radiation, differentiate between different types of cell death and provide a framework to monitor tumour responses *in vivo*.

3.2 Introduction

In clinical oncology and experimental therapeutics, changes in tumour growth rate or volume have traditionally been the first indication of treatment response. These changes typically occur late in the course of therapy. Currently, there is no routinely used imaging modality to assess tumour responses to cancer treatment within hours to days after the delivery of radiation treatment. Computed tomography (CT) and positron emission tomography (PET) imaging or combined CT/PET imaging have been used to assess tumour responses to cancer therapies typically 3 to 4 weeks, after the initiation of the treatment (10, 108). Dynamic contrast-enhanced magnetic resonance imaging (DCE-MRI) measurements have been observed to correlate with immunohistochemical surrogates of tumour anti-angiogenesis (109, 110) within the same time frame. Dynamic contrast-enhanced Doppler ultrasound (DCE-DUS) has been successful in predicting early tumour response in isolated limb perfusion of limb sarcomas (111) within 1 to 7 days after therapy delivery. However, the use of such imaging modalities to monitor the responses of tumours to cancer therapies can be limited either by their cost (DCE-MRI, PET, CT, combined PET/CT) or limited applicability (DCE-DUS). The ability to assess early tumour responsiveness to therapy within days after the start of the treatment, could ultimately aid clinicians in making decisions to modify therapy e.g., choosing different radiation regimens, adding a radiosensitizer or using different chemotherapy drugs that potentially could result in more effective treatment leading to improved outcomes and sparing patients from unnecessary side effects.

The ultrasonic scattering process in biological tissues is primarily affected by the size, acoustic impedance ($Z=p/\kappa$, where p is density and κ is compressibility) and the spatial distribution of the tissue scattering structures. Ultrasonic tissue characterization techniques are based on the premise that disease processes or therapies alter the physical characteristics of

tissue (i.e., compressibility, density and scatterer size) and these alterations cause observable changes in acoustic scattering properties. Characterization of the tissue microstructure by examining the frequency-dependent backscatter has been used to diagnose ocular tumours, cardiac and liver abnormalities (44, 55, 62), differentiate benign fibroadenomas from mammary carcinomas and sarcomas (66) and has provided good diagnostic accuracy in the detection and lesion localization of prostate cancer (52, 57).

The aim of cancer radiotherapy is to kill tumours by inducing cell death including apoptosis and mitotic arrest/catastrophe (1). Currently, standard methods for detecting cell death are invasive and involve special staining. Previous studies have indicated that high frequency ultrasound i.e., 10-60 MHz, is sensitive to apoptosis *in vitro* and *in vivo* (26). The backscatter intensity from apoptotic cells exhibited a significant increase, e.g., up to a sixteen fold increase in comparison with viable cells (27). In addition, the spectral slope was observed to increase significantly for apoptotic cells versus viable cells consistent with nuclear condensation and fragmentation assessed from cytological staining. For the range of the ultrasonic frequencies used in these studies of 10 to 60 MHz, the corresponding wavelengths of 25 to 150 μm approach the cell and nuclei sizes (10-20 μm) and hence are more sensitive to changes in cellular structure than conventional ultrasound (106).

In this chapter, I investigate whether the ultrasonic imaging, ultrasonic integrated backscatter (UIB) and spectral slope (SS) calculated from ultrasonic power spectra can be used in the laboratory to monitor the responses of tumour cells exposed to radiation treatment. The study represents the first evidence of the use of spectral parameters to detect radiotherapy effects *in vitro*, specifically differentiating between cell samples that die predominantly by mitotic arrest/catastrophe from cells that die predominately by a mix of apoptosis and mitotic arrest.

Three different cell lines were used in this study: AML, FaDu and Hep-2. The AML cell line was used as a reference model because the apoptotic response of this cell line to a chemotherapeutic drug was histologically and ultrasonically well characterized (26, 27). The head and neck cancer cell lines (FaDu and Hep-2) were chosen because a main primary treatment modality for head and neck cancers is radiotherapy.

3.3 Methods

3.3.1 Cell preparation

Acute myeloid leukemia cells (OCI-AML-5) (112) were grown from frozen stock samples as described elsewhere (40). Human head and neck tumour cell lines, FaDu and Hep-2, were obtained from American Type Culture Collection (ATCC). Hep-2 was cultured in (α -MEM) supplemented with 0.1% gentamycin and 10% fetal bovine serum (FBS), whereas FaDu was cultured in Eagle's Minimum Essential Media with 2 mM L-glutamine and Earle's balanced salt solution adjusted to contain 1.5 g/L sodium bicarbonate, 1.0 mM sodium pyruvate and 10% FBS. All cell lines were grown in a humidified atmosphere at 37°C, containing 5% CO₂.

Cell samples were irradiated using a small animal and cell irradiator Faxitron Cabinet X-ray System (Faxitron X-ray Corporation, Wheeling, IL, USA). This delivered 160 keV X-rays at a rate of 200cGy/minute and at doses of 2, 4 and 8 Gy. Structural changes that are characteristic of apoptotic and mitotic response (i.e., increase in cell and nuclei size, membrane ruffling, cytoplasm vacuolization, nuclei fragmentation and condensation and formation of apoptotic and mitotic bodies) were used as an indication of responses to radiotherapy. These structural changes were observed in AML cell culture for all applied radiotherapy doses and at 8 Gy for FaDu and Hep-2 cell lines at 48 h after exposure to radiotherapy. The cell samples were

ultrasonically imaged 48 h after exposure to radiotherapy because keeping the treated cells longer than 2 days in the culture would allow the surviving cells to further divide decreasing the chance to effectively image the early radiation effects. The 8 Gy radiation dose is consistent with large palliative doses that are administered in the clinic to obtain appreciable rapid clinical effects.

Before ultrasound data acquisition, cells were trypsinized (Hep-2 and FaDu), washed in PBS (phosphate-buffer-saline) and centrifuged at 1900 g. Parallel samples consisting of untreated (control) and treated cells were prepared by centrifugation in a custom-built sample holder. The sample holder had 3 cylindrical holes of 8 mmx7 mm (diameter x height). Treated and control samples were prepared by centrifugation of cells in two separate wells. The other well, containing PBS, served as a calibration reference. The cell samples were independently prepared in triplicate from different sets of cells.

3.3.2 Ultrasound data acquisition and analysis

A VS40B high-frequency ultrasound device (VisualSonics Inc., Toronto, Ontario) was used to image cell samples. A transducer with a nominal center frequency of 20 MHz and a -6 dB bandwidth of 12-28 MHz was used to collect ultrasound data. Data were collected within the transducer depth of field (3.12 mm), from five different planes containing 40-60 scan lines each and stored digitally at a sampling rate of 500 MHz. The regions of interest (ROIs) chosen to calculate the backscattered power spectra contained 15 to 25 independent scan lines at a distance of 250 μm (the transducer beamwidth at the nominal center frequency) and were 1 mm deep, centered around the transducer focus.

Ultrasound scan lines from each bracketed line segment were multiplied by a Hamming weighting function to suppress spectral lobes and the Fourier transform was computed. The squared magnitudes of the resultant spectra from all ROIs were averaged and divided by the

power spectrum computed from a flat quartz calibration target in order to calculate the normalized power spectra. This procedure removed system and transducer transfer functions to provide a common reference for data collected with various transducers and systems (89). The normalized power spectra were compensated for frequency dependent attenuation according to Taggart et al (40). The resulting normalized power spectra were integrated over the transducer - 6 dB bandwidth to calculate the UIB. Linear regression analysis was used to calculate the SS from the normalized backscatter power. The SS is an indicator of effective scatterer size and a decrease in SS corresponds to an increase in effective scatterer size when properly corrected for attenuation according to Lizzi et al (55). Further details on the theoretical and signal analysis considerations can be found elsewhere (44, 49).

The speed of sound (SOS) and attenuation coefficient slope (ATS) were obtained by repeating each of the measurements on three different ROIs on the same cell sample. A time-of-flight method (74) was used to calculate SOS. The SOS was used to calculate the thickness of the cell sample ($D = \text{SOS} \times t$, where t is the time difference between the arrival time of the echo from the top of the cell sample to the bottom of the well containing the cell sample). The thickness of the cell sample was used to calculate the ATS as a function of frequency using a broadband technique (74). Detailed presentation of SOS and ATS, data collection and analysis, are described in a recent publication (40).

3.3.3 Statistics.

The statistical analysis was performed using GraphPad Prism (GraphPad Software, San Diego, California, USA). A t-test was applied to each combination of conditions and a $p < 0.05$ was considered significant. The ultrasonic parameters calculated from all ultrasound scan lines for one treatment condition, considered as one population, were compared against the ultrasonic parameters computed from the corresponding control sample for FaDu and Hep-2 cell

lines. One way ANOVA was applied to test the changes in the ultrasonic parameters calculated from all three treatment conditions considered for AML cell line. The Bonferroni correction was applied to the probability value and $p < 0.0167$ was considered significant.

3.3.4 Cytological analysis, cell size and morphology measurements

To investigate the morphology of cells at each experimental condition, ultrasonically imaged samples were fixed for 24 hours in 10% buffer formalin, embedded in paraffin and processed as histological sections. Hematoxylin and eosin (H&E) staining and phase contrast microscopy images were used to assess general cell morphology. Cell and nuclear fragment sizes for each experimental condition were measured with a Multisizer3 Coulter Counter (Beckman Coulter, Mississauga, Ontario, Canada) using a 100 μm aperture that allowed precise and reliable particle size measurements in the 5-60 μm range. Flow cytometric analysis using propidium iodide was performed to measure cell DNA content using a FACS caliber (BD Biosciences, Mississauga, Ontario, Canada) as described elsewhere (113).

3.4 Results

The values of ATS, SOS, UIB, cell size and SS for all viable and treated cell samples are presented in Table 1. Statistically significant differences were not observed between ATS and SOS values from viable and irradiated cell samples for each cell line.

Cell type	ATS +/- SE (dB/mm/MHz)	SOS +/- SE (m/s)	UIB +/- SE (dB)	Cell size(μm) +/- variance(μm^2)	SS +/- SE (dB/MHz)
AML control	0.054 +/-0.002	1530 +/-2	-55.4 +/-0.3	10.3 +/-2.3	0.89 +/-0.08
AML 2Gy	0.063 +/-0.005	1501 +/-6	-51.6 +/-0.6	10.4 +/-4.5	0.91 +/-0.05
AML 4Gy	0.060 +/-0.007	1516 +/-5	-48.3 +/-0.5	9.2 +/-5.2	0.84 +/-0.06
AML 8GY	0.055 +/-0.008	1514 +/-3	-49.6 +/-0.6	9.9 +/-4.6	0.85 +/-0.10
FaDu control	0.070 +/-0.002	1532 +/-4	-50.5 +/-0.7	16.6 +/- 7.5	0.53 +/-0.07
FaDu 8Gy	0.068 +/-0.003	1499 +/-2	-46.3 +/-0.8	19.9 +/-19.1	0.34 +/-0.08
Hep-2 control	0.060 +/-0.007	1540 +/-7	-52.3 +/-0.4	17.4 +/- 5.4	0.57 +/-0.04
Hep-2 8Gy	0.059 +/-0.005	1543 +/-3	-45.9 +/-0.6	18.0 +/- 14.1	0.44 +/-0.07

Table 3-1. The ATS, SOS, UIB, average diameter +/- variance and SS measured for all cell samples. SE represents the standard error of the average ultrasonic parameters. Three cell samples were considered for each experimental condition.

The UIB increased for all three cell lines (FaDu, Hep-2 and AML) exposed to radiotherapy, by 3.8-7.1 dB ($p < 0.001$) (Table 1). Figure 3.1 shows two representative ultrasound images of an untreated and treated Hep-2 cell sample corresponding to the UIB values presented in Table 3-1.

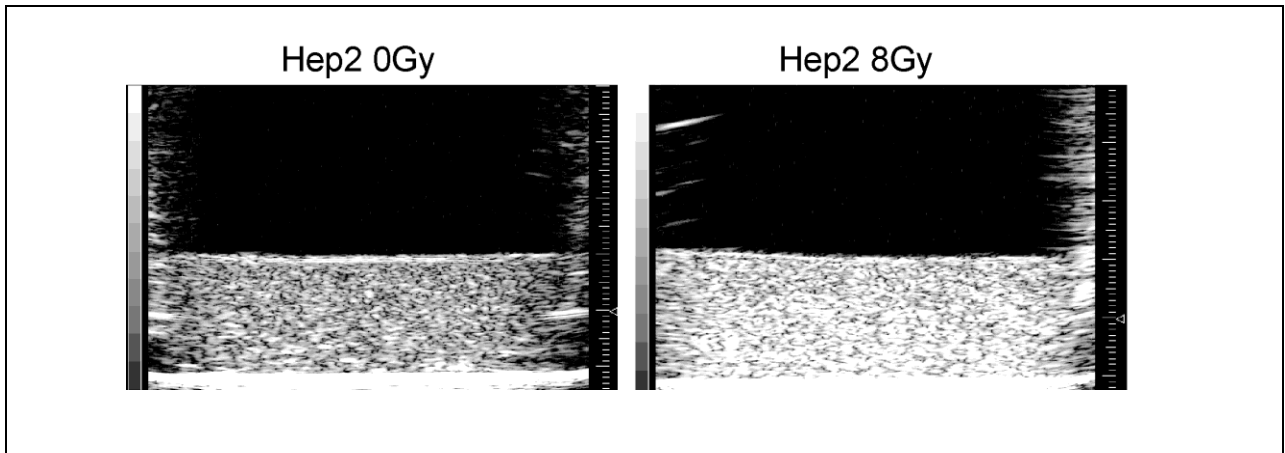


Figure 3.1. Representative ultrasound images of Hep-2 cell samples demonstrating an increase in ultrasound backscatter, observed as an increase in image brightness (~ four-fold increase), after radiation. The height of the cell pellet is ~ 2mm. The smallest division on the scale on the lateral side of each pellet is 0.1 mm. The small triangle on the right side of each cell sample represents the location of the transducer focal point. The hyperechoic line across the bottom of the ultrasound image is the bottom of the sample holder.

The SS can be related to the size of the major scattering structures in a sample (43, 55). In this study, the SS revealed different trends depending on the changes of cell/nuclear sizes following different modalities of cell death. The SS calculated for the AML cell samples did not change significantly between the viable and treated samples and between the samples treated with different radiation doses, (Table 3-1 and Figure 3.2A). The corresponding H&E image of the AML cells treated with radiotherapy exhibited a mix of cell death: apoptosis with nuclear condensation and fragmentation and mitotic arrest with enlarged cells (Figure 3.2A). The SS calculated for Hep-2 and FaDu cell samples decreased with the irradiation dose by 20-40% ($p < 0.05$) as presented in Table 3-1 and Figure 3.2B.

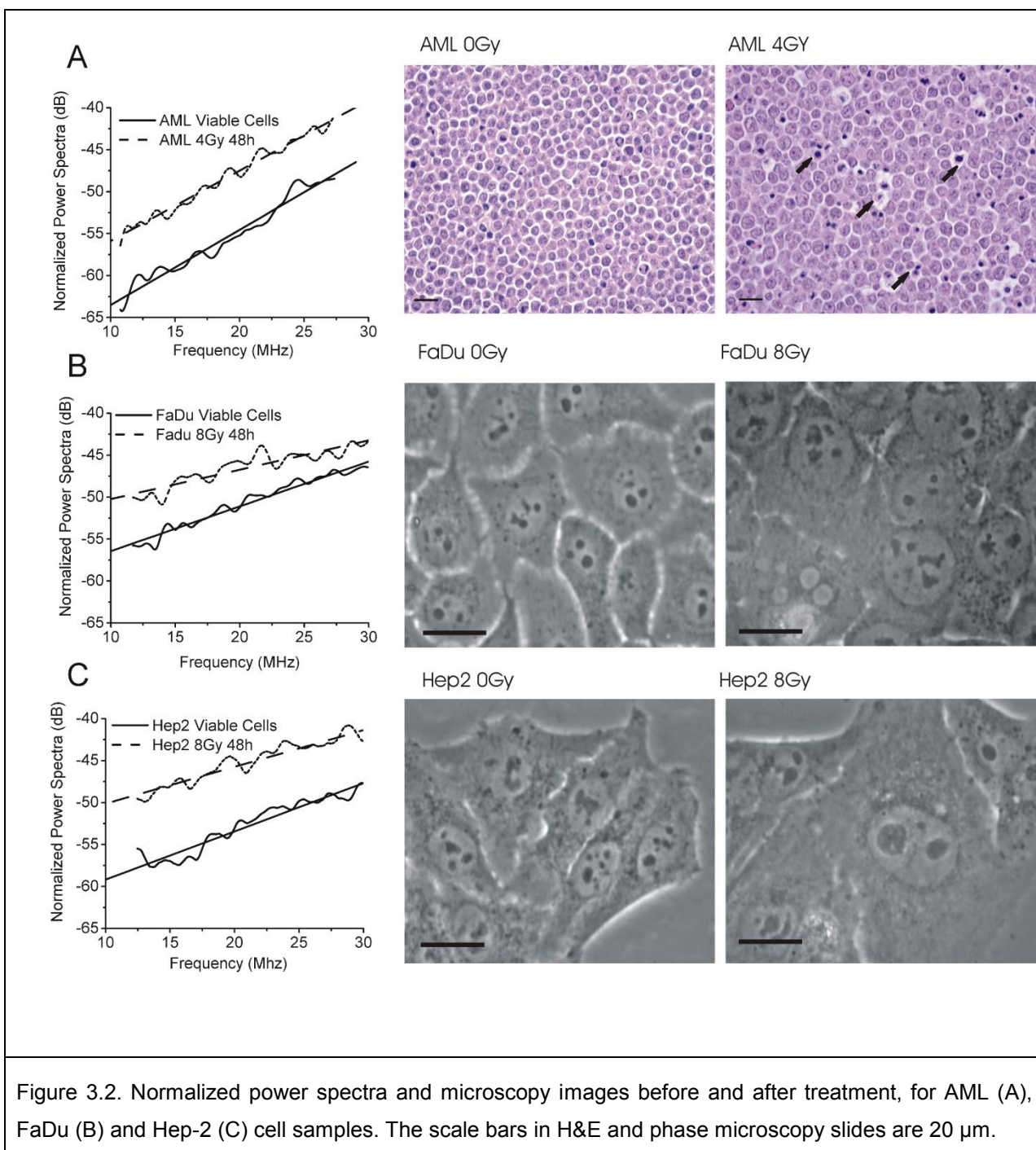


Figure 3.2. Normalized power spectra and microscopy images before and after treatment, for AML (A), FaDu (B) and Hep-2 (C) cell samples. The scale bars in H&E and phase microscopy slides are 20 μm .

The phase contrast microscopy images of the two head and neck cancer cell lines, FaDu and Hep-2, presented morphological characteristics of only mitotic arrest/catastrophe with enlarged cells and nuclei after exposure to 8 Gy radiation dose as presented in Figure 3.2 (B and C). The decrease in the SS can be interpreted as an increase in the average scatterer size,

which is consistent with the observed increase of cell/nuclear sizes. To identify the modalities of cell death following radiotherapy, in addition to histology, flow-cytometric measurements of DNA content were carried out. Because the nucleus becomes fragmented during apoptosis, sub-G₁ fractions were identified as apoptotic cells. The sub-G₁ peak can represent in addition to apoptotic cells, mechanically damaged cells and cell fragments resulted from the advanced stages of cell death, as described in (5, 113). The G₂/M peak was identified as cells in mitosis and mitotic arrest, whereas the peak with higher than double DNA content (higher than in the G₂/M fraction) was identified as cells in mitotic catastrophe. Cells typically die by mitotic arrest/catastrophe after they undergo up to four unsuccessful mitotic cycles as defined in Tannock et al (1). The analysis of the DNA content for AML cell samples demonstrated a mix of cell death by apoptosis, with a 25-fold maximum increase in the sub-G₁ fraction and a 3.5-fold maximum increase in the G₂/M cell fraction, as presented in Figure 3.3A. For the head and neck cancer cell lines no sub-G₁ fractions were detectable but there was an approximately two fold increase in the mitotic cell fraction (G₂/M) and a six to eight fold increase in the mitotic catastrophe (polyploid) cell fraction (Figure 3.3, B and C).

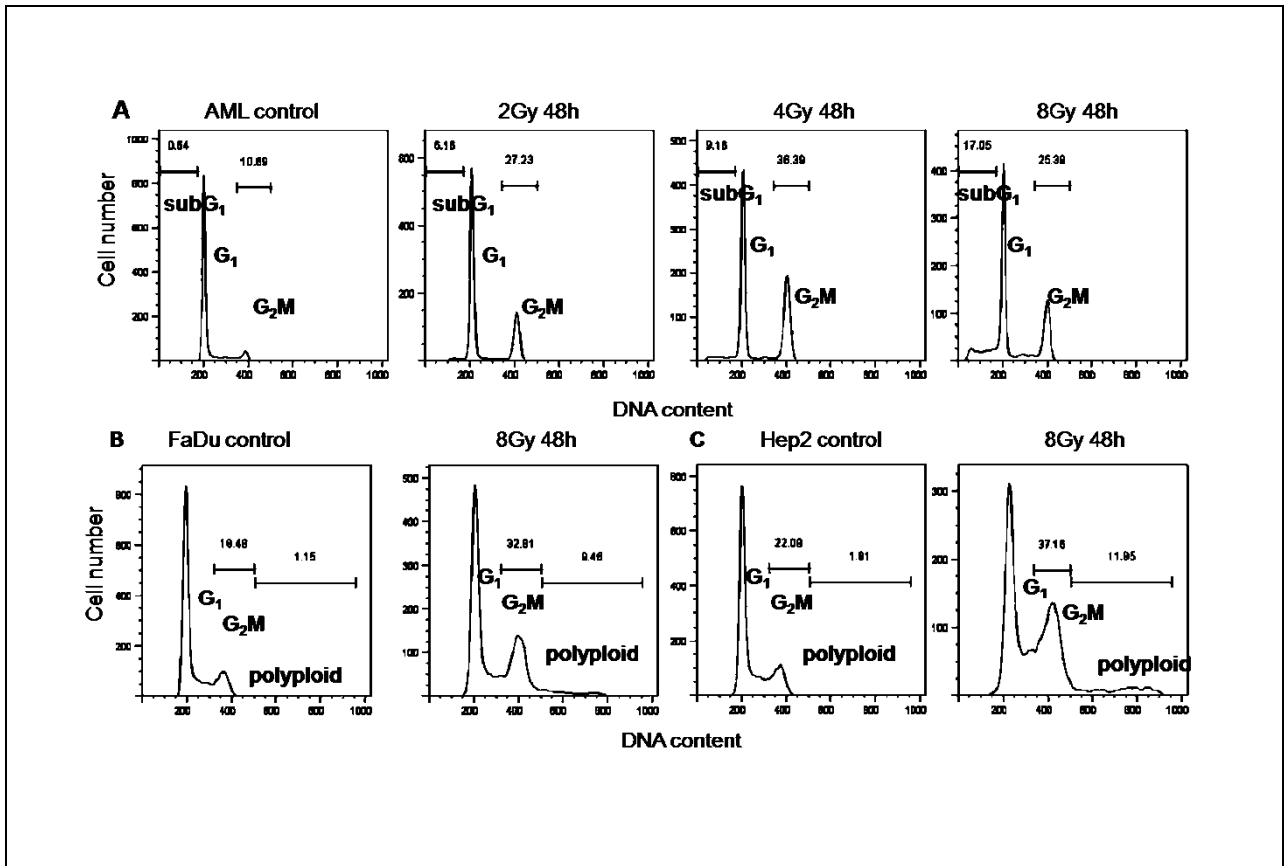
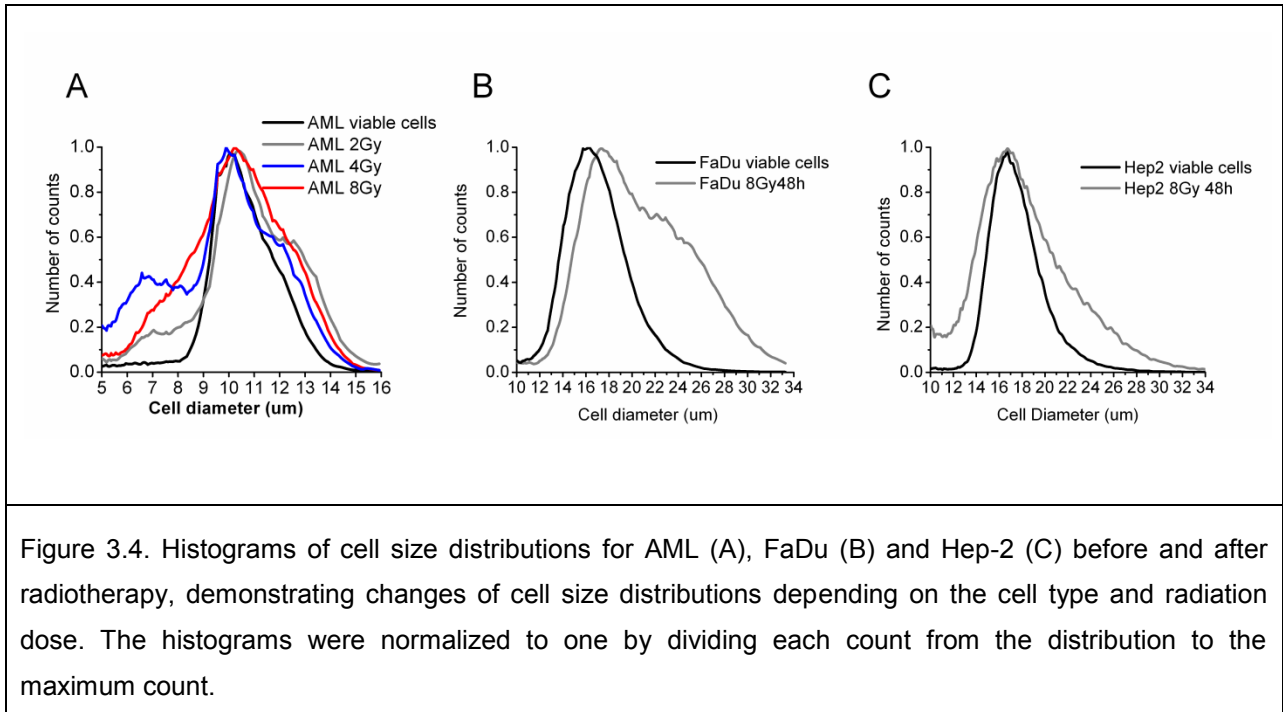


Figure 3.3. Flow-cytometric measurement of cellular DNA content. AML cell samples (A) demonstrating an increase in the apoptotic and mitotic cell fractions illustrated by the sub-G₁ fraction (0.64%-0Gy, 6.16%-2Gy, 9.16%-4Gy, 17.05%-8Gy) and G₂/M fraction (10.69%-0Gy, 27.23%-2Gy, 36.39%-4Gy, 25.39%-8Gy); FaDu (B) and Hep-2 (C) demonstrating an increase in G₂/M fraction (FaDu: 18.48%-0Gy, 32.81%-8Gy; Hep-2: 22.09%-0Gy, 37.16%-8Gy) and polyploid fraction (FaDu: 1.15%-0Gy, 9.46%-8Gy; Hep-2: 1.61%-0Gy, 11.95%-8Gy) after radiotherapy consistent with mitotic arrest/catastrophe.

Scatterer size can be a major determinant of the ultrasound backscattering strength, (indicated in this study by UIB) and of ultrasound backscattering frequency dependence (indicated in this study by SS). Measurements of cell size distributions were carried out to determine how the sequence of cell death affected cell sizes and correlate these changes to the ultrasonic parameters. The measurement of cell sizes demonstrated no significant changes in the average AML cell sizes with the treatment, (Table 1), however, the cell size distributions changed with the exposure to different radiotherapy doses. The cell size distributions revealed an increase in the count of smaller sizes, consistent with apoptotic cells and nuclear fragments,

and an increase in the count of larger sizes, consistent with mitotic arrested cells (Figure 3.4). An increase in the count of larger sizes was measured for FaDu and Hep-2, consistent with cell death by mitotic arrest/catastrophe exhibited by these cell lines (Figure 3.4, B and C).



In this chapter, I also investigated the variance of cell size (the squared standard deviation) because it can considerably influence cell and nuclei spatial organization in a sample (72, 73). The UIB measured from all cell samples correlated well with the variance of cell sizes with a Pearson correlation coefficient of $r=0.80$ and statistical significance of $p< 0.01$ (Figure 3.5). The goodness of fit of the linear regression was $r^2=0.64$, suggesting that the increase in cell size variance may have a contribution to the increase of ultrasound backscatter.

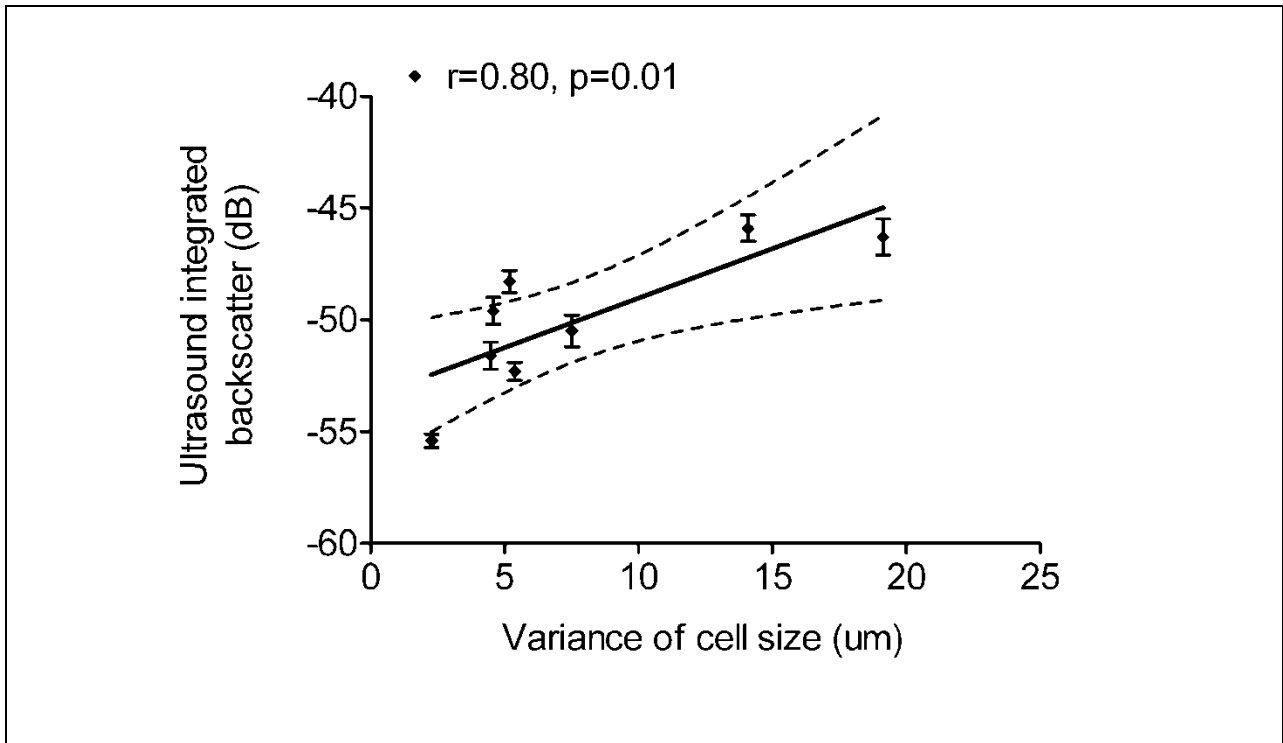


Figure 3.5. Linear correlation between the UIB and the variance of cell sizes measured from all cell samples, viable and exposed to radiotherapy. The curved lines are the 95% confidence bands of the regression line representing the boundaries of all possible straight lines, including the 95% interval of slopes and intercepts.

3.5 Discussion

This chapter demonstrated the use of ultrasonic spectral parameters to detect cell responses to radiotherapy and differentiate cell samples that die predominantly by mitotic arrest/catastrophe from cell samples that die predominately by a mix of apoptosis and mitotic arrest. The changes in ultrasonic parameters were direct consequences of cell structural changes following the sequence of cell death and hence, provides a basis for characterizing tumour responses to radiotherapy in mouse cancer models (29). The SOS and ATS were used to correct the normalized power spectra for frequency dependent attenuation and provided an understanding of how attenuation and speed of sound may change with radiotherapy.

Considering that the cell sample provides a good model of a tissue, this information is essential to *in vivo* applications of this technique (29).

Ultrasonic parameters, including SS and UIB, have been used before to characterize diseased tissue, or tissue and cell samples exposed to different therapeutic agents (27, 28, 40, 52, 55, 62).

The UIB increased in all cell samples exposed to radiotherapy. The UIB depends on size, acoustic properties (density and compressibility) and spatial arrangement of scatterers in a sample. Previous studies demonstrated an increase of ultrasound backscatter *in vitro* and *in vivo* for the cell samples exposed to chemotherapeutic drugs, photodynamic therapy (26, 27) and exposed to ischemic injury (28). The mechanism behind this increase was broadly linked to cell and nuclear morphological changes observed histologically during the sequence of cell death. This study confirms these observations using three cell lines exposed to radiotherapy that underwent different types of cell death. Qualitative analysis of cell microscopy images, the measurements of cellular DNA content and cell size distributions demonstrated that, as expected, the nuclear sizes decreased during cell death by apoptosis and increased during mitotic arrest/catastrophe followed by similar changes in cell sizes (Figures 3.2, 3.3 and 3.4). The changes in cell and nuclei sizes during the sequence of cell death resulted in an increase of the cell size variance by more than two fold as shown in Table 3-1. The increase in the variance of cell sizes may have a contribution to the UIB increase as suggested by the strength of the correlation between the UIB and the variance of cell sizes ($r^2=0.64$). This is further addressed in Chapter 5 of this thesis. Other contributions to the UIB increase can be attributed to morphological changes of cells and nuclei (e.g., sizes and acoustic properties).

The SS can be used to characterize the size of the major scattering structure in tissue as demonstrated previously (43, 44, 52, 63). Previous work of Kolios et al (27) demonstrated that

the SS increased in the cell samples that predominantly presented classic features of apoptosis including cell shrinkage and nuclear condensation and fragmentation. In contrast, in the experiments presented in this chapter, the SS decreased in cell samples that predominantly underwent mitotic arrest/catastrophe and did not change in the cell samples that underwent a mix of apoptosis and mitotic arrest. We suggested that this detection is based on the changes of cell and nuclei sizes during different modalities of cell death. Therefore, the SS can be used as an aid to differentiate the predominant form of cell death in cell samples exposed to different types of therapies.

The head and neck cancer models were chosen in this study because a primary treatment modality for these types of cancers is radiation therapy. Considering future applications of the technique described in this work, these type of tumours could be accessed in humans with endoscopic probes working at 10 to 20 MHz (114). Ultrasound imaging enhanced by ultrasonic spectral parameters could provide the benefit of determining the tumour response early, within days after treatment starts, allowing tumour imaging before and multiple times during the treatment. An early indicator of treatment response would be of great value to tailor treatments to individual patients and particularly promising in multistage interventions or combination treatments.

A penetration depth of 3 to 5 cm allows the technique to be applicable to a variety of tumours types such as skin cancers, certain cancers of the breast and cancers that can be reached with endoscopic probes such as nasopharyngeal and gastro-intestinal cancers. Studies in progress in our laboratory are investigating the potential of detecting similar effects with lower-frequency ultrasound down to 5 MHz that may enlarge the range of applications.

In conclusion, ultrasound imaging (10-30 MHz) and quantitative ultrasonic methods were used to detect responses to radiation treatment *in vitro* and differentiate between cells that die

predominantly by mitotic arrest/catastrophe from cells that die predominately by a mix of apoptosis and mitotic arrest. Experimental evidence supports the basis for ultrasonic detection of radiation therapy effects to be changes in size and potentially size variance of cell and nuclei following apoptosis, mitotic arrest and mitotic catastrophe. The technique may be applied pre-clinically *in vivo* on tumours grown subcutaneously in mice for further ultrasonic characterization of tumour responses to radiotherapy (29). The results indicate that these cell structural changes have a strong influence on backscattered ultrasound and SS, providing a framework for future experiments with the goal of demonstrating the potential of rapidly and non-invasively monitoring and differentiating the effects of radiotherapy and other anticancer treatments using an ultrasound based approach.

3.6 APPENDIX - Assessment of cell morphological changes indicative of responses to ionizing radiation

These cell structural changes: cell shrinking, nuclear condensation and fragmentation, enlarged cells and nuclei are characteristics of apoptosis and mitotic arrest/catastrophe. They represent indicators of radiation responses and hence precursors of cell death in this study. These cell structural changes were qualitatively and quantitatively assessed by cytologic and histologic analysis and measurements of cell sizes and DNA content. Finally cumulative cell death following radiation therapy was assessed using clonogenic assays.

Cytology and histology analysis include hematoxylin and eosin, TUNEL and fluorescent staining. Haematoxylin and eosin is the most widely used stain combination in medical diagnosis. The staining method involves application of the basic dye hematoxylin, which colors basophilic structures with blue-purple hue, and alcohol-based acidic eosin, which colors eosinophilic structures in bright pink. The basophilic structures are usually the structures rich in chromatin, e.g., cell nucleus and structures containing nucleic acid, e.g., the ribosomes ⁵. The eosinophilic structures are generally composed of intracellular and extracellular protein. Most of the cytoplasm is eosinophilic. The structures do not have to be acidic or basic to be called basophilic and eosinophilic. The terminology is based on the affinity to the dyes.

TUNEL (Terminal uridine deoxynucleotidyl transferase dUTP nick end labeling) is a common method to detect cells that undergo apoptosis. It detects DNA fragmentation that results from apoptotic signaling cascades. The assay relies on the presence of nicks (breaks) in the DNA which can be identified by terminal deoxynucleotidyl transferase, an enzyme that will catalyze the addition of dUTPs ⁶ that is secondarily labeled with a marker to the 3' hydroxyl

⁵ The site of protein synthesis, it contains RNA (ribonucleic acid).

⁶ Deoxyuridine-triphosphate is one of the 5 nucleotides from the structure of the nucleic acids.

termini of double and single stranded DNA (1). It may also label cells undergoing necrosis or cells that have suffered severe DNA damage.

The fluorescent probes including Hoechst 33342 to stain cell nuclei and complementary red-fluorescent Alexa Fluor 594 to stain cell membranes were used in this study. The fluorescence probe Hoechst 33342 is DNA selective and emits blue fluorescent light when is excited by ultraviolet light. The complementary fluorescent probe Alexa Fluor 594 binds selectively to some components of the cell membrane (N-acetylglucosamine and N-acetylneuraminic acid), absorbs green light and emits red fluorescent light.

Cell cultures were examined using phase contrast microscopy imaging. The phase contrast microscopy relies on the small differences in the refractive index and thickness between parts of the specimen such as between nucleus and cytoplasm or between the specimen and the surrounding medium. These differences are seen as degree of darkness or brightness in the image of the sample. The advantage of this technique is that cells do not involve any staining and can be monitored at different time intervals as many times as needed alive in the culture flask.

Cell size measurement was performed using a Multisizer 3 Coulter Counter that can provide high throughput analysis of cell number and cell size distributions from cell suspensions. The overall analysis range is from 0.4 to 1200 μm . Cells, once, suspended in a weak electrolyte solution are drawn through a small aperture that separates two electrodes that have an electric current flowing between them and thus, creating a voltage across the aperture. As a cell passes through the aperture, it displaces its own volume of electrolyte, momentarily increasing the impedance of the aperture. This change in impedance produces a pulse that is directly proportional to the volume of the cell that pass through the aperture. Finally, the analysis of these pulses enables a cell size distribution to be computed and displayed.

DNA content measurement provides a mean to quantify the modalities of cell death in a cell sample. Flow cytometry offers the advantage of a rapid analysis of large populations of individual cells with the aim of detecting various parameters of cell death based on the changes in light scattering properties of the dying cell. DNA-analysis can be performed by labeling cellular DNA with fluorescent probes, e.g. propidium iodide. Propidium iodide is a membrane impermeant and generally it is excluded from viable cells. The intensity of the light signal scattered by the labeled cell traversing the laser beam of the flow-cytometer is representative of the DNA content (5). Apoptotic bodies and cell fragments have less DNA than normal cells whereas cell in mitosis, mitotic arrest and mitotic catastrophe have more DNA than normal cells (113, 115).

Clonogenic assay represents experimental methods that assess the probability of cells to survive, divide and generate progeny by forming colonies of a predetermined minimum size when plated in appropriate growth conditions. At present, clonogenic survival remains the gold standard for determining the radiosensitivity of cells *in vitro*.

4 QUANTITATIVE ULTRASOUND CHARACTERIZATION OF RESPONSES TO RADIOTHERAPY IN CANCER MOUSE MODELS⁷

4.1 Abstract

In this chapter, I demonstrate the application of quantitative ultrasound methods to characterize tumour responses to cancer radiotherapy *in vivo*, as early as 24 hours after treatment administration. Currently, no imaging modality is used routinely to assess tumour responses to radiotherapy within hours to days after the delivery of treatment. The work presented in this chapter indicates that the responses to radiotherapy *in vivo*, in mouse cancer models, can be characterized non-invasively using ultrasound spectrum parameters and parametric images.

Three mouse models of head and neck cancer were exposed to radiation doses of 0, 2, 4 and 8 Gy. Data were collected with an ultrasound scanner using frequencies of 10 to 30 MHz. Ultrasound estimates calculated from normalized power spectra and parametric images (spatial maps of local estimates of ultrasound parameters) were used as indicators of response.

Two of the mouse models (FaDu and C666-1) exhibited large hyperechoic regions at 24 hours after radiotherapy. The ultrasound integrated backscatter increased by 6.5 to 8.2 dB ($p < 0.001$) and the spectral slopes increased from 0.77 to 0.90 dB/MHz for the C666-1 tumours and from 0.54 to 0.78 dB/MHz for the FaDu tumours, ($p < 0.05$), in these regions compared with pre-irradiated tumours. The hyperechoic regions in the ultrasound images corresponded in histology to areas of cell death. Parametric images could discern the tumour regions that responded to treatment. The other cancer mouse model (Hep-2) was resistant to radiotherapy.

⁷ The work presented in this Chapter is accepted for publication in Clinical Cancer Research 2009, 15(6).

The results indicate that cell structural changes following radiotherapy have a significant influence on ultrasound spectral parameters. This provides a foundation for future investigations regarding the use of ultrasound in cancer patients to individualize treatments non-invasively based on their responses to specific interventions.

4.2 Introduction

In clinical oncology, tumour responses to treatment are still largely assessed using anatomical imaging measurements of reductions in tumour size. This can take several weeks to occur and with some therapies may not occur at all despite a positive functional response to treatment (8). Computed tomography (CT), positron emission tomography (PET) and combined CT/PET imaging have been used to assess tumour responses to cancer therapies typically 3 to 4 weeks after treatment initiation (10, 108). Dynamic contrast-enhanced magnetic resonance imaging (DCE-MRI) measurements have been demonstrated to correlate with immunohistochemical surrogates of tumour anti-angiogenesis (109, 110) within the same time frame. Diffusion-weighted MRI (DW-MRI) has been used clinically to measure therapy response in different type of cancers such as brain tumours (116), gastro-intestinal cancers (117) and metastatic breast cancer (118). Dynamic contrast-enhanced Doppler ultrasound (DCE-DUS) has predicted early tumour responses in isolated perfusion studies of limb sarcomas (111) within 1 to 7 days after therapy delivery. However, the use of such imaging modalities to monitor tumour responses to cancer therapies can be limited either by their cost (DCE-MRI, DW-MRI, PET, CT, combined PET/CT) or limited applicability (DCE-DUS).

In this chapter, I test the hypothesis that mid to high frequency ultrasound imaging and quantitative ultrasound methods can be used to characterize tumour responses to cancer radiotherapy *in vivo*, as early as 24 hours after treatment administration. The ability to assess early tumour responsiveness to therapy within hours to days after the start of the treatment, could ultimately aid clinicians in making decisions to modify therapy e.g., choosing different radiation regimens, adding a radiosensitizer or using different chemotherapy drugs that potentially could result in more effective treatment leading to improved outcomes and sparing patients from unnecessary side effects.

The aim of cancer therapy is to kill tumours by inducing cell death (1) that can be used as an indicator of tumour response to therapy (8, 31). Currently, standard methods for detecting cell death are invasive requiring tissue biopsy for histological analysis. Previous studies have indicated that mid- to high-frequency ultrasound i.e., 10 to 60 MHz, is sensitive to apoptosis *in vitro* and *in vivo*. Backscatter intensity from apoptotic cells has exhibited an up to sixteen-fold increase in comparison with viable cells (26, 27). In addition, spectral slopes have increased significantly for apoptotic cells in comparison to viable cells (27). Similar changes in ultrasound backscatter have been detected in tissues exposed to lethal ischemic injury (28). For the range of the ultrasound frequencies used in these studies, 10 to 60 MHz, the corresponding wavelengths of 150 to 25 μm , approach the size of cells and nuclei (10-20 μm), and hence, are more sensitive to changes in cellular and nuclear structure than conventional ultrasound (frequencies < 10 MHz).

Characterization of tissue microstructure by examining frequency-dependent backscatter is termed quantitative ultrasound (QUS). QUS estimates describe the statistical properties of tissues structures or cell samples from a well defined ROI. QUS methods have been used to diagnose prostate cancer, ocular tumours, liver and cardiac abnormalities (44, 52, 62, 64), differentiate benign fibroadenomas from mammary carcinomas and sarcomas (66) and have provided good diagnostic accuracy in prostate cancer detection and lesion localization (91). QUS methods, specifically spectral parameters, can sense subtle structural alterations induced by ultrasonically induced hyperthermia in tumour xenografts (119), discern between different types of ocular tumours (16, 45) and classify these depending on their lethality potential (50, 64).

The work presented in this chapter represents the first evidence of the use of ultrasound imaging and spectrum analysis to detect radiotherapy effects *in vivo* in preclinical tumour mouse models. Tumour responses to radiotherapy were characterized by three ultrasound spectral parameters: the ultrasound integrated backscatter (UIB), spectral slope (SS) and spectral

intercept (SI). Although only two of these parameters are independent, it is useful to consider all three, since each of them is related to a different set of tissue scatterer properties. These spectral parameters were employed, firstly, to compute the average ultrasound spectral parameters within a region of interest and, secondly, to generate parametric images. We demonstrate that ultrasound spectral parameters and tumour parametric images can be used to non-invasively detect cell death in tumours, as early as 24 hours after radiotherapy at clinically relevant ultrasound frequencies of 10 to 30 MHz.

4.3 Methods

4.3.1 Animal use

All animal experiments were conducted in accordance with the guidelines of the Animal Care Committee (Sunnybrook Health Sciences Center, Ontario, Canada) and satisfied all the rules for the humane use of laboratory animals. In all experiments, 6 to 8 week-old severe combined immunodeficient (SB-17, SCID) male mice (Charles River Laboratories Inc, Ontario, Canada) were used.

4.3.2 Mouse Tumours

Cell culture. Three mouse models of head and neck cancer, a nasopharyngeal carcinoma (C666-1), a squamous cell carcinoma of the pharynx (FaDu) and an epidermoid carcinoma of the larynx (Hep-2) were used in this study. FaDu and Hep-2 cell lines were obtained from American Type Culture Collection (ATCC, Manassas, Virginia, USA). C666-1 cells (120, 121) were maintained in RPMI 1640 cell culture media (Invitrogen Canada Inc., Burlington, Ontario, Canada) supplemented with 10% fetal bovine serum (FBS) (Cansera International Inc., Etobicoke, Ontario, Canada) and antibiotics (100 mg/L penicillin and 100 mg/L streptomycin) (Bioshop, Burlington, Ontario, Canada). FaDu cells were cultured in Eagle's minimum essential

media (Invitrogen Canada Inc., Burlington, Ontario, Canada) with 2 mM L-glutamine and Earle's balanced salt solution adjusted to contain 1.5 g/L sodium bicarbonate, 1.0 mM sodium pyruvate (Sigma-Aldrich Co, Canada) and 10% FBS. Hep-2 cells were cultured in minimum essential media supplemented with 10% FBS and 0.1% gentamycin (Hoffman-La Roche Ltd, Canada). All cell lines were grown in a humidified atmosphere at 37°C, containing 5% CO₂.

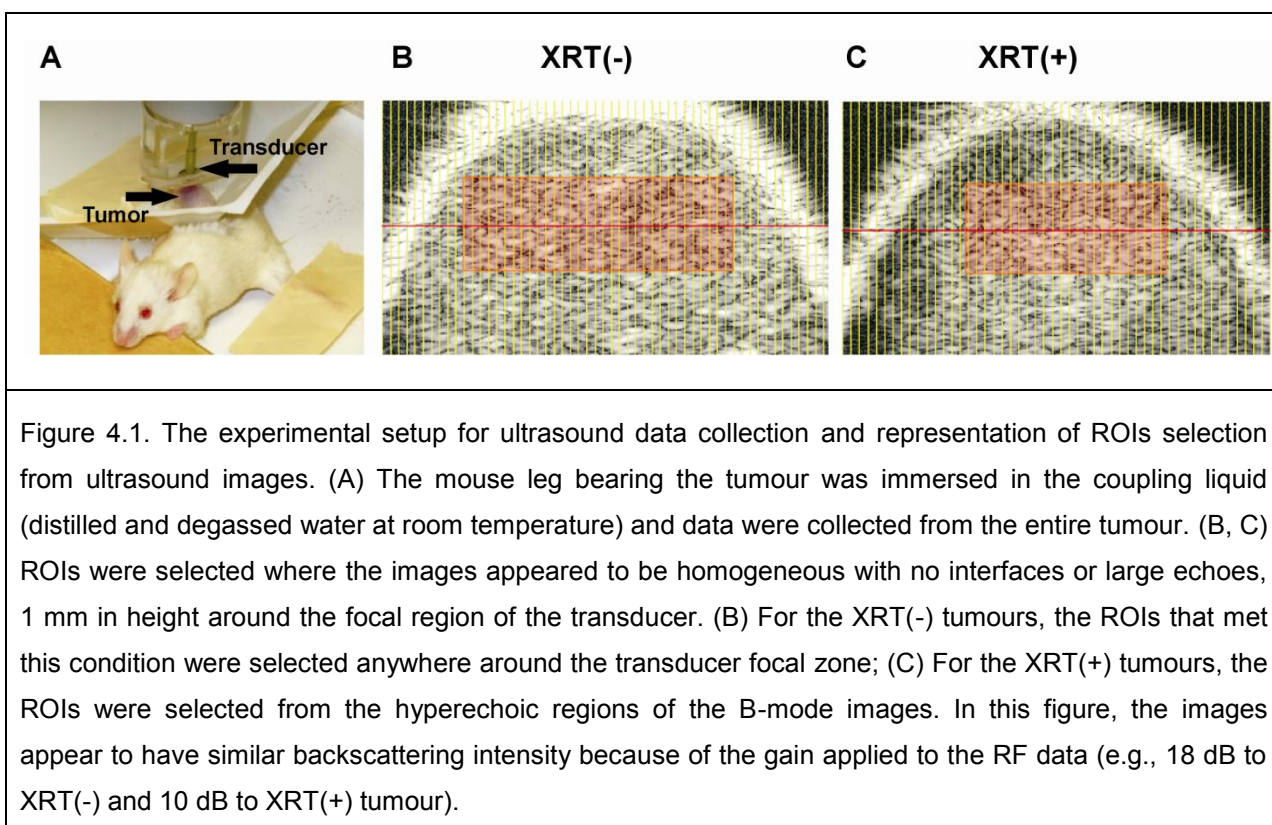
Xenograft tumour models. C666-1 (~10⁶), Hep-2 (~10⁶) and FaDu (~10⁵) cells were injected intradermally into the left hind leg of each mouse. Primary tumours were allowed to develop for approximately 2 to 4 weeks until they reached a diameter of 6 to 10 mm.

Prior to imaging mice were anaesthetized and the tumour and surrounding area were depilated (Nair, Mississauga, Ontario). Anaesthesia consisted of 100 mg/kg Ketamine, 5 mg/kg Xylazine and 1 mg/kg Acepromazine typically in 0.1 ml saline injected intravenously. This sedated mice for approximately 1 hour, sufficient time for the entire imaging and irradiation procedure. A total of 24 animals were used in this work. Six tumours per cell line were irradiated, with two animals at each radiation dose of 2, 4 and 8 Gy. The notations used in this chapter are: XRT(-) for the tumours prior exposure to radiotherapy and XRT(+) for the tumours exposed to radiotherapy. The rest of the animals served either as negative controls (4 animals), or the tumours exceeded the limit accepted for the experiment (10 mm largest dimension). The histology of the negative control tumours was checked against the histology of those regions in XRT(+) tumours that did not respond to therapy. The large tumours exhibited large hyperechogenic patches in ultrasound images at Day₀ and, therefore, were not considered as negative controls. These hyperechogenic patches were thought to represent regions of spontaneous cell death and, in order to check the histology of these patches, the large tumours followed the same protocol as the tumours exposed to radiotherapy (except irradiation).

Administration of ionizing radiation. Tumours were irradiated using a small animal irradiator, (Faxitron Cabinet X-ray System, Faxitron X-ray Corporation, Wheeling, IL, USA) that delivered 160 keV X-rays at a rate of 200cGy/minute.

4.3.3 Ultrasound data acquisition and analysis

A VisualSonics VS40B high-frequency ultrasound device (VisualSonics Inc., Toronto, Ontario, Canada) with a 20-MHz focused transducer (20-mm focal length, 8-mm aperture diameter, -6dB bandwidth of 11-28 MHz) was used to collect ultrasound images and radio-frequency (RF) data from all tumours. The experimental set-up is shown in Figure 4.1A.



Data collection. Ultrasound images were collected from 10 to 20 different scan planes with a distance between planes of 0.5 mm, by scanning the whole tumour sequentially from one side to another in order to sample the entire tumour. RF data were collected from 5 to 10 different scan planes in the middle of the tumour. Each plane contained 40 to 60 8-bit RF lines sampled at 500 MHz. The regions of interest (ROIs) chosen to calculate the average ultrasound parameters were 4 to 6 mm wide and 1 mm in height centered at the transducer focus, as displayed in Figure 4.1(B and C).

Spectrum analysis. RF data from each line segment were multiplied by a Hamming weighting function to suppress spectral lobes and the Fourier transform was computed. The squared magnitudes of the resultant spectra were averaged, divided by the power spectrum computed from a flat quartz in order to remove system and transducer transfer function and calculate the NPS (normalized power spectra). The resulting NPS were integrated over the transducer's -6 dB bandwidth to calculate the averaged UIB (dB). The SS (dB/MHz), the slope calculated from the linear regression analysis of the NPS, and the SI (dB), the extrapolation at zero MHz frequency, were computed. The UIB is similar to the midband fit described by the spectrum analysis framework developed by Lizzi et al (49, 88) and can be related to the effective scatterer size, concentration, and difference in acoustic impedance between the scatterers and surrounding medium. The SS can be related to the effective scatterer size (55) (i.e., an increase in the SS corresponds in theory to a decrease in the average scatterer size) and the SI depends on effective scatterer size, concentration, and relative acoustic impedance. Further details on the theoretical and signal analysis considerations and how spectral parameters are related to tissue microstructure can be found elsewhere (49, 88).

Since attenuation in intervening tissues can affect these parameters, the NPS were compensated for frequency dependent attenuation in skin and tumour tissue. The attenuation coefficient assumed for the skin was 0.2 dB/mm/MHz based on published attenuation

coefficients (122). The thickness of the skin was measured from the ultrasound images, yielding values of 0.30 ± 0.06 mm for (XRT-) and 0.45 ± 0.15 mm for (XRT+) tumours. The attenuation coefficient used for the tumour tissue was 0.06 dB/mm/MHz. This value was computed in the homogeneous regions of the mouse tumours, before and 24 hours after irradiation, by measuring the linear rate of decrease in UIB with increasing depth (44). This attenuation coefficient was similar to the attenuation coefficients measured *in vitro* from corresponding cell samples, viable and after exposure to radiotherapy (39). Signal analysis was performed using custom programs developed in MATLAB (The Mathworks Inc., Natick, MA, USA).

Spectral parameter images. Parametric images were generated and displayed local values of UIB, SS and SI as color coded pixels. The images were formed using a sliding Hamming window of 500 μ m with a 90% overlap to progressively analyze RF data along the individual scan lines. The length of the sliding window was chosen to yield parametric images with good resolution and reasonable stable estimates of spectral parameters based on the theoretical relationship between the size of the sliding window and the statistics of spectral parameters (89, 123). The spectrum analysis described above was performed at each window site to compute the corresponding local parameter values.

Statistics. A t-test was used to compare the spectral parameters computed from all independent RF lines collected from XRT(+) tumours against corresponding values computed from the same tumour before-irradiation using GraphPad Prism (GraphPad Software, San Diego, California, USA). A value of $p < 0.05$ was considered significant.

4.3.4 Histology

Twentyfour hours after irradiation and immediately after final ultrasound imaging, tumours were excised, fixed in 10% neutral-buffered formalin, processed and embedded in paraffin. The tumours were sectioned in the same nominal orientation to best match the ultrasound scanning

planes. Hematoxylin and eosin (H&E) staining was performed for routine histological analysis and TUNEL (terminal uridine deoxynucleotidyl transferase 2'-Deoxyuridine 5'-Triphosphate nick end labeling) staining was used to assess cell death, specifically apoptosis.

4.4 Results

Ultrasound images and spectral characterization results for all type of tumours are given in Figures 4.2-4.4. Representative ultrasound images and corresponding TUNEL staining of C666-1 tumour sections before and 24 hours after irradiation are displayed in Figure 4.2(A and B). After exposure to different radiation doses, the tumours exhibited large hyperechoic patches corresponding to the brown colored regions in the TUNEL staining indicating cell death. In contrast, Hep-2 tumours did not respond to therapy. Moreover, the tumours presented no significant change in echogenic appearance (Figure 4.2C). TUNEL staining presented some isolated clusters of cell death after treatment with 8 Gy radiation dose (Figure 4.2C) and no indication of cell death at 2 and 4 Gy radiation dose.

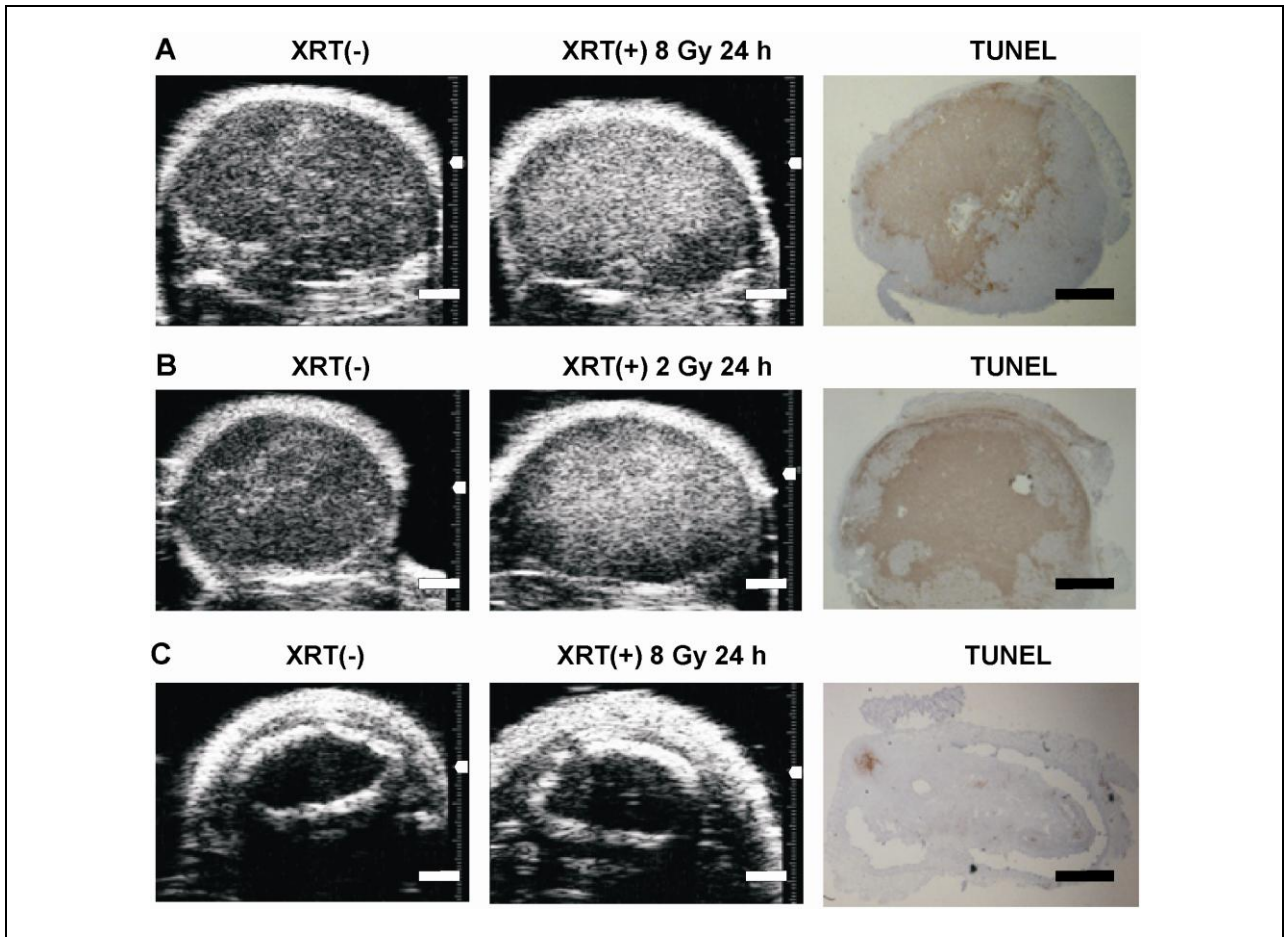


Figure 4.2. Representative ultrasound images of the XRT(-) and XRT(+) tumours and TUNEL staining corresponding to the XRT(+) tumours. (A, B) Ultrasound images of the C666-1 XRT(+) tumours presenting regions with increased echogeneity after radiotherapy, corresponding to the areas of cell death in the TUNEL stained sections. (C) Hep-2 tumour with no appreciable changes in the ultrasound images after exposure to radiotherapy and the corresponding TUNEL staining presenting only sparse brown spots indicating some isolated clusters of cell death. The triangle on the lateral side of each tumour represents the location of the transducer focal point. The scale bars represent 1 mm.

The average UIB measured from C666-1 and FaDu tumours increased by 8.2 ± 0.8 dB and 6.5 ± 1.0 dB ($p < 0.001$), respectively, after exposure to radiotherapy (Figure 4.3A). The average SS increased from 0.77 ± 0.03 dB/MHz to 0.90 ± 0.05 dB/MHz for C666-1 tumours ($p < 0.05$) and from 0.54 ± 0.06 dB/MHz to 0.78 ± 0.05 dB/MHz for FaDu tumours ($p < 0.05$) (Figure 4.3A). A feature analysis plot of the UIB versus SS displayed a separation between the XRT(-) and XRT(+) tumours (Figure 4.3A).

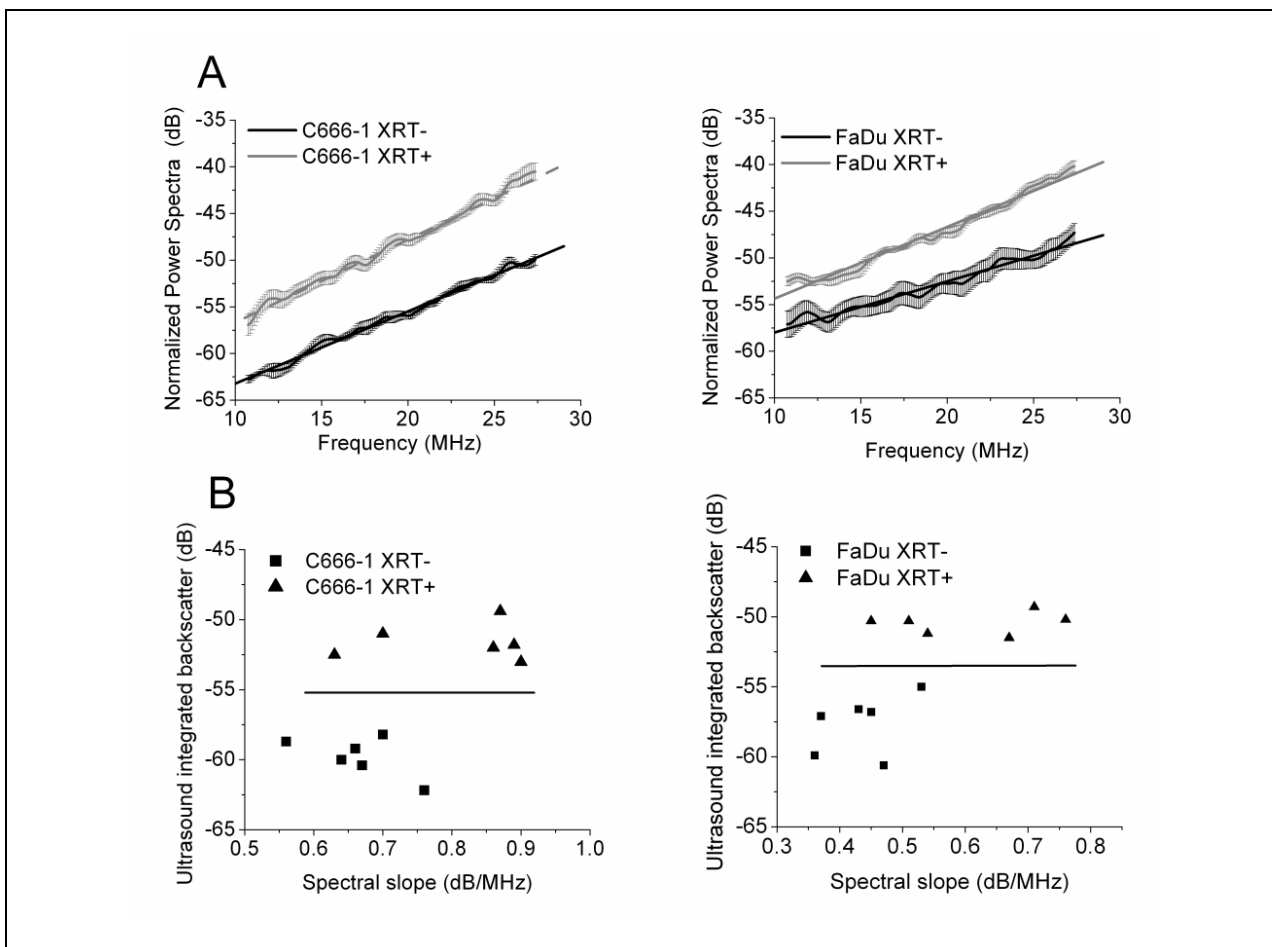
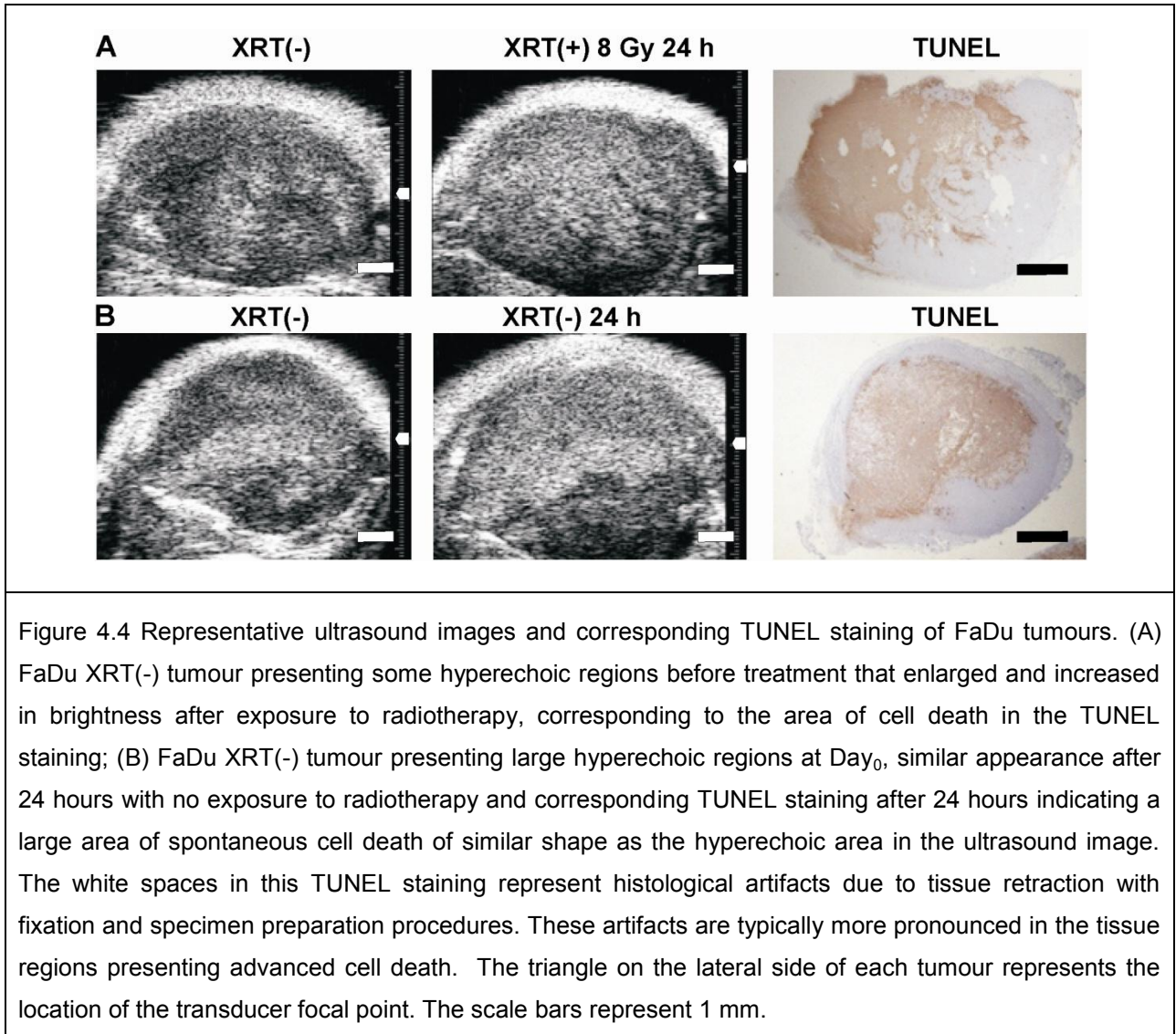


Figure 4.3. Ultrasound spectral parameter characterization of tumour responses to radiotherapy. (A) Averaged normalized power spectra and spectral slopes of C666-1 and FaDu tumours and, (B) corresponding feature analysis plots indicating a separation between the XRT(-) and XRT(+) tumours. Error bars in panel (A) represent the standard error of the averaged spectra for $n=6$ animals per each tumour type.

Some of the FaDu tumours exhibited small hyperechoic patches at Day₀, as presented in Figure 4.4(A). We considered that this complex ultrasound pattern might correspond to small spontaneous necrotic/apoptotic regions inside the tumour prior to radiation exposure. This pattern would mimic well some human tumours and hence, it was considered a valid approach to evaluate those tumours in the analysis. This pattern resulted in larger variability between NPS values calculated from XRT(-) FaDu tumours as indicated by Figure 4.3A. Nevertheless, after

radiotherapy, the size of the patches in these tumours increased, covering larger regions (Figure 4.4A).



The tumours larger than 10 mm were not exposed to radiotherapy (Figure 4.4B). These tumours exhibited large hyperechoic areas in the ultrasound images at Day₀ and were kept in the experiment in order to examine histologically the nature of these hyperechogenic patches. These large, rapidly growing tumours increased in all three dimensions by 0.5 to 2 mm from Day₀ to Day₁, whereas the treated tumours did not present significant changes in size. No

significant changes in the echogeneity of the ultrasound images of these untreated tumours were observed from Day₀ to Day₁. The corresponding TUNEL staining at Day₁ exhibited a large area of cell death (Figure 4.4B). This represents an example of ultrasound imaging detecting another modality of cell death (e.g. spontaneous cell death).

A representative ultrasound image, corresponding TUNEL staining and parametric images computed from the local estimates of spectral parameters are displayed in Figure 4.5. The local estimates of the UIB and SI were greater in the areas corresponding to the hyperechoic patches in the ultrasound images, following closely the areas of cell death from TUNEL staining (Figure 4.5, A-D). The parametric images constructed from the SS estimates resulted in a pattern of features different from the pattern in the corresponding conventional ultrasound images (Figure 4.5, A and E).

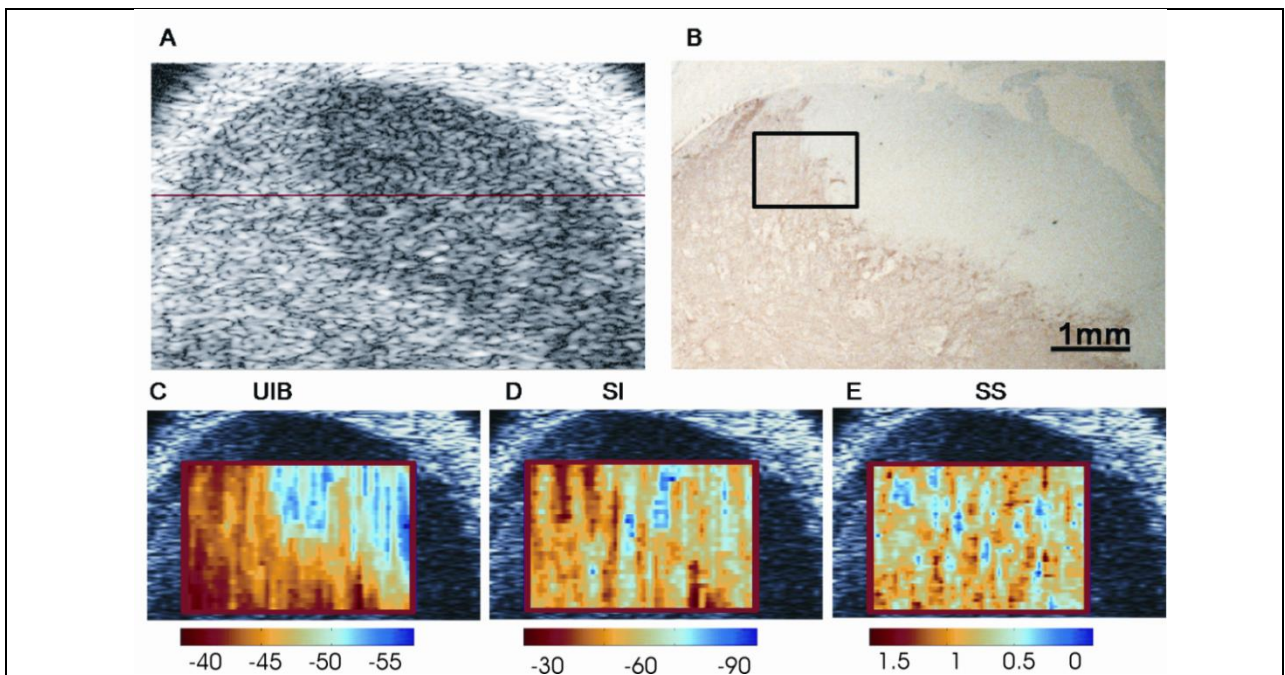


Figure 4.5. Ultrasound image with corresponding histology and parametric images. (A) Ultrasound image, (B) corresponding TUNEL stained image indicating an area of cell death of similar shape as the hyperechoic area in the ultrasound image and parametric images computed from the local estimates of (C) UIB, (D) SI and (E) SS. The colorbars under each parametric image indicate the ranges of the corresponding estimates of the spectral parameters. The boxed region in the TUNEL staining corresponds to the H&E staining from the Figure 4.6 (A).

H&E staining revealed a clear delineation between the areas of cell death, characterized by small condensed and fragmented nuclei, and regions exhibiting the normal phenotype (Figure 4.6, A and B). Overall the H&E staining revealed high tissue heterogeneity, more pronounced in the area of cell death and characterized by disparate nuclear sizes and changes in nuclear density. The area of viable cell phenotype contained some isolated clusters of cell death and exhibited a more homogeneous appearance (Figure 4.6, B and C). The H&E staining of the un-irradiated tumour presented no significant evidence of cell death (Figure 4.6C).

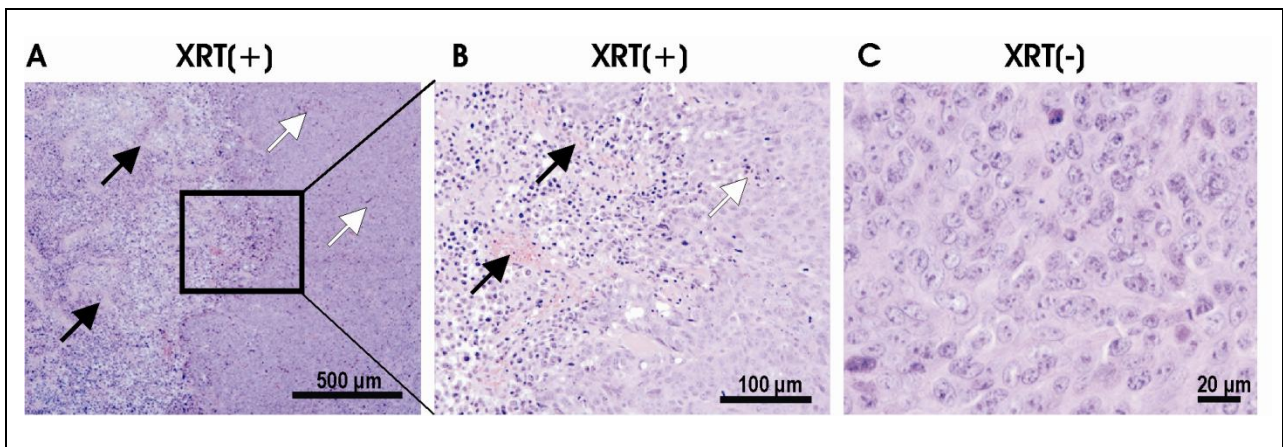


Figure 4.6. Hematoxylin and eosin images of the XRT(+) tumour of Figure 4.5 at two different magnifications (A) corresponding to the selection from Figure 4.5B and (B) corresponding to the selection from Figure 4.6A and H&E image (high magnification) of an XRT(-) tumour. The left side of the XRT(+) tumour images demonstrate the characteristics of cell death. The small white spaces in these regions represent histological artifacts due to tissue retraction with fixation procedure. These artifacts are typically more pronounced in the tissue regions presenting advanced cell death. The black arrows point to possible blood vessels. The right side of each image presents the appearance of viable tissue with white arrows pointing to isolated clusters of cell death. The H&E image of the XRT(-) tumour exhibit a relative homogeneous appearance with no significant evidence of cell death.

4.5 Discussion

The work presented in this chapter demonstrates for the first time that radiotherapy effects can be characterized by quantitative ultrasound methods in preclinical mouse cancer models, as early as 24 hours after treatment administration. The changes in ultrasound images and spectral parameters were interpreted as direct consequences of cell death following radiotherapy. This method was able to detect the regions of cell death in a tumour and thus it has the potential to detect tumours or tumour regions that respond to treatment from those that do not.

The histology from this study revealed that the most prominent structural changes following radiotherapy were related to cell nucleus as indicated by the TUNEL staining (Figures 4.2, 4.4 and 4.5) and H&E staining (Figure 4.6). These histological observations and evidence from previous work (26, 27, 39, 40, 42), suggested that the main changes in the ultrasound backscatter following radiotherapy were related to changes in nuclear size and properties.

Changes in UIB can be related to a combination of scatterer properties: size, spatial organization, concentration and relative acoustic impedance (72, 88). The regions exhibiting cell death in histology were characterized by an overall decrease in nuclear sizes, a consequence of nuclear condensation and fragmentation during the sequence of apoptotic cell death (Figure 4.6). According to models of ultrasound scattering (16) a decrease in scatterer size alone, maintaining other factors constant, would result in a decrease in UIB. This was not observed in this work. Therefore, the changes in the UIB most likely resulted from other changes in nuclear properties, (i.e., changes in acoustic impedances, concentration and spatial arrangement). For example, the darker staining of condensed nuclei suggested changes in the nuclear acoustic impedances, i.e., higher values of 2.00 MRayl for condensed chromatin versus 1.58-1.55 MRayl for cytoplasm have been reported recently (124). The increase in the randomization of nuclei during the sequence of cell death may also contribute to the increase in the UIB as previously indicated by a model of ultrasound scattering (72) and recently, suggested by experimental

observations (39). Since SI is related to the size, concentration and relative acoustic impedance of scatterers (49, 88), the increase in the SI, similarly to the increase in the UIB, might result from changes in nuclear properties and increase in the number of nuclear fragments following apoptotic cell death.

The local estimates of the SS presented large variations in the regions that responded to therapy, as well as, in the regions corresponding to the normal tumour phenotype (Figure 4.5E). These variations may result from a combination of factors including the inherent biological heterogeneity of tissue structure, heterogeneity of the tumour response to treatment and the model applied to calculate the SS estimates. The SS is mainly related to the scatterer size, therefore, the inherent biological variance of nuclear sizes and other structures affect the SS estimates. Furthermore, Chapter 3 has indicated that there is an increase in the variance of nuclear and cellular sizes following cell death. This could further increase the local variability of the SS estimates, predominantly in the regions of the tumour that presented the characteristics of cell death. The SS estimates are frequency dependent, therefore, they are sensitive to the length of the sliding window and to the frequency dependent attenuation. Larger sliding windows would yield better estimates and lower variance but with a compromise of a coarser resolution in the parametric images. Therefore, based on these considerations, the SS worked well in characterizing the responses to radiotherapy in large ROIs but yielded unstable local estimates when used with small ROIs. A variable attenuation along the ultrasound propagation path may also contribute to the larger variability of the local estimates of the SS. Further investigation towards the formulation of new models addressing the anisotropy of tissue constituents and their properties may help in obtaining better estimates for tissue characterization (124).

The head and neck cancer mouse models were chosen in this study because a primary treatment modality for these types of cancers is radiation therapy. Considering future applications of the technique described in this work, these types of tumours could be accessed

in humans with endoscopic probes working at 10 to 20 MHz (114). Ultrasound imaging enhanced by ultrasonic spectral parameters could provide a benefit of determining the tumour response early, within days after treatment starts. This would allow tumour imaging before and multiple times during treatment without the need of injecting specialized contrast agents as other techniques (e.g., PET, DCE-MRI, DCE-DUS). An early indicator of treatment response would be of great value to tailor treatments to individual patients and particularly promising in multistage interventions or combination treatments.

Guiding tissue biopsies may be another area of interest. Although tissue biopsies provide important information regarding molecular pathology and thus tumour response, the sampled tissue may not adequately represent the heterogeneity of the tumours and furthermore cannot be sampled longitudinally. Superimposed parameter estimates on gray scale ultrasound images enable non-invasive assessment of cell death in tumour or tumour regions and can be used to determine the location for tissue biopsies.

A penetration depth of 2 to 5 cm at the frequencies of 10 to 30 MHz allows the technique to be applicable to a variety of tumour types such as skin cancers, certain cancers of the breast and cancers that can be reached with endoscopic probes such as nasopharyngeal and gastrointestinal cancers. Ongoing studies in our laboratory are investigating the potential of detecting similar effects with lower-frequency ultrasound of down to 5 MHz (125) that may expand the range of applications (125).

In this work the Hep-2 tumours did not respond to radiotherapy and presented no evidence of cell death in the TUNEL staining. Thus, the Hep-2 tumours served for two purposes in this study: to act as a tumour model that did not respond to radiotherapy and also to provide an example of a tumour model with a complex tissue structure not amenable to this type of ultrasound analysis due to high specular reflections at the interfaces with some tissue

structures. These structures were highly attenuating and obscured the ultrasound scattering in the encapsulated tumour (Figure 4.2C).

In conclusion, spectral parameters and tumour parametric images constructed from spectral parameters were used to detect responses to radiation treatment *in vivo* for two cancer mouse models, at 24 hours after treatment administration and at the clinically relevant frequencies of 10 to 30 MHz. The ultrasound imaging within this frequency range was also able to detect spontaneous cell death in large XRT(-) tumours. This validates our findings, indicating that this ultrasound detection method is sensitive to the structural changes following cell death.

The third tumour model did not respond to therapy as verified by TUNEL staining and provided an example of complex tumour pattern for which this type of analysis may not be applicable without additional assessment tools. The experimental evidence presented in this chapter supports the basis for the application of mid-to high frequency ultrasound imaging and quantitative ultrasound methods to characterize early tumour responses to cancer radiotherapy. The results indicate that these cell structural changes have a profound influence on spectral parameters providing a framework for future experiments and/or clinical studies aimed at demonstrating the potential of rapidly and non-invasively monitoring the effects of radiotherapy and other anticancer treatments using an ultrasound based approach.

5 AN INCREASE IN CELL SIZE VARIANCE APPEARS TO EXPLAIN PART OF THE ULTRASOUND BACKSCATTER INCREASE MEASURED DURING CELL DEATH ⁹

5.1 Abstract

The work presented in this chapter presents a mechanism to explain the ultrasound backscatter increase measured from cell samples undergoing different forms of cell death. Based on the findings presented in this chapter and on the previous work of Hunt et al (72, 73) a simplified model of ultrasound scattering is proposed and compared to the experimental results.

Ultrasound integrated backscatter (UIB) was measured for four tumour cell lines (AML, FaDu, Hep-2 and C666-1), viable and undergoing cell death, after exposure to radiotherapy and/or chemotherapy. Ultrasound radiofrequency data were collected with an ultrasound scanner using frequencies from 10 to 30 MHz. An increase of 3.8-7.5 dB ($p < 0.001$) in UIB was measured from three of these cell lines following different forms of cell death.

No increase in UIB was measured from C666-1 cell samples undergoing cell death. An increase in the variance of cellular size following cell death was found for all cell lines. The correlation between UIB and the variance of cell sizes was $r = 0.79$ ($p = 0.006$). While many factors contribute to the increases in UIB, the purpose of this chapter was to explore the possibility that part of these increases is a consequence of the increase in the variance of cellular size. The UIB values were compared with simulations of ultrasound scattering from distributions of scatterers with different degrees of randomization. The changes measured in UIB with increasing in the variance of cellular size were in general agreement with the

⁹ The work presented in this chapter has been under review with Ultrasound in Medicine and Biology.

simulations of ultrasound scattering with increasing randomization. The simulation predicted no increase in ultrasound scattering for cellular arrangements with large randomization values (> 1.5), consistent with the result observed for the C666-1 cell line.

It was concluded that the increase in UIB could be in part explained by the increase in the randomization of the spatial distribution of nuclei following cell death.

5.2 Introduction

Radio-frequency (RF) ultrasound data have been used extensively in medical ultrasound to analyze noninvasively the structural properties of biological media (26-28, 43, 55, 60, 62, 67, 126). One approach is to use the frequency dependence of the RF backscatter spectrum. The RF spectrum can be related to the structure of a medium if this can be modeled as a random distribution of scattering particles (16) and the characteristics of instrumentation are known. Under these conditions, it is well known that the frequency dependence of the RF spectrum is mainly dependent on the size of the dominant scattering structure in the medium. The magnitude of the RF spectrum depends on the size, number density (number of scatterers per unit volume) and the relative acoustic impedance (fractional variation in acoustic impedance between the scattering particles and the surrounding medium) of the scattering particles. Accurate estimation of these properties requires that tissue structures responsible for scattering to be known. Although these scattering structures are not well understood, several research groups have been able to characterize various tissues using simple correlation models (43, 53, 55, 67, 80, 87, 92, 126).

Our group has been using ultrasound imaging and RF spectrum analysis to detect cell death in cell samples and tumours exposed to cancer therapies. These studies demonstrated that ultrasound backscatter increased in cell samples undergoing various forms of cell death: apoptosis (26, 27, 36), oncosis (28) and mitotic arrest/catastrophe (39).

The ability of ultrasound spectrum analysis to assess changes in physical characteristics of tissue scatterers makes the technique promising as a method to monitor cell death in preclinical and clinical settings. As this work progressed, the need for a better understanding of changes in the cellular structure that cause the increase in ultrasound scattering has become more pressing. In order to optimize the signal analysis algorithms and provide better quantitative

estimates of cell death, quantitative ultrasound studies have been conducted on simple biological media, i.e., cell samples emulating the cell packing in tissue and cell suspensions (27, 38, 39, 127, 128). Experimental evidence from these studies has suggested that ultrasound backscatter characteristics are dominated by nuclear size and acoustic properties at the frequencies of 10 to 60 MHz (39, 40, 69). Some of the increase in UIB can be attributed to nuclei condensation and fragmentation following cell death by apoptosis. For example, an acoustic impedance of 2.00 MRayl for condensed chromatin versus 1.58-1.55 MRayl for cytoplasm has been recently reported (124). Changes in cellular acoustic properties have also been reported in live cells undergoing apoptosis (41, 129). While cell apoptosis may result in stiffer nuclei or more nuclear fragments, there are other forms of cell death (e.g., oncosis, mitotic arrest/catastrophe) that are characterized by other types of cell structural changes. These structural changes usually result in an increase of cellular and nuclear size, as opposed to nuclear condensation and fragmentation (characteristics of apoptotic cell death), but result in similar increases in ultrasound scattering (28, 37, 39) as with apoptotic cell death.

The work presented in this chapter explores a mechanism, common to the diverse forms of cell death exhibited by the cell samples exposed to radiotherapy and chemotherapy, capable to explain the changes in UIB. The experimental data were collected from cell samples of four different tumour cell lines, viable and undergoing different forms of cell death after treatment. The increase in ultrasound backscatter in these samples, can be due to changes in scatterer properties (size and acoustic impedance) or could be linked to different degrees of randomness in the spatial distribution of scatterers, as predicted by the model proposed by Hunt et al (72, 73). Randomness refers to the degree of spatial organization of scatterers in a given ensemble of scatterers. For instance, a distribution of random scatterers lacks any predictable order whereas a less-random distribution (pseudo-random) has some degree of predictable order in scatterer spatial organization.

The work presented in this chapter brings new insights into the mechanisms responsible for increases in ultrasound backscattering following cell death. Specifically, the study explores the possibility that part of the increases in ultrasound backscatter measured from cell samples undergoing cell death results from the increase of the randomness in the spatial distribution of nuclei. Considering that the nuclei occupy fixed positions in the center of the cell, the changes in nuclear positions in a tightly packed collection of cells of similar size can be regarded as a direct consequence of the changes in cellular sizes (following cell death in this example). The experimental evidence presented in this chapter illustrates that all cell samples undergoing cell death exhibited an increase in the variance of cellular size. This increase in the variance of cellular size was linked to an increase in the randomness of the spatial distribution of the cell nuclei and consequently to increases in ultrasound backscatter.

5.3 Background

Historically, the established scattering models in biological tissue assume that the scatterers are randomly distributed to allow closed form solutions for various equations used to calculate ultrasound backscatter. Using this approach, the backscatter characteristics can then be related to the underlying tissue structure. Under this assumption, regardless of what theoretical approach is taken, e.g., discrete or continuum scattering model, it is recognized that ultrasound scattering in tissue is primarily affected by the size and acoustic properties of tissue scattering structures (16) and their relationship to ultrasound wavelength. However, the assumption of random scatterer distribution may not hold in cell samples or tumours with tightly packed cells. For example, in modeling the scattering from red blood cells, it is assumed that red blood cells are randomly distributed only for very low hematocrit concentrations ($< 2\%$), because under these conditions the position of any red blood cell can be considered

independent of the location of any other cell (15). For a collection of randomly distributed red blood cells, ultrasound backscatter increases with the variance of red blood cell volumes (15).

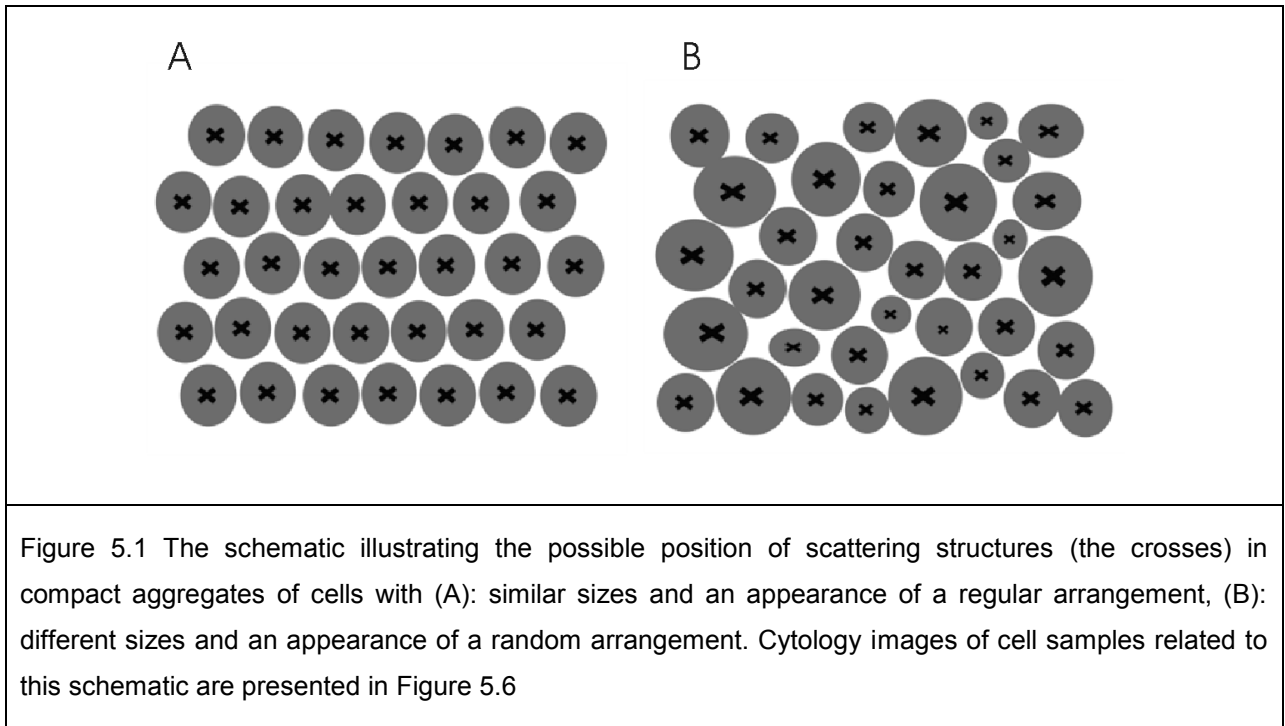
The effect of increase in scatterer volume fraction (i.e., increase in hematocrit) has been well documented for non-biological scatterers and red blood cells (94). Similar effects have been reproduced using suspensions of nucleated cells by Baddour et al (130). For high hematocrit or cell volume fraction the positions of any pair of cells are correlated and the spatial organization of cells can no longer be considered random (16). Some investigators (96, 97) have used a packing factor to account for the decrease in ultrasound backscatter due to the destructive interferences resulting from the increase in the correlation between particles in dense media. The packing factor defines a measure for the orderliness in the spatial arrangement of red blood cells and can be used to predict the ultrasound backscatter at high hematocrit (94, 131).

In a tightly packed collection of cells and, typically, in biological tissues, cells are packed even closer than red blood cells, because they are in physical contact with each other. For example, for cell sizes between 10 and 20 μm there are 150 to 1200 cells per resolution volume defined by the axial ($\sim 80 \mu\text{m}$) and lateral resolution (~ 250) of the high frequency ultrasound beam used typically in our experiments. If cells are tightly packed and have similar sizes, it is reasonable to believe that they are not in a random, but more organized arrangement and their positions are correlated. Figure 5.1 presents a schematic of tightly packed arrangement of cells with similar sizes and more irregular sizes. Since the cells are not identical spheres, they will not have a perfect regular arrangement but there is nonetheless some degree of order in tightly packed collection of cells with similar sizes.

The model used in this study of (72, 73) predicts that could be a large reduction of the backscatter signal if the scattering sources are regularly spaced. This model has been able to

provide an explanation for the “black” regions in ultrasound images of highly concentrated red blood cells, as being caused by a more regular separation of cells in those regions (15, 16, 93). The same model has predicted large changes in backscatter for scatterers with the same number density but different degrees of randomization. Furthermore, this model is in good agreement with the large increases in ultrasound backscatter with cell death and the appearance of disorganization in the arrangement of cells and nuclei undergoing apoptosis compared with viable samples that exhibit a more uniform appearance (26, 27, 70, 73). Overall, the model indicates that ultrasound backscatter signals are very sensitive to the effects of randomization in scatterer positions.

This chapter investigates the increase in ultrasound backscatter in cell samples undergoing cell death. Subtle changes in cell organization can take place following cell death, as the variance of cellular size increases. As the variance of cellular size increases, the position of nuclei departs from a regular to a more random distribution as represented in Figure 5.1. It is hypothesized that the increase in ultrasound backscatter with cell death is partially caused by an increase in the randomization of cell nuclei, e.g., from fairly regular spaced nuclei in viable cells to more random spaced nuclei following cell death. Assuming that the nucleus occupies the center of the cell, the nuclei position in a tightly packed collection of cells is primarily determined by cells position and packing of cells, and can be predicted as a function of cellular diameter and variance of cellular size.



5.4 Methods

5.4.1 Cell preparation

Acute myeloid leukemia cells (OCI-AML-5) (112) were grown from frozen stock samples as described elsewhere (40). FaDu and Hep-2 cell lines were obtained from American Type Culture Collection (ATCC, Manassas, Virginia, USA). C666-1 cells (120, 121) were maintained in RPMI 1640 cell culture media (Invitrogen Canada Inc., Burlington, Ontario, Canada) supplemented with 10% fetal bovine serum (FBS) (Cansera International Inc., Etobicoke, Ontario, Canada) and antibiotics (100 mg/L penicillin and 100 mg/L streptomycin) (Bioshop, Burlington, Ontario, Canada). FaDu cells were cultured in Eagle's minimum essential media (Invitrogen Canada Inc., Burlington, Ontario, Canada) with 2 mM L-glutamine and Earle's balanced salt solution adjusted to contain 1.5 g/L sodium bicarbonate, 1.0 mM sodium pyruvate (Sigma-Aldrich Co, Canada) and 10% FBS. Hep-2 cells were cultured in minimum essential

media supplemented with 10% FBS and 0.1% gentamycin (Hoffman-La Roche Ltd, Canada). All cell lines were grown in a humidified atmosphere at 37°C, containing 5% CO₂.

All cell lines were exposed to radiotherapy. The AML cell line was also exposed to chemotherapy. It was expected that radiotherapy and chemotherapy would result in different forms of cell death in these cell lines (26, 27, 39). Cell samples were irradiated using a small animal and cell irradiator Faxitron Cabinet X-ray System (Faxitron X-ray Corporation, Wheeling, IL, USA) that delivered 160 keV X-rays at a rate of 200 cGy/minute. The AML cell line was separately treated with the chemotherapeutic drug cis-platinum (cisplatin) at 10 µg/mL that induces apoptosis in this cell line (26, 27, 132). Cells were treated with the drug for 0, 12, 24, 48 and 72 h.

The cell cultures were examined daily under light microscopy in order to confirm cell death. Structural changes that are characteristic of apoptotic or mitotic response (i.e., increase in cell and nuclei size, membrane ruffling, cytoplasm vacuolization, nuclear fragmentation and condensation and formation of apoptotic and mitotic bodies) were used as an indication of cell death (115). These structural changes were observed in AML cell culture for all time points of treatment with cisplatin and at all applied radiotherapy doses. For the head and neck cancer cell lines most of these changes were observed with the 8 Gy radiation dose at 48 h after exposure to radiotherapy.

Before ultrasound data acquisition, cells were trypsinized (Hep-2, FaDu and C666-1) and washed in PBS (phosphate-buffer-saline). AML cells grew in suspension and they did not need to be trypsinized. After washing in PBS, cells were centrifuged at 1900 g to form compact aggregates of cells, referred in this study as cell samples. These cell samples likely emulate the spatial distribution and packing of cells in tumours as indicated in Chapter 6. Treated and viable samples were prepared by centrifugation of cells in two separate wells of a custom-built sample

holder (Figure 5.2, A). The cell samples were independently prepared in triplicate from different sets of cells. A representative ultrasound image of a compact aggregate of cells (cell sample) in the sample holder is presented in Figure 5.2, B.

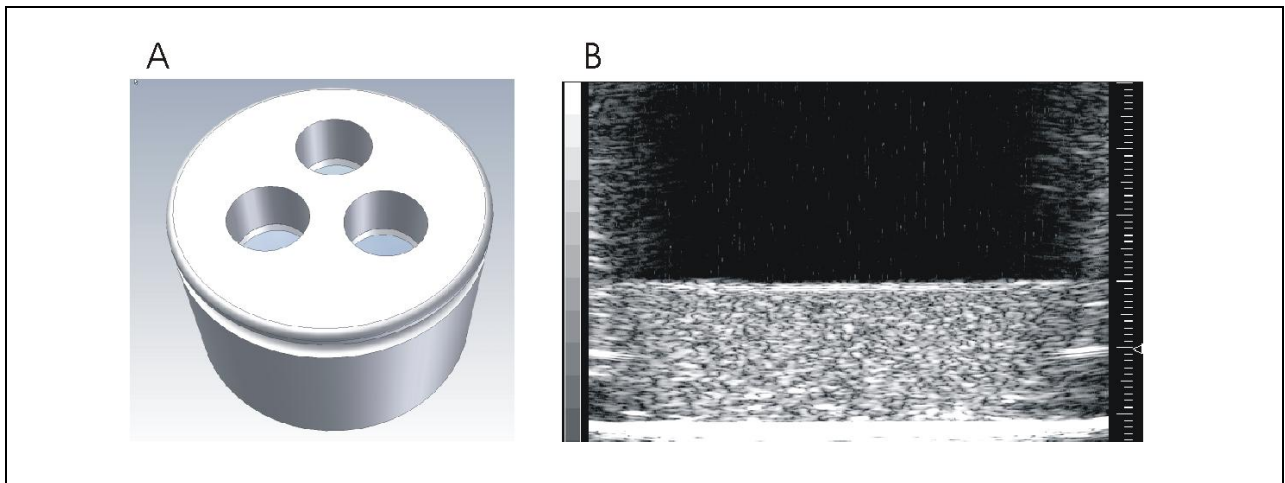


Figure 5.2 Images of the sample holder and a cell sample. (A) Image of the sample holder. The sample holder was made of stainless steel and had two parts: a flat bottom very fine polished to have an ultrasound signal reflection comparable to the transmitted signal and a stainless steel disk with 3 cylindrical holes cut through it, 8 mmx7 mm (diameter x height). The flat bottom was attached with screws to the stainless steel disk and bottom of the wells were cushioned with Teflon rings. Teflon rings ensured that the content of the wells is not spilled between compartments during the sample centrifugation. Two samples can be prepared once by centrifugation in the two wells. The other well serves as a calibration reference. (B) Ultrasound image of a compact aggregate of cells in the sample holder. The height of the cell sample is ~ 2 mm, the smallest division on the scale on the lateral side of cell samples is 0.1 mm. The small triangle on the right side of each cell sample represents the location of the transducer focal point. The hyperechoic lines across the bottom, right and left side of the ultrasound image are the bottom and the walls, respectively, of the sample holder.

5.4.2 Ultrasound data acquisition and analysis

A VS40B high-frequency ultrasound device (VisualSonics Inc., Toronto, Ontario) was used to image cell samples. A focused transducer with a nominal center frequency of 20 MHz

(20-mm focal length, 10-mm aperture diameter, -6dB bandwidth of 11-28 MHz) was used to collect ultrasound data. Data were collected within the transducer depth of field (3.12 mm calculated at the transducer nominal frequency), from five different planes containing 40-60 8-bit RF lines sampled at 500 MHz. The regions of interest (ROIs) chosen to calculate the backscattered power spectra contained 15 to 25 independent scan lines each, at a distance of 250 μm (the transducer beamwidth at the nominal center frequency) and were 1 mm deep, centered around the transducer focus.

Ultrasound scan lines from each bracketed line segment were multiplied by a Hamming weighting function to suppress spectral lobes and the Fourier transform was computed. The squared magnitudes of the resultant spectra from all ROIs were averaged and divided by the power spectrum computed from a flat quartz calibration target in order to calculate the normalized power spectra. This procedure removed system and transducer transfer functions to provide a common reference for data collected with various transducers and systems (89). The normalized power spectra measured from each sample were compensated for frequency-dependent attenuation losses according to (40) using the attenuation coefficients reported in Table 3-1 for AML, FaDu and Hep-2 cell samples, viable and treated with radiotherapy. The rest of the attenuation coefficients for AML and C666-1 cell samples, viable and exposed to chemotherapy and radiotherapy, respectively, are presented in Table 5-1. These attenuation coefficients were calculated as a function of frequency using a broadband technique (74). To calculate the UIB, the resulting normalized power spectra were integrated over the transducer -6dB bandwidth.

Cell type	ATS +/- SE (dB/mm/MHz)
C666-1 control	0.065+/-0.011
C666-1 8 Gy	0.070+/-0.014
AML 12 h	0.058+/-0.012
AML 24 h	0.062+/-0.010
AML 48 h	0.070+/-0.009
AML 72 h	0.130+/-0.015

Table 5-1. Attenuation coefficients slope for AML and C666-1 cell samples, viable and treated with chemotherapy and radiotherapy, respectively. SE represents the standard errors. These values were used to correct ultrasound backscatter for attenuation. Three cell samples were considered for each experimental condition.

5.4.3 Cytology analysis, measurements of cellular and nuclear size

After the acquisition of ultrasound data, the cell samples were fixed in 10% buffered formalin (Fisher Scientific, Neapan, ON, Canada) for a minimum of 2 days. The fixed cell samples were carefully removed from the sample holder and embedded in agar gel, to preserve the shape and integrity of the sample. The agar embedded cell samples were subsequently sectioned and placed in a cassette for paraffin embedding, so that the microtome sections were taken from the same plane as the ultrasound data. The sections were stained with hematoxylin

and eosin (H&E) and fluorescent probes using Hoechst 33342 (that stains cell nuclei) and complementary Alexa Fluor 594 (that stains cell membranes).

Cell and cellular fragment sizes for each experimental condition were measured with a Multisizer3 Coulter Counter (Beckman Coulter, Mississauga, Ontario, Canada) using a 100 μm aperture that allowed precise and reliable measurements of particle size. This method allowed precise measurements of 5000 to 10000 cells per treatment condition within the range of 5-60 μm . Similar measurements of the size of the nuclei are difficult to carry as they would require complex procedures of nuclei isolation that may modify their properties (i.e., may result in additional fragmentation or swelling). The average nuclear size was estimated from the Hoechst 33342 fluorescent staining of cell nuclei by measuring about 50 nuclei per treatment condition. For nuclei with irregular size the diameter was calculated as the average between the minimum and maximum dimension.

Flow cytometric analysis using propidium iodine (Invitrogen Canada Inc., Burlington, Ontario, Canada) was performed to measure cell DNA content (113). Cells were harvested, washed twice in fluorescent activated cell sorting (FACS) buffer (PBS/0.5% bovine serum albumin), resuspended in 1 mL of FACS buffer and fixed for 1 h on ice in 3 mL of ice-cold 70% ethanol. Cells were washed once, before resuspending them in 500 μL of FACS buffer supplemented with 40 $\mu\text{g/mL}$ RNase A (Sigma-Aldrich Co, Canada) and 50 $\mu\text{g/mL}$ propidium iodine and then cells were incubated at room temperature for 30 min in the dark before being analyzed in a FACS Caliber (BD Biosciences, Mississauga, Ontario, Canada) using FL-2A and FL-2W channels. The results are presented as the percentage number of cells found in different phases of the cell cycle. This classification is dependent on DNA content and helps to identify the forms of cell death following each of the applied therapies. The sub- G_1 fractions were identified as apoptotic cells because the nucleus becomes fragmented during apoptosis. The sub- G_1 peak can represent, in addition to apoptotic cells, mechanically damaged cells and cell

fragments in advanced stages of cell death (5, 115). The G_1 peak represents phenotypic normal cells. The G_2/M peak is identified as cells in mitosis and mitotic arrest, whereas the peak with higher than double DNA content (higher than the G_2/M fraction) was identified as cells in mitotic catastrophe and polyploid cells. Cells typically die by mitotic arrest/catastrophe after they undergo up to four unsuccessful mitotic cycles as described by Tannock et al (1) and they are characterized by enlarged cells and nuclei.

5.4.4 Simulation

Simulations of ultrasound backscatter signals from regular to more random distributed scatterers were used to investigate the dependency of ultrasound backscatter signals on the scatterer organization using the method of Hunt et al (72, 73). The model simulated the backscatter signals from cell samples, assuming that the signals are generated by scattering from nuclei. The simulation considered the nuclei as point scatterers situated in the center of the cell and assumed similar scattering strength from each nucleus during each treatment condition. The scattering from nuclei was assumed to be weak (no multiple scattering) and the attenuation within the simulated material was neglected. In the more periodic case, the separation between nuclei was similar to the cell diameter. In the pseudo-random case, the separation between nuclei was generated as a random variation within a specified range.

The scatterer positions were simulated using the equation:

$$S_{i+1} = S_i + D(1.0 - R/2 + (gen \times R)) \quad 5.1$$

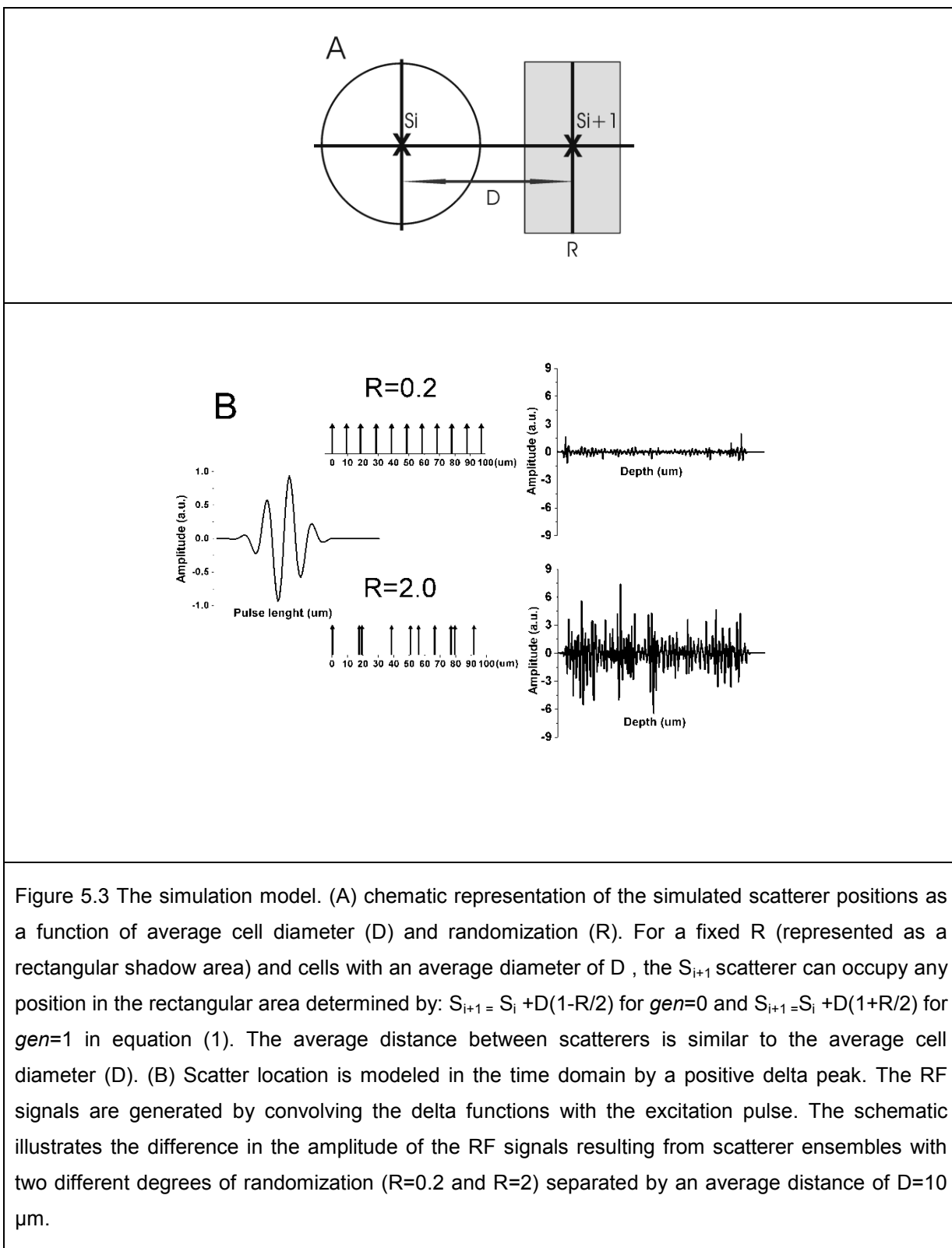
, where S_{i+1} is the position of the consecutive scatterer, D is the average cell diameter, R is randomization, gen is a random number within the interval (0.0, 1.0). Figure 5.3(A) illustrates the calculation of scatterer position as a function of the average cell diameter and randomization. For a fixed R , the S_{i+1} scatterer could occupy any position in the shadowed rectangular area Figure 5.3A, where $gen = 0$ is the left extreme and $gen = 1$ is the right extreme.

Figure 5.3(B) presents the simulation of RF signals for two scatterer distributions: a more periodic case ($R=0.2$) and a more random case ($R=2$).

The experimental randomization in the cell samples was linked to the variance of cellular sizes and was expressed as:

$$R_{\text{exp}} = \text{variance}(\mathbf{Cell\ Size}) / \text{Mean}(\mathbf{Cell\ Size}) \quad 5.2$$

where the maximum R_{exp} measured from the cell samples corresponds to the largest R value considered in the simulation. Finally, the increase in UIB simulated at different values of R from the numerical simulations was compared to the increase in UIB measured experimentally from cell samples.



5.5 Results

The UIB increased for three of the cell lines (AML, FaDu and Hep-2) exposed to cancer treatment by 3.8 to 7.5 dB ($p < 0.001$) (Table 5-2).

Cell type	UIB (dB) +/- SE	Cell size (μm) +/-variance	Nuclei size (μm) +/- variance	sub-G1 (%) (apoptotic)	G2M/polyploid (%) (mitotic arrest/catastro phe)
AML viable	-55.4 +/-0.3	10.3 +/-2.3	8.5 +/-1.4	0.6	10.7/0
AML 2 Gy	-51.6 +/-0.6	10.4 +/-4.5	8.5 +/-1.9	6.2	27.2/0
AML 4 Gy	-48.3 +/-0.5	9.2 +/-5.2	7.8 +/-2.6	9.2	36.4/0
AML 8 GY	-49.6 +/-0.6	9.9 +/-4.6	7.6 +/-3.0	17.1	25.4/0
AML viable	-54.6 +/-0.7	10.6 +/-2.3	8.6 +/-1.0	0.28	14.1/0
AML 12 h	-54.8 +/-1.1	10.6 +/-2.6	8.5 +/-1.4	6.9	12.5/0
AML 24 h	-50.1 +/-1.0	9.6 +/-3.6	7.6 +/-2.8	30.8	10.9/0
AML 48 h	-47.1 +/-0.8	9.6 +/-3.5	7.1 +/-3.2	42.4	8.2/0
AML 72 h	-50.1 +/-1.2	10.1 +/-2.0	6.5 +/-3.3	55.4	7.0/0
FaDu viable	-50.5 +/-0.7	16.6 +/- 7.5	11.7 +/-2.2	0	18.5/1.2
FaDu 8 Gy	-46.3 +/-0.8	19.9 +/-19.1	14.3 +/-3.9	0	32.8/9.5

Cell type	UIB (dB) +/- SE	Cell size (μm) +/-variance	Nuclei size (μm) +/- variance	sub-G1 (%) (apoptotic)	G2M/polyploid (%) (mitotic arrest/catastro phe)
Hep2 viable	-52.3 +/-0.4	17.4 +/- 5.4	12.6 +/-2.5	0	22.1/1.6
Hep2 8 Gy	-45.9+/-0.6	18.0 +/- 14.1	13.7 +/-3.7	0	37.2/12.0
C666-1 viable	-45.7+/-1.2	13.0+/- 26.0	10.4 +/-3.3	0	29.3/3.8
C666-1 8 Gy	-45.9+/-0.6	14.7+/- 33.3	11.1 +/-4.5	0	44.7/5.7

Table 5-2. The UIB, average cellular and nuclear diameter and relevant DNA fractions measured for all cell samples. SE represents the standard errors. Three cell samples were considered for each experimental condition.

No increase in the UIB was measured from C666-1 cell samples exposed to radiotherapy (Table 5-2). The UIB measured from the AML cell samples exposed to chemotherapy and radiotherapy increased depending on the duration of the exposure to the drug and the radiation doses (Figure 5.4, A).

To confirm and quantify different forms of cell death in these cell lines, measurements of DNA content were carried out, in addition to histology. The percentage of cells identified as sub-G₁, G₂/M and polyploid for all cell samples are presented in Table 5-2. Representative sections of H&E staining and corresponding measurements of DNA content are presented in Figure 5.4 (B and C) and 5 (A and B). Examination of the H&E staining indicated that AML cell samples exposed to chemotherapy exhibited predominantly features

associated with apoptotic cell death, specifically nuclear condensation and fragmentation. Corresponding analysis of DNA content indicated increases in the apoptotic fractions (sub- G_1) of up to 70 and 90 fold at 48 h and 72 h, respectively in Figure 5.4 (C) and Table 5-2. No significant increase in mitotic fractions (G_2/M) were measured at any of these time points (Figure 5.4 C and Table 5-2). The AML cells treated with radiotherapy revealed a mix of cell death, apoptosis and mitotic catastrophe (Table 5-2). These observations were in good agreement with the measurement of DNA content that revealed 15 and 28 fold increase in the apoptotic fractions and up to three and two fold increase in the mitotic fractions for the AML cell treated with 4 Gy and 8 Gy radiation dose, respectively (Table 5-2).

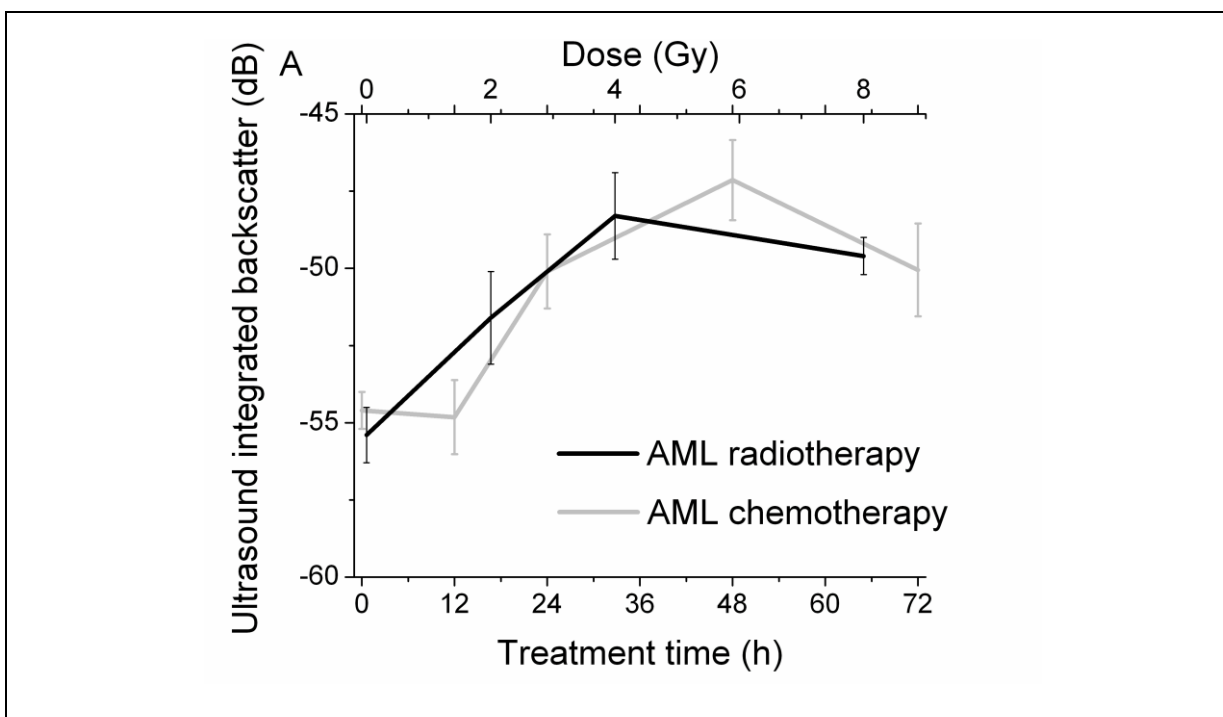
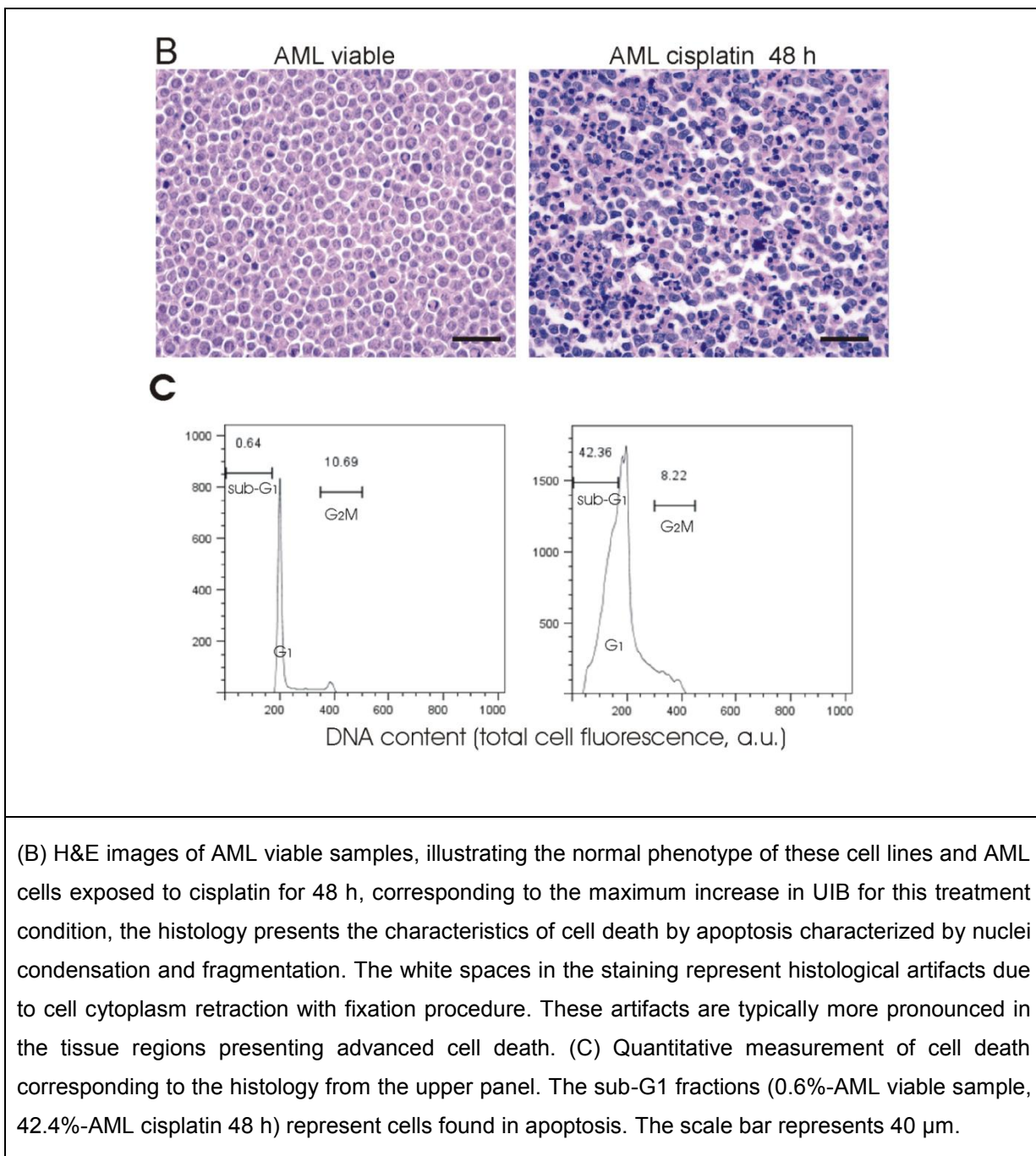


Figure 5.4. The UIB of AML cell samples exposed to cisplatin and radiotherapy. The ultrasound data were collected at 48 h after the cell samples were exposed to radiotherapy. (A) The UIB increased for AML cell lines exposed to chemotherapy by 4.5 to 7.5 dB ($p < 0.001$) with a maximum increase after 48h exposure to the drug. The UIB increased for AML cell sample exposed to radiotherapy by 3.8 to 7.1 ($p < 0.001$) with a maximum increase at 4 Gy radiation dose.



The head and neck cancer cell lines died predominantly by mitotic arrest/catastrophe, since no sub-G₁ fractions were detectable (Table 5-2 and Figure 5.5, A and B). There were approximately two-fold increases in the mitotic cell fractions and two to eight-fold increases in the polyploid cell fractions (Table 5-2 and Figure 5.5A) in these cell lines. Therefore, the cytology and the measurements of DNA content indicated that these

cell samples responded to treatment by different forms of cell death. Although, each of these forms of cell death exhibited distinct structural changes (e.g., nuclear condensation and fragmentation in apoptosis versus increase in nuclear and cellular size in mitotic arrest/catastrophe) an increase in ultrasound backscatter was measured from all cell samples (except C666-1) after treatment.

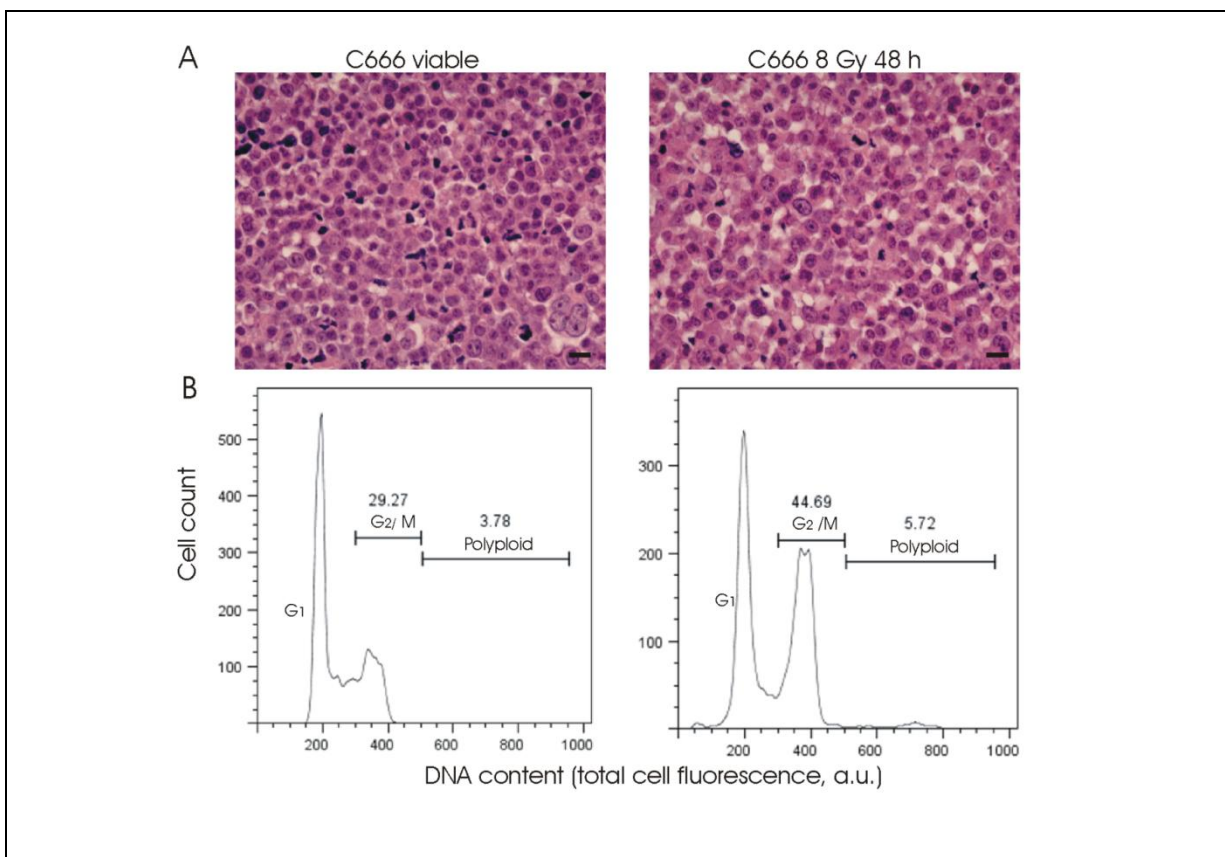


Figure 5.5. Representative H&E staining and corresponding measurement of DNA content for C666-1 cell samples. (A) C666-1 viable samples, illustrating the normal phenotype of these cell lines and C666-1 samples exposed to 8 Gy radiotherapy with a general appearance of enlarged cells. The white spaces in the staining represent histological artifacts due to cell cytoplasm retraction with fixation procedure. These artifacts are typically more pronounced in the tissue regions presenting advanced cell death. (B) Quantitative measurement of cell death corresponding to the histology from the upper panel. The G2/M fractions (29.3% C666-1 viable sample, 45.5% C666-1 8 Gy) represent the cells found in mitotic arrest. Polyploid fractions (3.8%-C666-1 viable sample 5.7% - C666-1 8 Gy) represent the cells found in mitotic catastrophe. The scale bar represents 20 μm .

Scatterer size is a major determinant of the ultrasound backscattering strength with increases in scatterer size resulting in increases in UIB. To determine how the sequence of cell death affected cellular sizes, precise measurements of cell size distributions were conducted using a Multisizer 3 Coulter Counter. The values of the average and variance of cellular size for each of the cell lines, viable and exposed to radiotherapy and chemotherapy, are presented in Table 5-2. The average nuclear size for each cell line was estimated from the fluorescent staining of cells and nuclei staining (Figure 5.6) and is presented in Table 5-2. The average nuclear size measured from AML cell lines exposed to either treatment, chemotherapy or radiotherapy, appeared to decrease. The head and neck cell lines revealed some increase in the average cellular and nuclear size consistent with the predominant modality of cell death mitotic arrest/catastrophe exhibited by these cell lines after radiotherapy (Table 5-2). No significant correlation was calculated between UIB and average cellular size ($r=0.41$, $p=0.12$) and UIB and average nuclear sizes ($r=0.46$, $p=0.08$).

As a result of treatment, the cell and nucleus underwent a series of structural changes resulting in an increase in the variance of cellular size, regardless of the cell line and the modality of cell death (Table 5-2). Figure 5.6 illustrates representative staining of cell nuclei and membranes indicating the changes in nuclear and cellular sizes and their arrangement following cell death for one of the cell lines, the FaDu cell line.

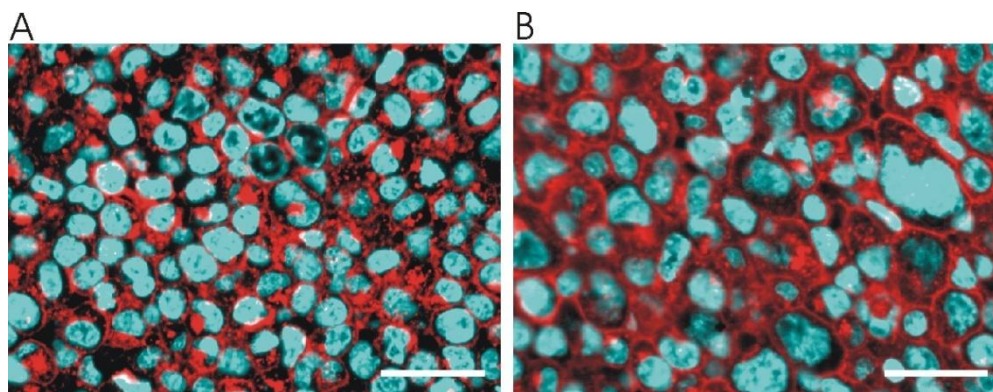


Figure 5.6 Representative staining of FaDu cell samples(A) viable and (B) exposed to 8 Gy radiotherapy illustrating changes in cellular and nuclear sizes and the changes in nuclei arrangement with cell death. The blue Hoechst 33342 stains cell nuclei and complementary red-fluorescent Alexa Fluor 594 stains cell membranes. In the viable cell sample, the nuclei tend to have a more regular distribution, whereas the nuclei in the treated cell sample tend to have a more random distribution. The scale bar represents 40 μm .

Cell size distributions of AML cell samples and C666-1 cell samples before and after exposure to the therapy are presented in Figure 5.7. Following cell death, there was an increase in the number of either smaller particles (consistent with apoptosis) or larger particles (consistent with mitotic arrest/catastrophe), or both smaller and larger particles (consistent with the mix of mitotic arrest and apoptosis). A significant correlation was calculated between the UIB and the variance of cell sizes ($r=0.73$, $p=0.002$) for the values presented in Table 5-2.

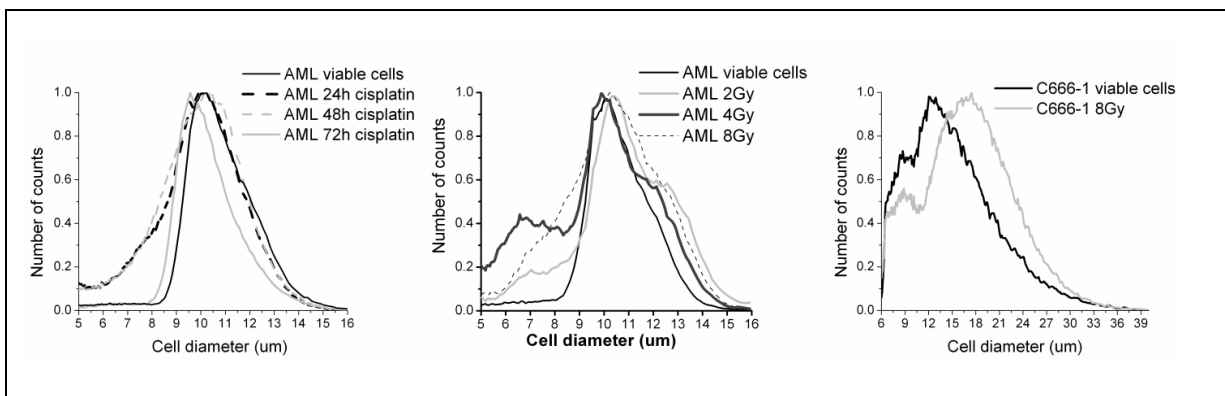


Figure 5.7 Histograms of cell size distributions.(A): AML cells treated with cisplatin for different periods of time, (B): AML cells treated with different doses of radiotherapy and counted at 48 h after exposure, (C): C666-1 cells treated with radiotherapy. The histograms are normalized to one by dividing each count from the distribution to the maximum count.

To examine how the variance of cellular size can influence the UIB, simulations of ultrasound scattering from scatterer distributions with different degree of randomization were conducted. These were compared with the experimental data as presented in Figure 5.8. The changes measured in the UIB with increasing variance of cell sizes were in general agreement with the simulations of ultrasound scattering with increasing randomization. Furthermore, these predicted no increase in ultrasound scattering for randomizations higher than a certain threshold consistent with the high UIB values calculated from C666 cell line before and after treatment.

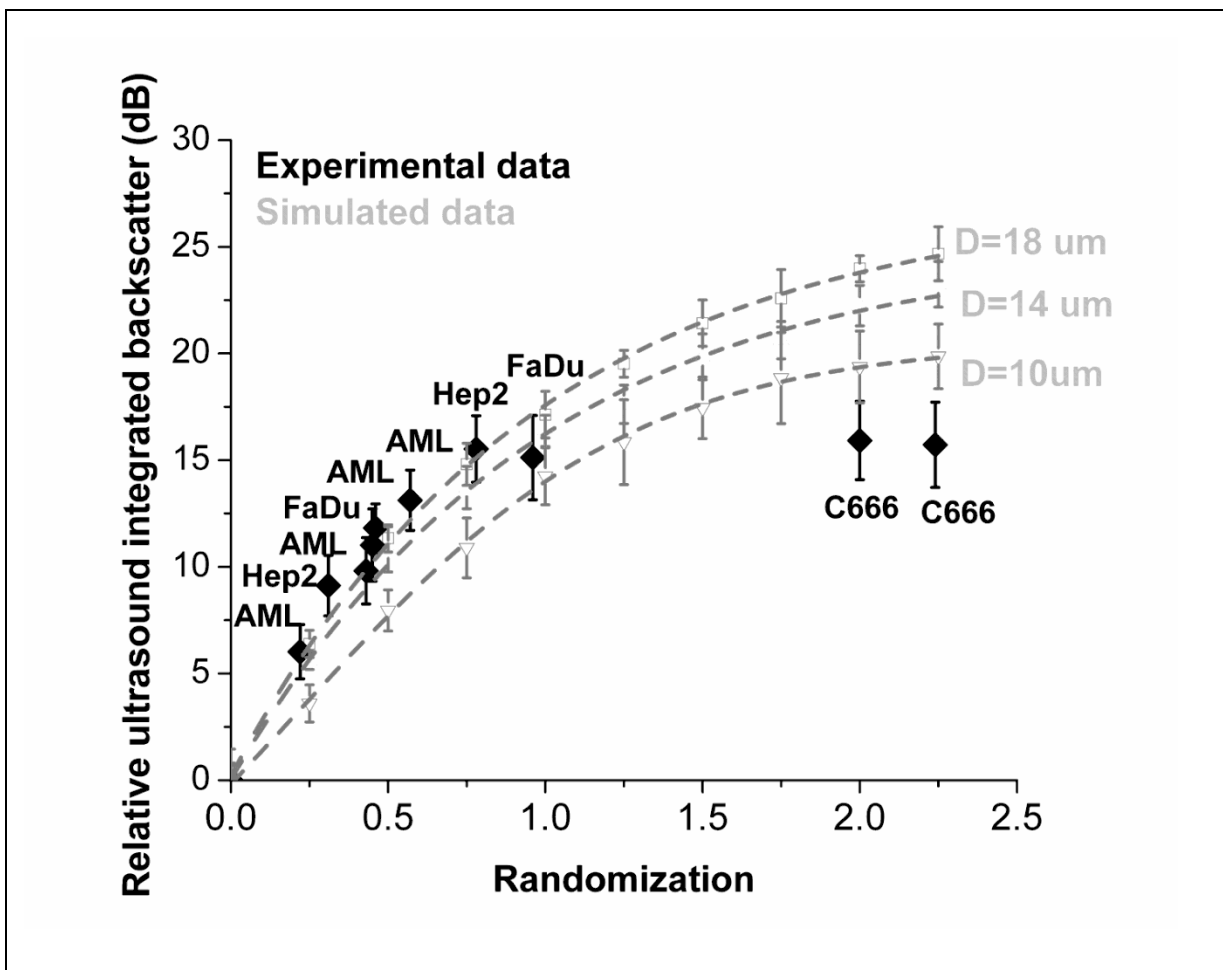


Figure 5.8. Increase in integrated backscatter versus randomization, experimental data and numerical simulation. The simulations were generated for scatterer separations close to the average cellular diameter of the cell lines used in these experiments. The error bars represent standard deviations for ten RF lines (in simulated data) and three independent cell samples (in experimental data).

5.6 Discussion

The goal of this chapter was to explore a mechanism that explains the increases in ultrasound backscatter measured from cell samples undergoing different forms of cell death. These forms of cell death were characterized by disparate cellular and nuclear structural changes but presented similar increases in UIB. Specifically, this study investigated the contribution of an increase of the randomization in nuclei position to the increase of ultrasound backscatter measured from cell samples exposed to anticancer therapies. The study assumed that the cell nucleus is the primary scatterer and the nucleus has a fixed position inside the cell, typically in the middle of the cell. Under these conditions, in a tightly packed collection of cells, the randomness in the position of nuclei depends on the variance of cellular size. Simulated data were generated to model the changes in ultrasound scattering with increasing in the randomness of nuclei position. These results were compared with the UIB increase and variance of cellular size measured experimentally.

The changes in UIB are related to a combination of intrinsic scatterer properties e.g., size, number density and relative acoustic impedance (16, 88). The changes in UIB are also sensitive to scatterer spatial organization, as indicated by the model proposed by Hunt et al (72) and the models of ultrasound scattering in blood (15, 93, 131, 133, 134). Changes in each of these properties happen simultaneously during cell death (i.e. nuclear condensation and fragmentation, increase in the variance of cellular size), resulting in complex histological features from which it is difficult to identify the relative contribution of each type of change to ultrasound scattering. However, each of these changes is likely to have a contribution to the overall ultrasound scattering strength. For example, the increase in the nuclear size in FaDu and Hep-2 cell lines may explain the UIB increase measured from these cell samples after exposure to radiotherapy (Table 5-2). However, the increase in nuclear size alone cannot explain the increases in the UIB measured in the AML cell line exposed to chemotherapy

and radiotherapy. This cell line exhibited either no change or a slight decrease in the average nuclear size for different treatment conditions (Table 5-2). Furthermore, no significant correlation between the UIB increase and the average nuclear size was found for the values presented in Table 5-2. The correlation between the average cellular size and the increases in the UIB was also tested, since some studies (67, 87) suggested that cell is the dominant scatterer within the frequency range of 10 to 25 MHz. No significant correlation between the UIB increase and the average cellular size was found for the values presented in Table 5-2. The AML cells exposed to cisplatin presented significant nuclear condensation with increases in apoptotic fractions of up to 70 and 90 fold at 48 h and 72 h, respectively (Figure 5.4, B and C and Table 5-2). Previous studies have reported changes in the acoustic properties of condensed chromatin following cell death (26, 27, 42, 129). Therefore, it is possible that changes in density and compressibility to explain some of the increases in the UIB measured in AML cell samples undergoing predominantly apoptosis. However, the same magnitude of the UIB increase was measured from the AML cells exposed to 4 Gy radiotherapy that corresponded to a much smaller increase in the apoptotic fraction of 15-fold (Table 5-2). Furthermore, similar increases in UIB were measured in Hep-2 and FaDu cell lines with no evidence of nuclear condensation and apoptotic fractions (Figure 5, A and B and Table 5-2). Therefore, neither of these changes in nuclear size or acoustic impedance was able to explain, alone, the increases in UIB measured from these cell samples (AML, FaDu and Hep-2) after exposure to anticancer therapies. Nevertheless, each of these changes may contribute variably to the increase in UIB depending on the specific modality of cell death. For example, a major contribution to the increase in UIB of AML cells treated with cisplatin appeared to come from changes in the acoustic properties of the condensed nuclei, since the AML cells treated with cisplatin for 72 h, exhibited a 4.6 dB increase in UIB with neither increase in nuclear size or variance of cellular size (Table 5-2).

More evidence that an increase in the variance of cellular size contributes to the increases in UIB came from the fact that an increase in the variance of the cellular sizes was measured in all cell samples, regardless of the modality of cell death. It also correlated well with the increases in UIB ($r = 0.73$, $p = 0.002$). Furthermore, the simulations presented in this study, predicted no significant increase in ultrasound scattering for randomizations values higher than 1.5 (Figure 5.8). This was consistent with the very large variance of cellular size, high UIB values for the C666-1 viable cell samples and no increase in UIB measured from C666-1 cell samples exposed to radiotherapy (Table 5-2). Interestingly, this cell line responded to radiotherapy similarly to the other two head and neck cancer cell lines with increases in mitotic and polyploidy cell fractions (Table 5-2 and Figure 5, A and B). Further evidence of the contribution of variance of cellular size to ultrasound scattering came from the comparison of nuclear sizes and UIB values measured from the head and neck cancer cell lines. The average nuclear size for the C666-1 cell lines was smaller than the average nuclear size for FaDu and Hep2 cell lines, (Table 5-2). If the randomization did not play a part and assuming that nuclear acoustic properties did not present large variations between different cell lines, higher UIB values would be expected from FaDu and Hep2 cell lines with larger nuclei. This is different than the result observed in this study.

The curves that connect the UIB values from the simulations in Figure 5.8 were drawn only for guidance (using a second order polynomial) with no intention of suggesting a specific relationship between UIB and randomization. In their previous publication, Hunt et al (72) reported a linear relationship between the square root of the UIB and randomization. This relationship was valid for randomization values of up to 1.5 with no increase in UIB for randomization higher than 1.5, similar to the results from this study. Suggesting a specific relationship between the relative UIB and randomization is beyond the purpose of this work. We believe that further studies, in which the variance of cellular size can be more carefully

controlled within a large range of values, are more appropriate for this purpose. For example, a tighter control of the variance of cellular size can be achieved by mixing two cell lines of distinct nuclear sizes in different proportions (135).

The fact that ultrasound scattering strength is sensitive to the spatial distribution of nuclei may have a significant impact on ultrasound tissue characterization. Previous studies have indicated the capability of ultrasound backscatter to discern between viable and treated tissue (26, 29, 42) and viable and damaged tissue (28). In these studies, the regions that presented higher tissue echogeneity in ultrasound images corresponded to regions of higher tissue heterogeneity. For example, larger heterogeneity in nuclear sizes and nuclear number density were observed in the histology corresponding to the regions that responded to therapy (29). The increase in randomization of scattering structures following different forms of cell death may explain part of the differences in ultrasound backscatter between regions of a tumour that responded and did not respond to therapy and between viable and damaged tissue. However, one may expect no increase in UIB for highly heterogeneous tissues, similar to the result obtained from C666-1 cell samples treated with radiotherapy (Figure 5.8).

The focus of this chapter was to explore if the increase in the randomness of nuclear positions in cell samples undergoing cell death, contributed to the increases in UIB measured from these cell samples. While the idea of one-dimensional analysis is useful, a more realistic model would be two and three-dimensional analysis for the spatial distribution of scatterers. Two dimensional simulations were performed previously, yielding similar results, i.e., increase of ultrasound scattering strength with increase in the randomness of scatterer positions (70, 72, 73). The purpose of one-dimensional simulation here was to gain insight as to how the increase in the variance of cellular size with cell death changes the UIB. The model considered tightly packed cells and scattering occurring from the nucleus

that occupies the center of the cell. No scattering occurred from other parts of the cell. While each nucleus could have larger or smaller scattering cross-section depending on its size and physical attributes, this model considered only the effect of randomization that resulted from changes in the variance of cellular size, with no further changes in nuclei position inside the cell with cell death.

With all these simplifications, the model predictions are consistent with the experimental data. The model appears to be a good starting point to explain how such small physical changes in a cell could produce such large changes (i.e., up to six fold increase) in the measured ultrasound backscatter (Figure 5.4 and Table 5-2). Furthermore, the model explained why some cell samples (C666-1), that appeared to undergo cell death after radiotherapy exhibited no increases in UIB, as did the other two cell lines (FaDu and Hep-2).

5.7 Conclusion

This chapter indicated that the increase in the randomization of nuclear positions has a contribution to the increase in ultrasound scattering measured following cell death. The randomization was expressed as a function of the variance of cellular size in a given sample. These findings could have important implications for ultrasound characterization of cell death and tissue characterization in general, since the increase of the cell size variance is likely common to the most forms of cell death: apoptosis, mitotic arrest/catastrophe, the mix of apoptosis and mitotic arrest/catastrophe. Therefore, pathologies that result in cell death can be potentially identified using ultrasound methods. More experimental and theoretical evaluations are needed to develop these concepts. One approach would be to separate the contribution of the intrinsic nuclear properties (e.g., size, acoustic impedance) from the contribution of spatial organization to ultrasound scattering. Ongoing research in

our laboratory aims to precisely and reliably measure the nucleus acoustic properties as a function of treatment (41). These values can serve as inputs into classical scattering models (e.g. Gaussian, fluid sphere, spherical shell) or new developed cell models (87). The comparison of theoretical ultrasound backscatter spectra with the experimental data may help to estimate the contribution of randomization to UIB for different types of treatments in specific cell lines.

6 CONCLUSION AND FUTURE WORK

6.1 Conclusion

In this thesis I demonstrated that ultrasound imaging (10 to 30 MHz) and quantitative ultrasound methods are able to non-invasively detect early responses to radiotherapy *in vitro* and *in vivo*. The mechanism behind this detection was linked to changes in the acoustic properties of cells and/or nuclei and changes in the spatial organization of cells and nuclei following cell death. The work brings new experimental evidence that randomization in the spatial organization of nuclei contributes to the increase in ultrasound scattering following cell death. This final chapter summarizes the conclusions and presents possible future directions.

In Chapter 3 it was shown that ultrasound imaging and ultrasound spectral parameters, the UIB and SS, measured from cell samples can be used in the laboratory, in well-controlled conditions, to monitor response of cells to radiation treatment *in vitro*. These results represent the first body of work on the use of ultrasound spectral parameters to detect radiotherapy effects *in vitro* and differentiate between cells that die predominantly by mitotic arrest/catastrophe from cells that die predominately by a mix of apoptosis and mitotic arrest.

In Chapter 4, tumour response to radiotherapy in preclinical xenograft cancer mouse models were characterized by three ultrasound spectral parameters: UIB, SS and SI. These spectral parameters were employed, firstly, to compute the average ultrasound spectral parameters within a demarcated spatial region and, secondly, to generate parametric images. It was demonstrated that ultrasound images enhanced by spatial maps constructed

from ultrasound spectral parameters were capable of non-invasively detecting cell death in tumours, as early as 24 hours after radiotherapy at the clinically relevant ultrasound frequencies of 10 to 30 MHz. These results indicate that cells structural changes following cell death have a significant influence on spectral parameters, providing a framework for future experiments and/or clinical studies aiming to demonstrate the potential of rapidly and non-invasively monitoring the effects of radiotherapy and other anticancer treatments using an ultrasound based approach.

Biological tissues are complex structures consisting of cells of different sizes and different composition among which are intermixed blood vessels. These structures scatter ultrasound differently depending on their mechanical properties and ultrasound interrogating frequency, resulting in complex interference patterns that may explain why fundamental ultrasonic scattering structures in tissues are still poorly understood. Cell samples, used in this thesis, are a simplified representation of a tumor likely to contain cells of approximately same size, similar acoustic properties and packing but without the added complexity of other structures (e.g., blood vessels, collagen, muscles, skin), whereas a tumor xenograft contains most of these structures characteristics of biological tissues. Rather than resolving individual structures, ultrasound spectrum analysis estimates the statistical properties of tissue structures. Considering that tumor cells are the dominant component of cell samples and tumors, it is reasonable to expect that ultrasound parameters (related to cellular statistical properties at the frequencies used in this work) to be similar in cell samples and tumor xenografts. This is verified by the SS estimated from cell samples (Chapter 3) and tumours (Chapter 4) that yielded similar values indicating that the same scattering structure dominates the ultrasound scattering in cell samples and tumour xenografts, regardless of a more heterogeneous structure of a tumor compared with a cell sample. Assuming a Gaussian model, the values of the effective scatterer sizes estimated from the SS (equation

2.12) were close to the cellular sizes estimated from histology (Table 6-1). This suggests that structures in the size range of cells dominate the backscatter characteristics from cell samples and tumour xenografts, regardless of a more heterogeneous structure of a tumor compared with cell sample as also indicated by other investigators (67).

Cell line	SS +/- SE (dB/MHz) Cell samples (n=3)	SS +/- SE (dB/MHz), tumour (n=6)	Effective scatterer size \pmSD (μm)	Nuclear and cellular sizes \pmSD (μm)	UIB cell samples (dB) (n=3)	UIB mouse tumours (dB) (n=6)
FaDu	0.53 \pm 0.07	0.54 \pm 0.05	26.7 \pm 2.6	11.7 \pm 2.2 16.6 \pm 7.5	-50.5 \pm 0.7	-53.0 \pm 0.8
C666-1	0.71 \pm 0.06	0.77 \pm 0.03	19.3 \pm 3.2	10.0 \pm 2.4 13.0 \pm 26	-45.7 \pm 1.2	-56.2 \pm 0.4

Table 6-1. The SS and UIB measured from cell samples and tumour xenografts, effective scatterer size and average nuclear size measured from the histological staining of cell samples and cellular size (as per Table 5-2).. Hoechst fluorescent staining was used to estimate the average size of nuclei with up to 50 nuclei measured per cell sample.

Similar values of UIB were measured from cell samples and tumour xenografts for the FaDu tumour cell line. In Chapter 2-Figure 2.6 are presented comparative H&E images of a FaDu cell sample and tumour indicating similar arrangement of cells in a cell sample and tumour. However, the UIB values for the C666-1 cell samples were significantly larger than the UIB values measured from tumour xenografts, about 10 dB difference (Table 6-1). This difference in the UIB values between C666-1 cell samples and tumours can be explained based on the results from Chapter 5 in which was indicated that an increase in the variance of cellular size contributes to the increase in ultrasound backscatter. The C666-1

cell culture demonstrates a specific phenotype consisting of adherent cells (diameter of $\sim 14 \mu\text{m}$) and a small proportion of cells growing in suspension (diameter of $\sim 9 \mu\text{m}$) resulting in a large variance of cellular size in the C666-1 cell sample (Chapter 5, Figure 5.7 C). The cells growing in suspension were not represented in tumour xenografts that exhibited a more uniform composition with cells of approximately similar size (Figure 6.1). Therefore, the larger variance of cellular size in C666-1 cell samples, six times larger than in tumours (Figure 6.1) may provide an explanation for the larger UIB values measured from cell samples, consistent with the findings from Chapter 5.

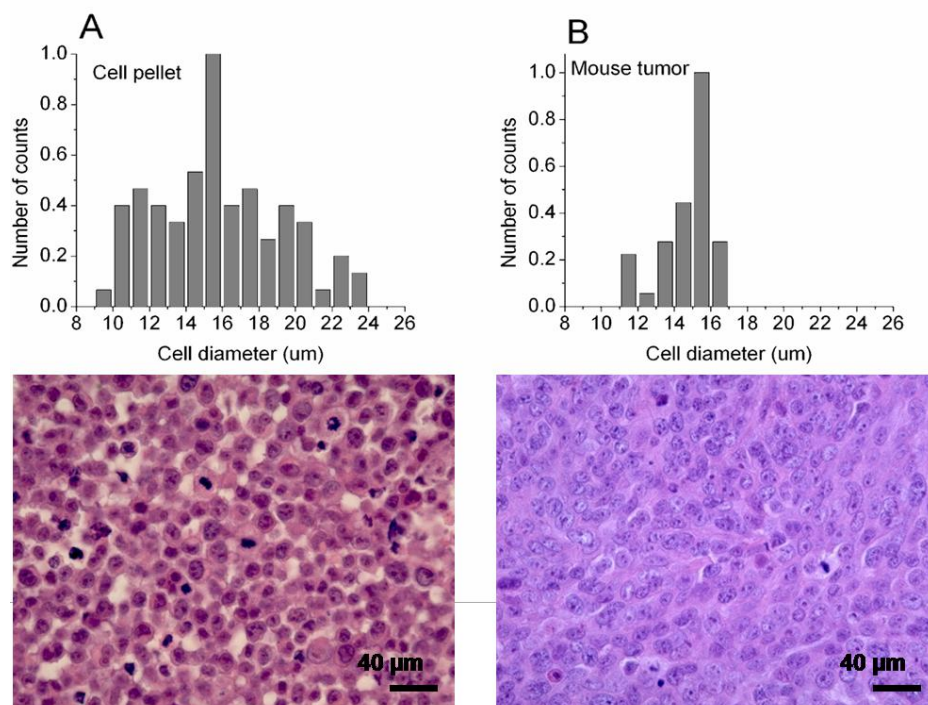


Figure 6.1 Histograms of cell size distribution and corresponding H&E staining for (A) C666-1 cell sample and (B) C666-1 mouse tumour. The variance of cellular size estimated from histology (100 cells were measured) yielded values of 12.8 and 2.3 for the cell sample and mouse tumour, respectively. The histograms were normalized to one, by dividing each count to the maximum count. The histology of the cell sample has an appearance of larger heterogeneity in cellular size compared with the histology of mouse tumour.

6.2 Implications

This thesis contributes to the field of tissue characterization in several ways. Firstly, it demonstrate that ultrasound imaging (10 to 30 MHz) and quantitative ultrasound methods are able to non-invasively detect early responses to radiotherapy *in vitro* and *in vivo*. This could provide the benefit of determining tumour response to anti-cancer therapies early,

within days after the start of treatment, potentially as early as 24 hours, as indicated in this work. An early predictor of treatment response would be of great value to provide individualized treatment to cancer patients and particularly promising in multistage interventions or combination treatments. The tumours treated with radiotherapy exhibited a heterogeneous response with regions of cell death of irregular shape, as revealed by the TUNEL staining that corresponded to the hyperechogenic regions in the ultrasound images (Chapter 4, Figures 4.2 and 4.4). In order to characterize these irregular shapes more rigorously, parametric images were computed from the local estimates of the ultrasonic parameters. It was demonstrated that ultrasound methods are capable to detect cell death and may help to characterize the heterogeneity of tumour response to radiotherapy. The tumour response to radiation appears to be more complex than originally thought, as observed in the response exhibited by the tumour xenografts treated with radiotherapy in this thesis and also indicated by recent investigations (136).

Secondly, assuming a Gaussian model to predict the ultrasound scattering, the ultrasound estimates of the effective scatterer sizes calculated from the viable cell samples and untreated mouse tumour yielded values close to the cellular sizes. This constitutes an important result indicating that the changes observed in ultrasonic parameters could be linked to changes in cellular structure, therefore, can be used to identify different pathologies that modify the acoustic properties of cell, including cell death. For example, data presented in Chapter 3 indicate that spectral parameters were able to differentiate between cells that die predominantly by mitotic arrest or catastrophe from cells that die predominantly by a mixture of apoptosis and mitotic arrest.

The results presented in Chapter 5 provide new insights into the physics of ultrasound scattering from cell ensembles undergoing cell death. These results indicated that the increase in the variance of cellular size following cell death contributes to the increase in

ultrasound scattering. These findings could have important implications for ultrasound characterization of cell death since the increase in cell size variance is common to most forms of cell death (i.e., apoptosis, mitotic arrest/catastrophe). These results also suggest that scientists working towards tissue characterization should be prudent in choosing the cell lines or tissues models to characterize cell death. As demonstrated in Chapter 5, cell samples with a large distribution of cell sizes may exhibit no increase in UIB following cell death, similar to the result obtained from C666-1 cell samples treated with radiotherapy.

Finally, these results indicate that a theoretical framework that considers the degree of orderliness of tissue scattering structure is necessary in order to more accurately characterize tissue pathologies using quantitative ultrasound. For instance, ultrasound backscatter measured from ensembles of scatterers with similar acoustic properties but different degree of randomization may have different ultrasound backscatter values. Moreover, diseases that alter the acoustic properties of scattering structures may also alter their inherited spatial organization. The degree of orderliness of scattering structures has an influence on ultrasound scattering and therefore needs to be considered in tissue characterization algorithms.

6.3 Future work

The future work presented in this chapter has three main directions. The first part proposes future studies to validate this method for applications in preclinical and clinical studies. The second part suggests some general directions in order to quantify cell death in a given cell ensemble. The third part reviews the current criteria to assess solid tumour responses in clinical trials and proposes general directions to incorporate the QUS methods in clinical trial design.

6.3.1 Future work, registration of whole mount tumour histology with 3D ultrasound and parametric images

In Chapter 4, changes in ultrasound images and spectral parameters measured from mouse tumours were correlated with changes estimated from tumour histology. It was concluded that the changes in the spectral parameters were direct consequences of cell death. The tumours were excised and sectioned in the same nominal orientation to best match the ultrasound scanning planes. Ultrasound and histological images were registered by visual comparison of tumour size and, similarities of tumor edge.

Currently, stained histological sections are considered the gold standard for cancer diagnosis, detection of cell death and assessment of tumour response. In order to adopt the ultrasound images and QUS methods in preclinical and clinical applications, it will be of interest to know how well the volume of cell death in ultrasound and parametric images corresponds to the true value in histology. The knowledge of how the margins of the region of cell death represented in ultrasound and parametric images correspond to the margins of the area of cell death as assessed from histology can be used to develop new clinical applications, e.g. guiding needle and surgical excision biopsies for diagnostic purposes using ultrasound methods.

In order to compare the correspondence between the hyperechoic volume and the volume of cell death reconstructed from the ultrasound images and histological staining of the tumour slices, respectively, the whole-mount tumour histology volume can be registered with 3D ultrasound representation of the tumour. To reconstruct the hyperechoic and cell death volumes, the hyperechoic regions in the 2D ultrasound images and the area of cell death in tumour histology can be manually contoured or using automated segmentation

algorithms based on image intensity. Finally, finite element based-analysis can be used to estimate the reconstructed volumes and relationship between them.

6.3.2 Future work, predicting the contribution of nuclear acoustic properties and nuclei spatial organization to ultrasound backscatter

Overall, the results presented in Chapters 3 to 5 indicated that the nuclei change their size, acoustic impedance and spatial distribution following cell death resulting in changes of scattering frequency dependence and magnitude of ultrasound backscatter. The contribution of each of these changes to ultrasound backscatter appeared to be dependent on the forms of cell death. In order to determine the proportion of cells undergoing cell death in a biological tissue and, thus, quantifying cell death is necessary to discern between the contribution of nuclear intrinsic properties and the contribution of nuclear spatial organization to the ultrasound scattering in an analyzed sample.

Intrinsic acoustic cellular and nuclear properties can be measured using acoustic microscopy or microrheology techniques. For instance, acoustic microscopy scanners allow simultaneous optical microscopy and acoustical microscopy imaging of a single cell and can be used to correlate changes in the acoustical properties and morphological features in a single cell. Once the cell acoustical properties will be estimated, they can serve as input parameters to model scattering from a single cell. To model scattering from a cell ensemble, the position of each scatterer with the cell acoustic properties can be generated as a function of cellular size variance measured as described in Chapter 5. The corresponding phase-shifts resulting from this arrangement can be calculated and the individual contributions to the ultrasound field summed to model the theoretical ultrasound scattering.

Another approach will be to consider that nuclei are suspended scatterers in a continuum of cytoplasm. For instance, an ensemble of cells can be modeled as a

distribution of randomly-spaced fluid spheres with nucleus like properties. Other scattering models to describe the cell scattering, i.e., spherical shell, Gaussian, or newly developed cell models (87) can also be considered. The theoretical models of ultrasound backscatter can be fitted to the normalized backscatter power measured experimentally. Typically, a gain factor is used to correct for any magnitude bias in the normalized power spectra from the cell sample and the theoretical power spectra (87). Since the initial assumption is that the scatterers are randomly distributed, the gain factor can be used to infer the contribution of randomization to the ultrasound backscatter.

It would also be of interest to derive a specific relationship between the changes in the ultrasound spectral parameters and increase in the variance of cellular sizes. For example, the variance of cellular sizes can be tightly controlled within a large range of values using mixtures of two different cell lines with distinct cell sizes in different proportions. This type of data may provide stronger algorithms for tissue characterization using ultrasound spectral parameters and may provide input to a theoretical framework for ultrasound tissue characterization that takes into account the degree of randomization of tissue scattering structures.

6.3.3 Future directions in characterization of cell death using QUS methods

The long-term goal of this work is the development of ultrasound tissue characterization techniques to assess tumour responses to radiotherapy and other anticancer therapies in cancer patients using ultrasound. The spectral parameters UIB, SS and SI can be used to differentiate response to radiation treatment. Parameters computed from ultrasound spectra can be displayed numerically and graphically. However in a clinical setting, results are often best analyzed and interpreted when information is presented in an image format. Therefore,

the spectral analysis techniques can be clinically developed in two complementary modes. The first mode computes the averaged spectral parameters within a demarcated spatial region that can be delineated by an operator. These parameters can be displayed numerically and graphically to follow the tumour evolution before and multiple times after treatment. The spectral parameters can be used to construct a clinical data base and develop classification procedures for differentiating treatment response. The second mode generates spectral parameter images that display the distribution of parameter values and may indicate a heterogeneous response of the tumour and treatment evolution. The treated tumour may present no early change in tumour volume, shape or other macroscopic traits but may present significant changes in cellular and nuclear properties. These changes can be detected by ultrasound spectral parameters and determine whether the therapy is successful.

The implementation of QUS methods is not difficult. The QUS automated algorithms can be implemented on modern clinical scanners with RF data collection and processing capabilities. Therefore, real-time display of QUS images could easily become a reality. In addition to ultrasound imaging and spectral parameters, changes in the tumour vasculature with the applied treatment can potentially represent another indicator of tumour response (136). Studies in progress in our laboratory using mid to high frequency Doppler ultrasound to assess changes in tumour vasculature following different cancer therapies have correlated these changes with tumour histology and intratumoural blood vessel density. Ultrasound imaging, QUS methods and high frequency Doppler ultrasound can be integrated on the same ultrasound machine and may provide a complete assessment of tumour response (cells and vasculature) to the applied therapy.

Traditionally, response evaluation criteria in solid tumours (RECIST) guidelines are applied to clinical trials to evaluate the tumour response and determine whether the

agent/regimen demonstrates sufficiently encouraging results to warrant further testing (71). Taking into account the changes in the longest diameter of the assessed tumour, the criteria for a complete response is the disappearance of all target lesions; partial response means at least 30% decrease in the longest diameter of the target lesion; progressive disease is at least 20% increase in the longest diameter of the target lesion with stable disease being defined as neither sufficient shrinkage to qualify for partial response nor sufficient increase to qualify for progressive disease. Evaluation of tumour response following these criteria is typically conducted at six to eight weeks after treatments starts and re-evaluation or confirmation of response is performed at four weeks after the criteria for response are first met. In this context, early non-invasive detection of cell death, within days after start of treatment has a good potential to improve clinical trial efficiency, aid in the development of novel targeted therapies and provide input to individualized treatment planning.

Ultrasound imaging and QUS methods can be incorporated into clinical trial designs. For instance, in new drug development, changes in ultrasound images and ultrasound parameters can be used to monitor therapy response and potentially predict outcome. The molecular phenotypes of tumours may affect patient specific response to certain therapies. In this context, the ultrasound parameters can be used as functional image biomarkers to predict the response and stratify patients based on their response. Since only the patients who are responsive to therapy will continue these trials, this may result in reducing the number of patients required for a clinical study. Consequently, this may result in a decrease in the costs of clinical trials and the time for a drug to reach market. Furthermore, identifying therapies for individual patients can prevent adverse drug reactions avoiding ineffective treatments.

7 REFERENCES

1. Tannock IF, Hill RP, Bristow RG, Harrington L. The basic science of oncology. 4th ed. Tannock I, editor. New York: McGraw-Hill; 2005.
2. Koong AC, Le QT, Ho A, Fong B, Gibbs IC, Fisher G, et al. Phase I study of stereotactic radiosurgery in patients with locally advanced pancreatic cancer. *International Journal of Radiation Oncology Biology Physics* 2004;58(4):1017-21.
3. Lutz ST, Chow EL, Hartsell WF, Konski AA. A review of hypofractionated palliative radiotherapy. *Cancer* 2007;109(8):1462-70.
4. Dawson LA, Eccles C, Bissonnette JP, Brock KK. Accuracy of daily image guidance for hypofractionated liver radiotherapy with active breathing control. *Int J Radiat Oncol Biol Phys* 2005;62(4):1247-52.
5. Darzynkiewicz Z, Juan G, Li X, Gorczyca W, Murakami T, Traganos F. Cytometry in cell necrobiology: Analysis of apoptosis and accidental cell death (necrosis). *Cytometry* 1997;27(1):1-20.
6. Lockshin RA, Tilly JL, Zakeri Z. When cells die : A comprehensive evaluation of apoptosis and programmed cell death. New York: Wiley-Liss; 1998.
7. Van Cruchten S, Van den Broeck W. Morphological and biochemical aspects of apoptosis, oncosis and necrosis. *Anatomia* 2002;31(4, pp. 214-223):August 2002.
8. Brindle K. New approaches for imaging tumour responses to treatment. *Nat Rev Cancer* 2008;8(2):94-107.
9. Von Schulthess GK, Steinert HC, Hany TF. Integrated PET/CT: Current applications and future directions. *Radiology* 2006;238(2):405-22.

10. Weber WA, Figlin R. Monitoring cancer treatment with PET/CT: Does it make a difference? *J Nucl Med* 2007;48(Suppl 1):36S-44S.

11. Weber WA, Petersen V, Schmidt B, Tyndale-Hines L, Link T, Peschel C, et al. Positron emission tomography in non-small-cell lung cancer: Prediction of response to chemotherapy by quantitative assessment of glucose use. *J Clin Oncol* 2003;21(14):2651-7.

12. Weber WA, Ott K, Becker K, Dittler HJ, Helmberger H, Avril NE, et al. Prediction of response to preoperative chemotherapy in adenocarcinomas of the esophagogastric junction by metabolic imaging. *J Clin Oncol* 2001;19(12):3058-65.

13. Spaepen K, Stroobants S, Dupont P, Van Steenweghen S, Thomas J, Vandenberghe P, et al. Prognostic value of positron emission tomography (PET) with fluorine-18 fluorodeoxyglucose ([¹⁸F]FDG) after first-line chemotherapy in non-hodgkin's lymphoma: Is [¹⁸F]FDG-PET a valid alternative to conventional diagnostic methods?. *J Clin Oncol* 2001;19(2):414-9.

14. Weber WA, Wieder H. Monitoring chemotherapy and radiotherapy of solid tumors. *Eur J Nucl Med Mol Imaging* 2006;33(Suppl 1):27-37.

15. Cobbold, R. S. C. *Foundations of biomedical ultrasound*, chapter 5 . Oxford University Press, USA; 1 edition; 2006.

16. Shung KK, Thieme GA. *Ultrasonic scattering in biological tissues*, chapters 3-5. Shung KK and Thieme GA, editors. CRC Press; 1993.

17. Wilson SR, Jang HJ, Kim TK, Burns PN. Diagnosis of focal liver masses on ultrasonography: Comparison of unenhanced and contrast-enhanced scans. *J Ultrasound Med* 2007;26(6):775-87.

18. Foster FS, Burns PN, Simpson DH, Wilson SR, Christopher DA, Goertz DE. Ultrasound for the visualization and quantification of tumor microcirculation. *Cancer Metastasis Rev* 2000;19(1-2):131-8.
19. Foster FS, Pavlin CJ, Harasiewicz KA, Christopher DA, Turnbull DH. Advances in ultrasound biomicroscopy. *Ultrasound Med Biol* 2000;26(1):1-27.
20. Foster FS, Zhang MY, Zhou YQ, Liu G, Mehi J, Cherin E, et al. A new ultrasound instrument for in vivo microimaging of mice. *Ultrasound Med Biol* 2002;28(9):1165-72.
21. Foster FS, Zhang M, Duckett AS, Cucevic V, Pavlin CJ. In vivo imaging of embryonic development in the mouse eye by ultrasound biomicroscopy. *Invest Ophthalmol Vis Sci* 2003;44(6):2361-6.
22. Graham KC, Wirtzfeld LA, MacKenzie LT, Postenka CO, Groom AC, MacDonald IC, et al. Three-dimensional high-frequency ultrasound imaging for longitudinal evaluation of liver metastases in preclinical models. *Cancer Res* 2005;65(12):5231-7.
23. Cheung AM, Brown AS, Hastie LA, Cucevic V, Roy M, Lacefield JC, et al. Three-dimensional ultrasound biomicroscopy for xenograft growth analysis. *Ultrasound Med Biol* 2005;31(6):865-70.
24. Goertz DE, Yu JL, Kerbel RS, Burns PN, Foster FS. High-frequency doppler ultrasound monitors the effects of antivasular therapy on tumor blood flow. *Cancer Res* 2002;62(22):6371-5.
25. Huizen IV, Wu G, Moussa M, Chin JL, Fenster A, Lacefield JC, et al. Establishment of a serum tumor marker for preclinical trials of mouse prostate cancer models. *Clin Cancer Res* 2005;11(21):7911-9.

26. Czarnota GJ, Kolios MC, Abraham J, Portnoy M, Ottensmeyer FP, Hunt JW, et al. Ultrasound imaging of apoptosis: High-resolution non-invasive monitoring of programmed cell death *in vitro*, *in situ* and *in vivo*. *Br J Cancer* 1999;81(3):520-7.
27. Kolios MC, Czarnota GJ, Lee M, Hunt JW, Sherar MD. Ultrasonic spectral parameter characterization of apoptosis. *Ultrasound Med Biol* 2002;28(5):589-97.
28. Vlad RM, Czarnota GJ, Giles A, Sherar MD, Hunt JW, Kolios MC. High-frequency ultrasound for monitoring changes in liver tissue during preservation. *Phys Med Biol* 2005;50(2):197-213.
29. Vlad RM, Brand S, Giles A, Kolios MC, Czarnota GJ. Quantitative ultrasound assessing tumor responses to radiotherapy in cancer mouse models . *Ultrasonic Imaging*. 2008;29:255-6.
30. Dubray B, Breton C, Delic J, Klijanienko J, Maciorowski Z, Vielh P, et al. In vitro radiation-induced apoptosis and early response to low-dose radiotherapy in non-hodgkin's lymphomas. *Radiother Oncol* 1998;46(2):185-91.
31. Symmans WF, Volm MD, Shapiro RL, Perkins AB, Kim AY, Demaria S, et al. Paclitaxel-induced apoptosis and mitotic arrest assessed by serial fine-needle aspiration: Implications for early prediction of breast cancer response to neoadjuvant treatment. *Clin Cancer Res* 2000;6(12):4610-7.
32. Roberg K, Jonsson AC, Grenman R, Norberg-Spaak L. Radiotherapy response in oral squamous carcinoma cell lines: Evaluation of apoptotic proteins as prognostic factors. *Head Neck* 2007;29(4):325-34.

33. Tordiglione M, Antognoni P, Danova M. The biological significance and clinical prospects of apoptosis within the parameters of radiotherapy response. *Radiol Med (Torino)* 1996;91(3):286-91.
34. Moffat BA, Chenevert TL, Lawrence TS, Meyer CR, Johnson TD, Dong Q, et al. Functional diffusion map: A noninvasive MRI biomarker for early stratification of clinical brain tumor response. *Proc Natl Acad Sci U S A* 2005;102(15):5524-9.
35. Boersma HH, Kietselaer BL, Stolk LM, Bennaghmouch A, Hofstra L, Narula J, et al. Past, present, and future of annexin A5: From protein discovery to clinical applications. *J Nucl Med* 2005;46(12):2035-50.
36. Czarnota GJ, Kolios MC, Vaziri H, Benchimol S, Ottensmeyer FP, Sherar MD, et al. Ultrasonic biomicroscopy of viable, dead and apoptotic cells. *Ultrasound Med Biol* 1997;23(6):961-5.
37. Kolios MC, Taggart L, Baddour RE, Foster FS, Hunt JW, Czarnota GJ, et al. An investigation of backscatter power spectra from cells, cell pellets and microspheres. *Ultrasonics Symposium, IEEE 2003;Volume: 1:752-7.*
38. Tunis AS, Baddour RE, Czarnota GJ, Giles A, Worthington AE, Sherar MD, et al. Using high frequency ultrasound envelope statistics to determine scatterer number density in dilute cell solutions. *Ultrasonic symposium IEEE 2005;Volume 2:878-81.*
39. Vlad RM, Alajez NM, Giles A, Kolios MC, Czarnota GJ. Quantitative ultrasound characterization of cancer radiotherapy effects in vitro *Int J of Radiat Oncol Biol Phys* 2008;72(4):1236-43.

40. Taggart LR, Baddour RE, Giles A, Czarnota GJ, Kolios MC. Ultrasonic characterization of whole cells and isolated nuclei. *Ultrasound Med Biol*. 2007;33(3):389-401.
41. Brand S, Weiss EC, Lemor RM, Kolios MC. High frequency ultrasound tissue characterization and acoustic microscopy of intracellular changes. *Ultrasound Med Biol*. 2008;34(9):1396-407.
42. Banihashemi B, Vlad RM, Giles A, Kolios MC, Czarnota GJ. Ultrasound imaging of apoptosis in tumour response: Novel monitoring of photodynamic therapy effects. *Cancer Research* 2008;68(20):8590-6.
43. Lizzi FL, Ostromogilsky M, Feleppa EJ, Rorke MC, Yaremko MM. Relationship of ultrasonic spectral parameters to features of tissue microstructure. *IEEE Transactions on Ultrasonics, Ferroelectrics and Frequency Control* 1987;34(3):319-29.
44. Lizzi FL, King DL, Rorke MC, Hui J, Ostromogilsky M, Yaremko MM, et al. Comparison of theoretical scattering results and ultrasonic data from clinical liver examinations. *Ultrasound Med Biol* 1988;14(5):377-85.
45. Coleman DJ, Lizzi FL, Silverman RH, Helson L, Torpey JH, Rondeau MJ. A model for acoustic characterization of intraocular tumors. *Invest Ophthalmol Vis Sci* 1985;26(4):545-50.
46. Insana MF, Garra BS, Rosenthal SJ, Hall TJ. Quantitative ultrasonography. *Med Prog Technol* 1989;15(3-4):141-53.
47. Garra BS, Insana MF, Shawker TH, Wagner RF, Bradford M, Russell M. Quantitative ultrasonic detection and classification of diffuse liver disease. comparison with human observer performance. *Invest Radiol* 1989;24(3):196-203.

48. Mimbs JW, O'Donnell M, Miller JG, Sobel BE. Detection of cardiomyopathic changes induced by doxorubicin based on quantitative analysis of ultrasonic backscatter. *Am J Cardiol* 1981;47(5):1056-60.
49. Lizzi FL, Greenebaum M, Feleppa EJ, Elbaum M, Coleman DJ. Theoretical framework for spectrum analysis in ultrasonic tissue characterization. *J Acoust Soc Am* 1983;73(4):1366-73.
50. Feleppa EJ, Lizzi FL, Coleman DJ, Yaremko MM. Diagnostic spectrum analysis in ophthalmology: A physical perspective. *Ultrasound Med Biol* 1986;12(8):623-31.
51. Lizzi FL, Driller J, Ostromogilsky M. Thermal model for ultrasonic treatment of glaucoma. *Ultrasound Med Biol* 1984;10(3):289-98.
52. Feleppa EJ, Kalisz A, Melgar S, J. B., Lizzi, F. L., Tian L, Rosado AL, et al. Typing of prostate tissue by ultrasonic spectrum analysis. *IEEE Trans. Ultrason., Ferroelec., Freq. Contr.* 1996;43(4):609-19.
53. Lizzi FL. Ultrasonic scatterer-property images of the eye and prostate. *Proc IEEE Ultrason Symp* 1997;2:1109-18.
54. Ursea R, Coleman DJ, Silverman RH, Lizzi FL, Daly SM, Harrison W. Correlation of high-frequency ultrasound backscatter with tumor microstructure in iris melanoma. *Ophthalmology* 1998;105(5):906-12.
55. Lizzi FL, Feleppa EJ, Kaiser AS, Deng CX. Ultrasonic spectrum analysis for tissue evaluation. *Pattern Recognition Letters* 2003;24(4):637-58.
56. Lizzi FL, Coleman DJ. History of ophthalmic ultrasound. *J Ultrasound Med* 2004;23(10):1255-66.

57. Balaji KC, Fair WR, Feleppa EJ, Porter CR, Tsai H, Liu T, et al. Role of advanced 2 and 3-dimensional ultrasound for detecting prostate cancer. *J Urol* 2002;168(6):2422-5.
58. Insana MF, Hall TJ, Fishback JL. Identifying acoustic scattering sources in normal renal parenchyma from the anisotropy in acoustic properties. *Ultrasound Med Biol* 1991;17(6):613-26.
59. Insana MF, Hall TJ. A method for characterizing soft tissue microstructure using parametric ultrasound imaging. *Prog Clin Biol Res* 1991;363:241-56.
60. Garra BS, Insana MF, Sesterhenn IA, Hall TJ, Wagner RF, Rotellar C, et al. Quantitative ultrasonic detection of parenchymal structural change in diffuse renal disease. *Invest Radiol* 1994;29(2):134-40.
61. Kovacs A, Courtois MR, Weinheimer CJ, Posdamer SH, Wallace KD, Holland MR, et al. Ultrasonic tissue characterization of the mouse myocardium: Successful in vivo cyclic variation measurements. *J Am Soc Echocardiogr* 2004;17(8):883-92.
62. Yang M, Krueger TM, Miller JG, Holland MR. Characterization of anisotropic myocardial backscatter using spectral slope, intercept and midband fit parameters. *Ultrason Imaging* 2007;29(2):122-34.
63. Ursea R, Coleman DJ, Silverman RH, Lizzi FL, Daly SM, Harrison W. Correlation of high-frequency ultrasound backscatter with tumor microstructure in iris melanoma. *Ophthalmology* 1998;105(5):906-12.
64. Silverman RH, Folberg R, Rondeau MJ, Boldt HC, Lloyd HO, Chen X, et al. Spectral parameter imaging for detection of prognostically significant histologic features in uveal melanoma. *Ultrasound Med Biol* 2003;29(7):951-9.

65. Coleman DJ, Silverman RH, Rondeau MJ, Boldt HC, Lloyd HO, Lizzi FL, et al. Noninvasive in vivo detection of prognostic indicators for high-risk uveal melanoma: Ultrasound parameter imaging. *Ophthalmology* 2004;111(3):558-64.
66. Oelze ML, O'Brien WD,Jr, Blue JP, Zachary JF. Differentiation and characterization of rat mammary fibroadenomas and 4T1 mouse carcinomas using quantitative ultrasound imaging. *IEEE Trans Med Imaging* 2004;23(6):764-71.
67. Oelze ML, Zachary JF. Examination of cancer in mouse models using high-frequency quantitative ultrasound. *Ultrasound Med Biol* 2006;32(11):1639-48.
68. Insana MF. Ultrasonic imaging of microscopic structures in living organs. *Int Rev Exp Pathol* 1996;36:73-92.
69. Czarnota GJ, Kolios MC, Hunt JW, Sherar MD. Ultrasound imaging of apoptosis. DNA-damage effects visualized. *Methods Mol Biol* 2002;203:257-77.
70. Tunis AS, Czarnota GJ, Giles A, Sherar MD, Hunt JW, Kolios MC. Monitoring structural changes in cells with high-frequency ultrasound signal statistics. *Ultrasound Med Biol* 2005;31(8):1041-9.
71. Jaffe CC. Measures of response: RECIST, WHO, and new alternatives. *J Clin Oncol* 2006;24(20):3245-51.
72. Hunt JW, Worthington AE, Kerr AT. The subtleties of ultrasound images of an ensemble of cells: Simulation from regular and more random distributions of scatterers. *Ultrasound Med Biol* 1995;21(3):329-41.
73. Hunt JW, Worthington AE, Xuan A, Kolios MC, Czarnota GJ, Sherar MD. A model based upon pseudo regular spacing of cells combined with the randomisation of the

nuclei can explain the significant changes in high-frequency ultrasound signals during apoptosis. *Ultrasound Med Biol* 2002;28(2):217-26.

74. Encyclopedia of acoustics. Crocker MJ, editor. Toronto: Wiley; 1997.

75. Bushberg JT. The essential physics of medical imaging. 2nd ed. Philadelphia: Lippincott; 2002.

76. Morse PM, Ingard K. Theoretical acoustics. McGraw-Hill; 1968.

77. Rayleigh JWS. The theory of Sound. Dover Classics of Science and Mathematics, 1945.

78. Ishimaru A. Wave propagation and scattering in random media. New York: Oxford University Press; 1997.

79. Faran JJ. Sound scattering by solid cylinders and spheres. *J Acoust Soc Am*. 1951;23:405-18.

80. Insana MF, Wagner RF, Brown DG, Hall TJ. Describing small-scale structure in random media using pulse-echo ultrasound. *J Acoust Soc Am*. 1990;87(1):179-92.

81. Roy RA. Quantitative particle characterization by scattered ultrasound (Ph.D. thesis); University of Cambridge (England), 1987.

82. Couture O. Ultrasound echoes from targeted contrast agents (Ph.D. thesis); University of Toronto (Canada), 2007.

83. Chin CT. Modelling the behaviour of microbubble contrast agents for diagnostic ultrasound (Ph.D. thesis), University of Toronto (Canada); 2001.

84. Shung KK. Ultrasonic characterization of biological tissues. *J Biomech Eng* 1985;107(4):309-14.

85. Insana MF, Wagner RF, Brown DG, Hall TJ. Describing small-scale structure in random media using pulse-echo ultrasound. *J Acoust Soc Am* 1990;87(1):179-92.
86. Oelze ML, Zachary JF, O'Brien WD, Jr. Characterization of tissue microstructure using ultrasonic backscatter: Theory and technique for optimization using a Gaussian form factor. *J Acoust Soc Am* 2002;112(3 Pt 1):1202-11.
87. Oelze ML, O'Brien WD, Jr. Application of three scattering models to characterization of solid tumors in mice. *Ultrason Imaging* 2006;28(2):83-96.
88. Lizzi FL, Astor M, Liu T, Deng C, Coleman DJ, Silverman RH. Ultrasonic spectrum analysis for tissue assays and therapy evaluation. *International Journal of Imaging Systems and Technology* 1997;8(1):3-10.
89. Lizzi FL, Astor M, Feleppa EJ, Shao M, Kalisz A. Statistical framework for ultrasonic spectral parameter imaging. *Ultrasound Med Biol* 1997;23(9):1371-82.
90. Lizzi FL, Astor M, Kalisz A, Liu T, Coleman DJ, Silverman R.H., et al. In: *Ultrasonic spectrum analysis for assays of different scatterer morphologies: theory and very-high frequency clinical results.* ; 1996. p. 1155-9.
91. Feleppa EJ, Porter CR, Ketterling J, Lee P, Dasgupta S, Urban S, et al. Recent developments in tissue-type imaging (TTI) for planning and monitoring treatment of prostate cancer. *Ultrason Imaging* 2004;26(3):163-72.
92. Feleppa EJ, Ennis RD, Schiff PB, Wu CS, Kalisz A, Ketterling J, et al. Spectrum-analysis and neural networks for imaging to detect and treat prostate cancer. *Ultrason Imaging* 2001;23(3):135-46.
93. Mo LYL, Cobbold RSC. A stochastic model of the backscattered doppler ultrasound from blood. *IEEE Transactions on Biomedical Engineering* 1986;BME-33(1):20-7.

94. Mo LYL, Kuo I-, Shung KK, Ceresne L, Cobbold RSC. Ultrasound scattering from blood with hematocrits up to 100%. *IEEE Transactions on Biomedical Engineering* 1994;41(1):91-5.
95. Baddour RE, Kolios MC. The fluid and elastic nature of nucleated cells: Implications from the cellular backscatter response. *J Acoust Soc Am* 2007;121(1):E16-22.
96. Twersky V. Low-frequency scattering by mixtures of correlated nonspherical particles. *J Acoust Soc Am* 1988;84(1):409-15.
97. Twersky V. Low-frequency scattering by correlated distributions of randomly oriented particles. *J Acoust Soc Am* 1987;81(5):1609-18.
98. Sherar MD, Noss MB, Foster FS. Ultrasound backscatter microscopy images the internal structure of living tumour spheroids. *Nature* 1987;330(3):493-5.
99. Jensen JA. A model for the propagation and scattering of ultrasound in tissue. *J Acoust Soc Am*. 1991;89(1):182-90.
100. Fields S, Dunn F. Letter: Correlation of echographic visualizability of tissue with biological composition and physiological state. *J Acoust Soc Am* 1973;54(3):809-12.
101. Goss SA, Dunn F. Ultrasonics propagation properties of collagen. *Phys Med Biol* 1980;25(5):827-37.
102. O'Donnell M, Mimbs JW, Miller JG. The relationship between collagen and ultrasonic attenuation in myocardial tissue. *J Acoust Soc Am* 1979;65(2):512-7.
103. O'Donnell M, Mimbs JW, Miller JG. Relationship between collagen and ultrasonic backscatter in myocardial tissue. *J Acoust Soc Am* 1981;69(2):580-8.

104. Bamber JC, Hill CR, King JA. Acoustic properties of normal and cancerous human liver;dependence on tissue structure. *Ultrasound in Medicine and Biology* 1981;7(2):135-44.
105. Fei DY, Shung KK. Ultrasonic backscatter from mammalian tissues. *J Acoust Soc Am* 1985;78(3):871-6.
106. Kolios MC, Czarnota GJ. In: *New insights into high frequency ultrasonic tissue scattering*. March 5-6, 2008; p. O4-2.
107. Oelze ML, O'Brien Jr., W. D., Zachary JF. High-frequency quantitative ultrasound imaging of solid tumors in mice. *Acoustical Imaging* 2007;28:301-6.
108. Erasmus JJ, Munden RF. The role of integrated computed tomography positron-emission tomography in esophageal cancer: Staging and assessment of therapeutic response. *Semin Radiat Oncol* 2007;17(1):29-37.
109. Brasch RC, Li KC, Husband JE, Keogan MT, Neeman M, Padhani AR, et al. In vivo monitoring of tumor angiogenesis with MR imaging. *Acad Radiol* 2000;7(10):812-23.
110. Preda A, Wielopolski PA, Ten Hagen TL, van Vliet M, Veenland JF, Ambagtsheer G, et al. Dynamic contrast-enhanced MRI using macromolecular contrast media for monitoring the response to isolated limb perfusion in experimental soft-tissue sarcomas. *MAGMA* 2004;17(3-6):296-302.
111. Lassau N, Lamuraglia M, Vanel D, Le Cesne A, Chami L, Jaziri S, et al. Doppler US with perfusion software and contrast medium injection in the early evaluation of isolated limb perfusion of limb sarcomas: Prospective study of 49 cases. *Ann Oncol* 2005;16(7):1054-60.

112. Wang C, Koistinen P, Yang GS, Williams DE, Lyman SD, Minden MD, et al. Mast cell growth factor, a ligand for the receptor encoded by c-kit, affects the growth in culture of the blast cells of acute myeloblastic leukemia. *Leukemia* 1991;5(6):493-9.
113. Pozarowski P, Grabarek J, Darzynkiewicz Z. Flow cytometry of apoptosis. *Curr Protoc Cell Biol* 2004;Chapter 18:Unit 18.8.
114. Lightdale CJ, Kulkarni KG. Role of endoscopic ultrasonography in the staging and follow-up of esophageal cancer. *J Clin Oncol* 2005;23(20):4483-9.
115. Darzynkiewicz Z, Juan G, Bedner E. Determining cell cycle stages by flow cytometry. *Curr Protoc Cell Biol* 2001;Chapter 8:Unit 8.4.
116. Tsien C, Gomez-Hassan D, Chenevert TL, Lee J, Lawrence T, Ten Haken RK, et al. Predicting outcome of patients with high-grade gliomas after radiotherapy using quantitative analysis of T1-weighted magnetic resonance imaging. *Int J Radiat Oncol Biol Phys* 2007;67(5):1476-83.
117. DeVries AF, Kremser C, Hein PA, Griebel J, Krezcy A, Ofner D, et al. Tumor microcirculation and diffusion predict therapy outcome for primary rectal carcinoma. *Int J Radiat Oncol Biol Phys* 2003;56(4):958-65.
118. Theilmann RJ, Borders R, Trouard TP, Xia G, Outwater E, Ranger-Moore J, et al. Changes in water mobility measured by diffusion MRI predict response of metastatic breast cancer to chemotherapy. *Neoplasia* 2004;6(6):831-7.
119. Silverman RH, Coleman DJ, Lizzi FL, Torpey JH, Driller J, Iwamoto T, et al. Ultrasonic tissue characterization and histopathology in tumor xenografts following ultrasonically induced hyperthermia. *Ultrasound in Medicine and Biology* 1986;12(8):639-45.

120. Cheung ST, Huang DP, Hui AB, Lo KW, Ko CW, Tsang YS, et al. Nasopharyngeal carcinoma cell line (C666-1) consistently harbouring epstein-barr virus. *Int J Cancer* 1999;83(1):121-6.
121. Li JH, Chia M, Shi W, Ngo D, Strathdee CA, Huang D, et al. Tumor-targeted gene therapy for nasopharyngeal carcinoma. *Cancer Res* 2002;62(1):171-8.
122. Shung KK. *Diagnostic ultrasound : Imaging and blood flow measurements*. Published by CRC Press, 2005, editor. Boca Raton, FL: Taylor & Francis; 2005.
123. Lizzi FL, Alam SK, Mikaelian S, Lee P, Feleppa EJ. On the statistics of ultrasonic spectral parameters. *Ultrasound Med Biol* 2006;32(11):1671-85.
124. Mamou J, Oelze ML, O'Brien WD,Jr, Zachary JF. Identifying ultrasonic scattering sites from three-dimensional impedance maps. *J Acoust Soc Am* 2005;117(1):413-23.
125. Czarnota GJ, Papanicolau N, Lee J, Karshafian R, Giles A, Kolios MC. Novel low-frequency ultrasound detection of apoptosis *in vitro* and *in vivo*. 33rd International Symposium on Ultrasonic Imaging and Tissue characterization. May, 2008:237-8.
126. Insana MF, Hall TJ, Wood JG, Yan ZY. Renal ultrasound using parametric imaging techniques to detect changes in microstructure and function. *Invest Radiol* 1993;28(8):720-5.
127. Baddour RE, Sherar MD, Hunt JW, Czarnota GJ, Kolios MC. High-frequency ultrasound scattering from microspheres and single cells. *J Acoust Soc Am* 2005;117(2):934-43.

128. Brand S, Solanki B, Foster D, Czarnota GJ, Kolios MC. Monitoring of cell death in epithelial cells using high frequency ultrasound spectroscopy. *Ultrasound Med Biol.* in press x;x(x):x-.

129. Brand S, Czarnota GJ, Kolios MC, Weiss EC, Lemor R. Visualization of apoptotic cells using scanning acoustic microscopy and high frequency ultrasound. *Ultrasonics Symposium, IEEE 2005*;2:882-5.

130. Baddour RE, Kolios MC. In: The effect of volume fraction on the backscatter from nucleated cells at high frequencies. *2005 IEEE ultrasonics symposium, 2005.* p. 1672-4.

131. Yu FTH, Cloutier G. Experimental ultrasound characterization of red blood cell aggregation using the structure factor size estimator. *J Acoust Soc Am 2007*;122(1):645-56.

132. Tunis AS, Spurrell D, McAlduff D, Giles A, Hariri M, Khokha R, et al. High frequency ultrasound signal statistics from mouse mammary tissue during involution. *Ultrasonic symposium IEEE 2004*;Volume 1:768-71.

133. Savery D, Cloutier G. High-frequency ultrasound backscattering by blood: Analytical and semianalytical models of the erythrocyte cross section. *J Acoust Soc Am 2007*;121(6):3963-71.

134. Franceschini E, Yu FT, Cloutier G. Simultaneous estimation of attenuation and structure parameters of aggregated red blood cells from backscatter measurements. *J Acoust Soc Am 2008*;123(4):E85-91.

135. Kolios MC, Czarnota GJ. In: High frequency ultrasound scattering from mixtures of two different cells lines: Tissue characterization insights. ; 2008. p. 25-8.

136. Fuks Z, Kolesnick R. Engaging the vascular component of the tumor response. *Cancer Cell* 2005;8(2):89-91.